STRAIN EFFECTS ON SILICON CMOS TRANSISTORS: THRESHOLD VOLTAGE, GATE TUNNELING CURRENT, AND *1/f* NOISE CHARACTERISTICS

By

JI-SONG LIM

A DISSERTATION PRESENTED TO THE GRADUATE SCHOOL
OF THE UNIVERSITY OF FLORIDA IN PARTIAL FULFILLMENT
OF THE REQUIREMENTS FOR THE DEGREE OF
DOCTOR OF PHILOSOPHY

UNIVERSITY OF FLORIDA

2007

To my family
whose encouragement and support have made this possible

ACKNOWLEDGMENTS

I would like to express my sincere gratitude to all those who gave me the opportunity to complete this thesis. Special thanks are due to my principal advisor, Dr. Scott E. Thompson, for his constant encouragement and expert guidance. He has introduced me to the research area of strained silicon CMOS transistors, and has provided valuable advice and direction throughout my doctorate studies.

I would also like to thank my co-advisor, Dr. Toshikazu Nishida, for encouraging my research work, for his consistent excellent technical advice, and for teaching me to write a good research paper. Thanks also go to Drs., Ramakant Srivastava, Ant Ural, and Hugh Fan for their interest and participation in serving on my committee and their suggestions and comments.

All the former and current members of the strained silicon group have contributed immeasurably to my research work through interactive discussions. I have been privileged to work with Kehuey Wu, Guangyu Sun, Andy Koehler, Sagar Suthram, Uma Aghoram, Nirav Shah, Younsung Choi, Nidhi Mohata, Xiaodong Yang, Srivatsan Parthasarathy, Min Chu, Xiaoliang Lu, Yongke Sun, Toshi Numata, Hyunwoo Park, Tony Acosta. These people have made me working in the lab and office with lots of fun, and many have provided useful advice for me. I am especially thankful to Kehuey Wu for his help with the proper use of a wafer bending jig.

I dedicate this dissertation to my family, without whose support and patience so long time, my achievement could not have been complete. Last but not least, I especially like to thank my loving mother, brother, sisters and relatives in Korea for their everlasting love and trust in my efforts, and for standing by me whenever I needed them the most.

TABLE OF CONTENTS

LIST OF TABLES

LIST OF FIGURES

Abstract of Dissertation Presented to the Graduate School
of the University of Florida in Partial Fulfillment of the
Requirements for the Degree of Doctor of Philosophy

STRAIN EFFECTS ON SILICON CMOS TRANSISTORS: THRESHOLD VOLTAGE, GATE TUNNELING CURRENT, AND 1/*f* NOISE CHARACTERISTICS

By

Ji-Song Lim

December 2007

Chair: Scott E. Thompson
Cochair: Toshikazu Nishida
Major: Electrical and Computer Engineering

The study of strain effects on CMOS (complementary-metal-oxide-semiconductor) transistors has been mainly focused on drive current enhancements. In computer central processing unit (CPU) chips, strained CMOS transistors play an important role for high speed computer operations since the CPU speed is directly related to the current drive capabilities of the transistors controlling the CMOS logic circuitry in the chips. In addition to this strain effect on channel carrier mobilities, strain also affects other important physical properties in MOSFETs. This dissertation investigates such strain effects on the MOSFET operation as threshold voltage, gate tunneling current, and low-frequency *1/f* noise characteristics. Strain engineering of the MOSFET channel alters the inversion subband energy levels which, in turn, influences these physical properties as well as channel carrier mobilities. More specifically, shear strain reduces symmetry in silicon and lifts the degeneracy of both conduction and valence bands. As a result, the constant energy surfaces are severely warped for the valence band whereas the shapes of the energy surfaces are unchanged to the first order in stress for the conduction band. The strain effects on silicon MOSFETs are then classified as an effect of band splitting and shifts due to the hydrostatic and shear strain components for both conduction and valence bands, and an

additional effect of subband (heavy- and light-hole) effective mass change due to the band warping for the valence band.

Based on these key strain effects on MOSFETs, the calculated values for threshold voltage shifts are quite consistent with the measured data for n-channel MOSFETs under uniaxial tensile stress as well as the published experimental data for biaxially tensile-strained n-channel MOSFETs. Gate tunneling currents are also well predicted by this strain model including band splitting, shifts and warping. Furthermore, conduction deformation potential constants are determined through this gate tunneling current measurements on n-channel MOSFETs under mechanical stress. Strain effects on *1/f* noise are also studied in conjunction with applications of strained devices to high performance RF or high speed CMOS circuits. Detailed physical mechanisms of the strain effects on *1/f* noise power spectral density (PSD) are identified and the contribution of each mechanism to the resultant change in *1/f* noise PSD is estimated on the basis of the measured data.

CHAPTER 1
INTRODUCTION

Historical Overview of Research on Strain Effects on Semiconductors

Over the past 50 years, strain effects on semiconductors such as Si and Ge have been extensively studied both theoretically and experimentally. Bardeen and Shockley first introduced a deformation potential theory in 1950 to explain phonon scattering in semiconductors [1]. It was shown in their paper that the electron- or hole-phonon interaction causes a static displacement of the atoms, thus resulting in the conduction or valence band energy shifts. Later in 1956, Herring and Vogt further generalized the deformation potential method [2] and formulated the conduction band energy shift as a function of strain together with a couple of deformation potential constants. Strain effects on valence bands were also quantified by Pikus and Bir [3]. They constructed a strain Hamiltonian for valence bands based on an invariance property of the angular momentum under symmetry operations of a crystal. In 1963, Hasegawa added the spin-orbit split-off (SO) band effects to this Hamiltonian [4], which has become a currently-used typical strain Hamiltonian form of valence bands.

Experimentally, numerous endeavors have been made to determine deformation potentials in strained Si, Ge and other materials. In 1954, Smith first observed the piezoresistance change in strained Si and Ge [5]. Since then, piezoresistance measurements have been used as an important experimental method for determining the deformation potential constants [6]. Hensel and Feher conducted a cyclotron resonance experiment in 1963 [7] to determine deformation potentials in Ge. By the photoluminescence technique, Balslev determined deformation potentials for Si and Ge [8], and Bhargave and Nathan for GaAs [9]. Besides, Pollak and Cardona used a piezo-electroreflectance technique [10] to measure deformation potentials for Si, Ge and GaAs. In all these experiments mentioned above, however, only strain-induced relative energy level shifts could be measured. As a result, the dilation deformation potential for Si (commonly denoted by

symbol, Ξ_d), which is related to the absolute energy level shift in the conduction band, has been reported over a very wide range including opposite signs, 1.13 to -10.7 eV [11, 12]. Recently in our lab, an experimental method to determine a value of Ξ_d for Si has been proposed [13]. The method is based on the change in the gate direct tunneling currents of Si n-MOSFETs under externally applied mechanical stress, from which the obtained value is quite consistent with theoretical works.

While the earlier studies on strain were mainly focused on bulk semiconductor properties, practical studies for CMOS device applications began in the 1980's with the advance of fabrication process technologies [14, 15]. In order to increase the drive current (or charge carrier mobility) in Si MOSFETs, typically two types of process techniques were developed for introducing strain into the Si surface channel. As shown in Fig.1-1, one type of technique is to use epitaxial technology to form a thin layer of Si on top of the relaxed silicon germanium ($Si_{1-x}Ge_x$) layer [16, 17]. Since the $Si_{1-x}Ge_x$ layer has a larger lattice constant, the thin Si channel layer is permanently under biaxial tensile strain. The other type is source/drain engineering and thin film process techniques, which were developed by Intel in the 1990's, such as high-stress nitride capping layers around the gate and selective epitaxial $Si_{1-x}Ge_x$ in the source/drain regions [18]. The nitride capping layer approach is applied to n-MOSFETs for uniaxial tensile strain and the embedded $Si_{1-x}Ge_x$ approach to p-MOSFETs for uniaxial compressive strain [18].

Strain has been recognized as one of the key technology features for scaled MOSFET devices [19, 20]. Over the past 30 years, the downscaling of MOSFET dimensions has continued to improve device performances [21], and actually great benefits have been achieved in terms of the transistor speed, density, cost, and power consumption.

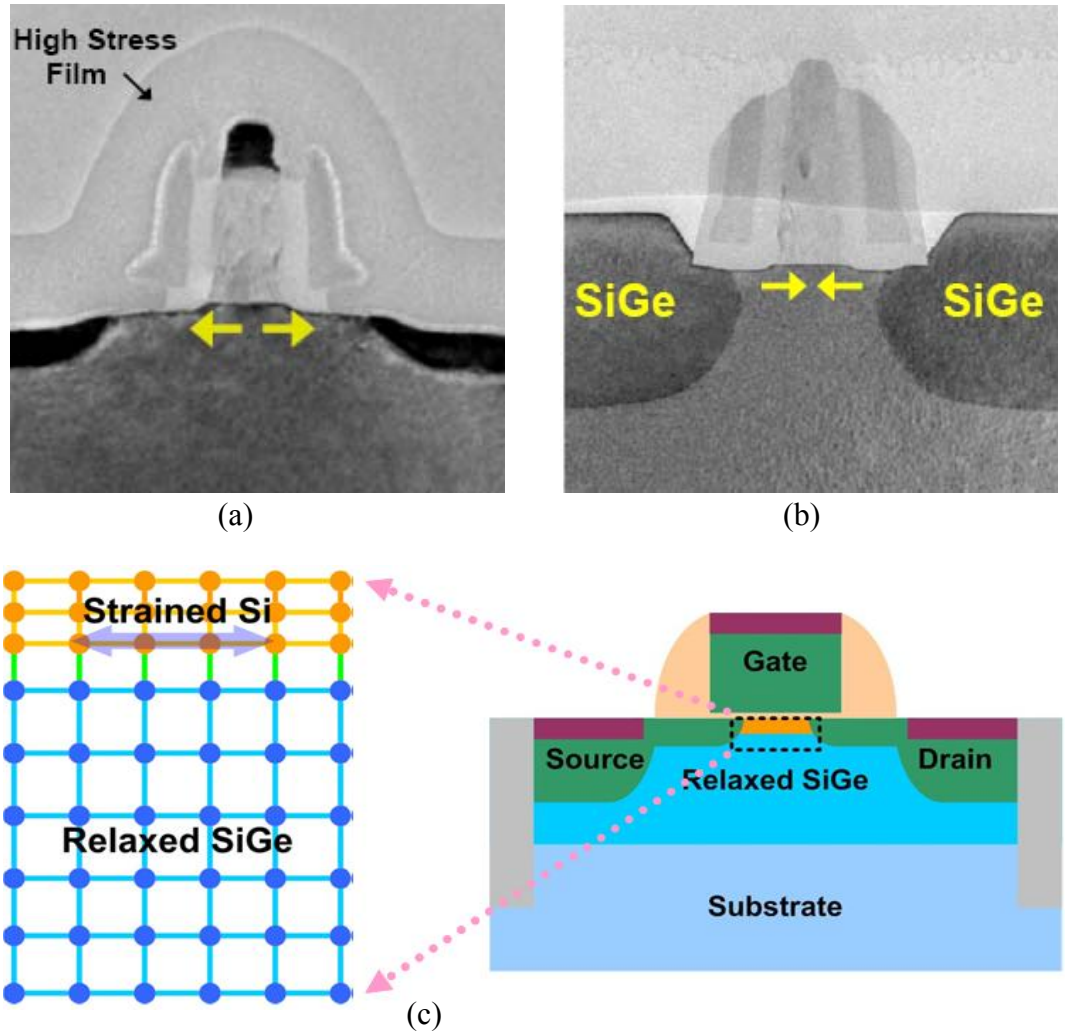

Figure 1-1. Uniaxially- and biaxially-strained Si MOSFETs, adapted from [18, 27]. (a) Nitride capping layered n-MOSFET. (b) p-MOSFET with a $Si_{1-x}Ge_x$ source and drain. (c) Biaxially-strained Si MOSFET on a relaxed $Si_{1-x}Ge_x$ layer.

However, as the dimension scaling approaches physical limitations (for example, ~30 nm gate length and ~1 nm gate oxide thickness), a number of difficulties such as short channel effects and increased gate leakage currents arise, thus making the device scaling an increasingly challenging task. To maintain this historical trend of performance improvements through scaling, the industry requires noble solutions. One solution under active study to reduce the gate leakage current is the use of high-k materials for the gate dielectric [21]. The introduction of high-κ dielectric materials, however, results in drive current loss due to carrier mobility degradation

[19]. Then currently, strained-Si MOSFETs are drawing researchers' attention again as an alternative to compensating for this drive current loss.

Motivation

Typically, biaxial tensile stress is introduced via a thin epitaxial Si channel grown on a relaxed $Si_{1-x}Ge_x$ substrate. Alternatively, carrier mobility enhancement can be obtained using longitudinal uniaxial tensile stress typically introduced with a nitride capping layer or through an embedded $Si_{1-x}Ge_x$ source/drain. Since the strain capping layer or the embedded $Si_{1-x}Ge_x$ approach requires negligible alterations to a standard CMOS process flow, uniaxial strain was widely adopted at the 90-nm generation [18]. Biaxial and uniaxial tensile strain-enhanced channel carrier mobility has been well studied, and shown to primarily result from lower conductivity effective mass under gate bias and strain and reduced intervalley scattering [14-21]. On the other hand, less attention has been paid to other important physical properties such as threshold voltage, gate tunneling current and low frequency *1/f* noise characteristics.

Understanding the threshold voltage shift is important when determining the performance gain of strained Si. Since performance benchmarking needs to be done at constant off-state leakage, an adjustment to compensate for the strain-induced threshold voltage shift is required. This adjustment is typically accomplished by increasing the well doping concentration which degrades mobility and increases junction capacitance. The study on threshold voltage is also important in relation to device lifetime and reliability.

In the design of strained silicon devices, it is essential to accurately quantify strain-induced energy level shifts and splitting which are modeled by deformation potentials. Strain-induced band splitting removes conduction and valence band degeneracy and is primarily responsible for the engineered mobility enhancement. While the shear deformation potentials used to calculate energy level splitting are well known with good accuracy from piezoresistance measurements

(Ξ_u = 9.16 eV), the hydrostatic deformation potential is difficult to directly measure using the conventional optical techniques. As a result, a very wide range of values with opposite signs have been reported (1.13 to -10.7 eV) [11, 12]. This results since the optical experimental techniques directly measure differences in energy levels (for example, strain-induced band gap narrowing) but not the absolute position of the energy levels which leaves large uncertainty in important band parameters such as the electron affinity of strained-Si.

Recently, low frequency *1/f* noise has drawn researchers' attention in conjunction with applications of strained devices to analog circuits. Since *1/f* noise often acts as a critical limiting factor in analog circuit design, it is essential to understand the effect of strain on *1/f* noise and quantify its magnitude. Although some studies exist on strain effects on *1/f* noise, they mainly focus on processing aspects in strained SiGe MOSFETs []. None has elucidated fundamental strain effects on 1/*f* noise yet.

Scope and Organization

This dissertation deals with strain effects on MOSFET operations; threshold voltage, gate tunneling current and low frequency *1/f* noise characteristics. The outline is as follows.

Chapter 2 gives a brief introduction of the strain-stress relation and a representative method of strain components in terms of elastic compliance constants. Based on this strain representation, the deformation potentials of the conduction and valence bands are calculated, and the band edge shifts and splitting are discussed in detail as strain effects.

In Chapter 3, we first examine our stress-applying apparatuses of the uniaxial and biaxial jigs and then review the strain-induced threshold voltage model for n-MOSFETs. Each component of the model is also analyzed thoroughly in conjunction with its underlying physical mechanism.

In Chapter 4, strain effects on the gate tunneling current are dealt with. Based on experimental observations, qualitative analyses are made first for both n- and p-MOSFETs. The detailed model for n-MOSFETs is then presented. Next, deformation potential constants are extracted from the measured data on the basis of this model prediction.

In Chap. 5, strain effects on *1/f* noise are dealt with. The experimental method with an electrical measurement setup is first introduced. The measurement results and data analysis for both n- and p-MOSFETs are then discussed. Detailed mechanisms of strain effects on noise PSD are identified and the contribution of each mechanism to the total noise PSD is estimated.

Finally, Chap. 6 is the summary and the recommendation for the future work.

CHAPTER 2
STRAIN EFFECT ON SILICON ENERGY BAND

In this chapter, we will briefly review the basics of strain effects on both conduction and valence energy bands which are relevant to our work. The magnitude of the energy band shift with strain is typically calculated by introducing elastic compliance constants (*S*-matrix elements) or stiffness constants (*C*-matrix elements) to represent strain components. Of these two representations, the *S*-matrix representation will be used throughout this dissertation.

Representation of Strain Component with S-matrix Element

A solid under stress is generally characterized by a second order stress tensor $\boldsymbol{\sigma}$ whose elements σ_{ij} are defined as the *j*-component of the force transferred per unit area perpendicular to the *i*-direction. The sign is positive for tensile stress and negative for compressive stress. Simple equilibrium considerations yield that $\sigma_{ij} = \sigma_{ji}$. Similarly, the deformation can be described by a second order strain tensor $\boldsymbol{\varepsilon}$:

$$\varepsilon_{ij} = \varepsilon_{ji} = \frac{1}{2}\left(\frac{\partial u_i}{\partial x_j} + \frac{\partial u_j}{\partial x_i}\right), \tag{2-1}$$

where **u** is the displacement of a solid. The relation between stress and strain can be also given by the fourth order elastic compliance tensor $\boldsymbol{S}$:

$$\varepsilon_{ij} = S_{ijkl}\sigma_{kl}. \tag{2-2}$$

This constitutes a sequence of nine equations, since each strain component of ε_{ij} is a linear combination of all the stress components of σ_{ij}, that is, $\varepsilon_{ij} = S_{ij11}\sigma_{11} + S_{ij12}\sigma_{12} + \ldots\ldots + S_{ij33}\sigma_{33}$. In the constitutive relation, totally there are 9 components each for both strain and stress tensors, and 81 independent components for the compliance tensor. However, both $\boldsymbol{\varepsilon}$ and $\boldsymbol{\sigma}$ are symmetric,

with 6 rather than 9 components each. As a result, we can express Eq. (2-2) in a reduced matrix form where 81 compliance components reduce to 36 as shown in reference [22]:

$$\begin{pmatrix} \varepsilon_1 \\ \varepsilon_2 \\ \varepsilon_3 \\ \varepsilon_4 \\ \varepsilon_5 \\ \varepsilon_6 \end{pmatrix} = \begin{pmatrix} S_{11} & S_{12} & S_{13} & S_{14} & S_{15} & S_{16} \\ S_{21} & S_{22} & S_{23} & S_{24} & S_{25} & S_{26} \\ S_{31} & S_{32} & S_{33} & S_{34} & S_{35} & S_{36} \\ S_{41} & S_{42} & S_{43} & S_{44} & S_{45} & S_{46} \\ S_{51} & S_{52} & S_{53} & S_{54} & S_{55} & S_{56} \\ S_{61} & S_{62} & S_{63} & S_{64} & S_{65} & S_{66} \end{pmatrix} \begin{pmatrix} \sigma_1 \\ \sigma_2 \\ \sigma_3 \\ \sigma_4 \\ \sigma_5 \\ \sigma_6 \end{pmatrix}, \tag{2-3}$$

where the 6×1 column matrices of both strain and stress are defined, respectively, as

$$\begin{pmatrix} \varepsilon_1 \\ \varepsilon_2 \\ \varepsilon_3 \\ \varepsilon_4 \\ \varepsilon_5 \\ \varepsilon_6 \end{pmatrix} \equiv \begin{pmatrix} \varepsilon_{11} \\ \varepsilon_{22} \\ \varepsilon_{33} \\ 2\varepsilon_{23} \\ 2\varepsilon_{13} \\ 2\varepsilon_{12} \end{pmatrix}, \qquad \begin{pmatrix} \sigma_1 \\ \sigma_2 \\ \sigma_3 \\ \sigma_4 \\ \sigma_5 \\ \sigma_6 \end{pmatrix} \equiv \begin{pmatrix} \sigma_{11} \\ \sigma_{22} \\ \sigma_{33} \\ \sigma_{23} \\ \sigma_{13} \\ \sigma_{12} \end{pmatrix} \tag{2-4}$$

This resulting matrix relation of Eq. (2-3) is no longer a tensor form because each strain component does not follow the coordinate transformation rule as in Eq. (2-2). Further, in cubic crystals such as Si and Ge, the compliance matrix is simplified to [22]

$$(S) = \begin{pmatrix} S_{11} & S_{12} & S_{12} & 0 & 0 & 0 \\ S_{12} & S_{11} & S_{12} & 0 & 0 & 0 \\ S_{12} & S_{12} & S_{11} & 0 & 0 & 0 \\ 0 & 0 & 0 & S_{44} & 0 & 0 \\ 0 & 0 & 0 & 0 & S_{44} & 0 \\ 0 & 0 & 0 & 0 & 0 & S_{44} \end{pmatrix}. \tag{2-5}$$

Now, let us calculate strain components in a cubic crystal for uniaxial stresses with magnitude σ applied along crystallographic axes such as [100], [110], and [111] directions. As shown in Eq. (2-3), since strain components are represented as a product of the S-matrix and

stress matrix, we need to first get stress components for each type of stress. For a [100] stress, it is trivial; all stress components are zero except that $\sigma_{xx} = \sigma$. For the other two directions of stresses, [110] and [111], a little care need to be taken so that all stress components can be obtained as second order stress tensor elements. A simple and straightforward way is to introduce a dyad notation which is equivalent to a second order tensor representation. A dyad is simply a pair of vectors and its operation (namely a dyadic) is defined as

$$\begin{aligned}\vec{A}\vec{B} &\equiv (A_x\hat{i} + A_y\hat{j} + A_z\hat{k})(B_x\hat{i} + B_y\hat{j} + B_z\hat{k}) \\ &\equiv A_xB_x\hat{i}\hat{i} + A_xB_y\hat{i}\hat{j} + A_xB_z\hat{i}\hat{k} + A_yB_x\hat{j}\hat{i} + A_yB_y\hat{j}\hat{j} + A_yB_z\hat{j}\hat{k} \\ &\quad + A_zB_x\hat{k}\hat{i} + A_zB_y\hat{k}\hat{j} + A_zB_z\hat{k}\hat{k} \quad \textit{for any two vectors, } \vec{A} \textit{ and } \vec{B}.\end{aligned} \tag{2-6}$$

The nine elements above correspond directly to each element of a second order tensor. Further, in consideration of the properties of a stress tensor (the symmetry condition $\sigma_{ij} = \sigma_{ji}$, and rotation-invariant quantity Tr(σ_{ij}) = magnitude of stress), we can obtain the following stress tensor element in terms of the dyad notation,

$$\sigma_{ij} = \frac{\left(\vec{\sigma}\vec{\sigma}\right)_{ij}}{\left|\vec{\sigma}\right|}. \tag{2-7}$$

Based on Eq. (2-7), we can easily express any stress components for any stress directions, and consequently obtain strain components through the strain-stress matrix relation. Fig. 2-1 shows three crystallographic stress directions and their vector elements. For a [110] stress, the stress vector is given by, $\vec{\sigma} = \sigma \cdot (1/\sqrt{2}, 1/\sqrt{2}\,,\ 0)$. A simple calculation using Eq. (2-7) leads to $\sigma_{xx} = \sigma_{xy} = \sigma/2$, $\sigma_{xy} = \sigma_{yx} = \sigma/2$, with the rest components 0's. Now, using Eq. (2-3) through (2-5) with the stress components obtained above, we can write down the strain-stress matrix relation for a [110] stress as,

$$\begin{pmatrix} \varepsilon_{xx} \\ \varepsilon_{yy} \\ \varepsilon_{zz} \\ 2\varepsilon_{yz} \\ 2\varepsilon_{xz} \\ 2\varepsilon_{xy} \end{pmatrix} = \begin{pmatrix} S_{11} & S_{12} & S_{12} & 0 & 0 & 0 \\ S_{12} & S_{11} & S_{12} & 0 & 0 & 0 \\ S_{12} & S_{12} & S_{11} & 0 & 0 & 0 \\ 0 & 0 & 0 & S_{44} & 0 & 0 \\ 0 & 0 & 0 & 0 & S_{44} & 0 \\ 0 & 0 & 0 & 0 & 0 & S_{44} \end{pmatrix} \begin{pmatrix} \sigma/2 \\ \sigma/2 \\ 0 \\ 0 \\ 0 \\ \sigma/2 \end{pmatrix}, \tag{2-8}$$

which yields the following strain components; $\varepsilon_{xx} = \varepsilon_{yy} = (S_{11} + S_{12})\sigma/2$, $\varepsilon_{zz} = S_{12}\sigma$, $\varepsilon_{yz} = \varepsilon_{xz} = 0$, and $\varepsilon_{xy} = S_{44}\sigma/4$. It should be noted that some authors use a different shear strain component, $\varepsilon_{xy} = S_{44}\sigma/2$, for a [110] stress [4, 7, 23]. This discrepancy arises from the fact that they directly use the tensor notation of Eq. (2-2) to obtain strain components. In our case, however, the contracted matrix notation (or conventional notation), which is not a tensor form rigorously, is used since it is more popular and simpler [12, 24]. Strain components for a [111] stress can be also calculated in the same way. In Table 2-1, strain components are listed for three principal uniaxial stresses and an in-plane biaxial stress ($\sigma_{xx} = \sigma_{yy} = \sigma$, with no other components), together with elastic compliance constant values for Si.

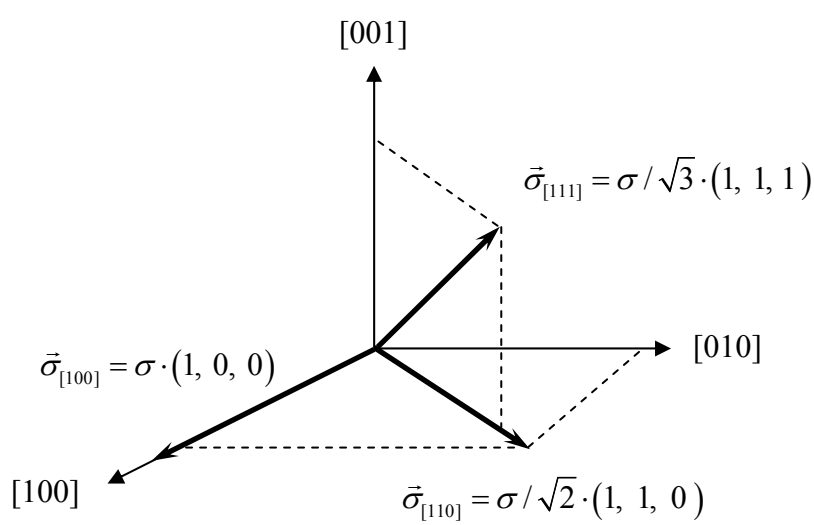

Figure 2-1. Three uniaxial stresses applied along [100], [110], and [111] directions.

Table 2-1. Strain components for three principal uniaxial stresses and an in-plane biaxial stress,and elastic compliance constant values for Si.

Stress type	[100]	[110]	[111]	In-plane biaxial
Strain components	$\varepsilon_{xx} = S_{11}\sigma$ $\varepsilon_{yy} = \varepsilon_{zz} = S_{12}\sigma$ the rest = 0's	$\varepsilon_{xx} = \varepsilon_{yy}$ $= (S_{11}+S_{12})\sigma/2$ $\varepsilon_{zz} = S_{12}\sigma$ $\varepsilon_{xy} = \varepsilon_{yx} = S_{44}\sigma/4$ the rest = 0's ($\varepsilon_{xy} = \varepsilon_{yx} =$ $S_{44}\sigma/2$)	$\varepsilon_{xx} = \varepsilon_{yy} = \varepsilon_{zz}$ $= (S_{11}+2S_{12})\sigma/3$ $\varepsilon_{xy} = \varepsilon_{yx} = \varepsilon_{yz} = \varepsilon_{zy}$ $= \varepsilon_{zx} = \varepsilon_{xz}$ $= S_{44}\sigma/6$ ($\varepsilon_{xy} = \varepsilon_{yx} = \varepsilon_{yz}$ $= \varepsilon_{zy} = \varepsilon_{zx} = \varepsilon_{xz}$ $= S_{44}\sigma/3$)	$\varepsilon_{xx} = \varepsilon_{yy}$ $= (S_{11}+S_{12})\sigma$ $\varepsilon_{zz} = 2S_{12}\sigma$ the rest = 0's

Elastic compliance constants	S_{11}	S_{12}	S_{44}
	7.68×10^{-12} [m^2/N]	-2.14×10^{-12} [m^2/N]	1.26×10^{-11} [m^2/N]

*Strain components in the parentheses are obtained from the strain-stress tensor relation of Eq. (2-2).

Strain Effect on Conduction and Valence Band

Silicon is an indirect energy bandgap semiconductor. In the E-k diagram, as shown in Fig. 2-2, its conduction band edges (the lowest points in the conduction band) are located close to the Brillouin zone boundaries along the [100] and its equivalent directions, while the valence band edge (the highest point in the valence band) lies at the origin (called a Γ-point) in k-space. The regions around conduction band edges are called Δ-valleys, and modeled as six ellipsoids since the constant energy surface in E-k relation around the edges is ellipsoidal in shape. A Λ-valley along the [111] direction is also shown in the figure. It is a higher energy state ($E_L>E_g$), and thus less important for Si The valence band edge comprises six bands including spin degeneracy; its upper bands are four-fold degenerate with heavy- and light-hole states mixed with each other, and its lower bands (called a spin-orbit split-off band) are doublet with a splitting energy of 44meV. These extrema of the conduction and valence energy bands are critical to determine most physical properties (e.g., electronic, optical) in semiconductor devices, so we can understand most device characteristics simply by looking at the behaviors of a small portion of the band structure near band edges.

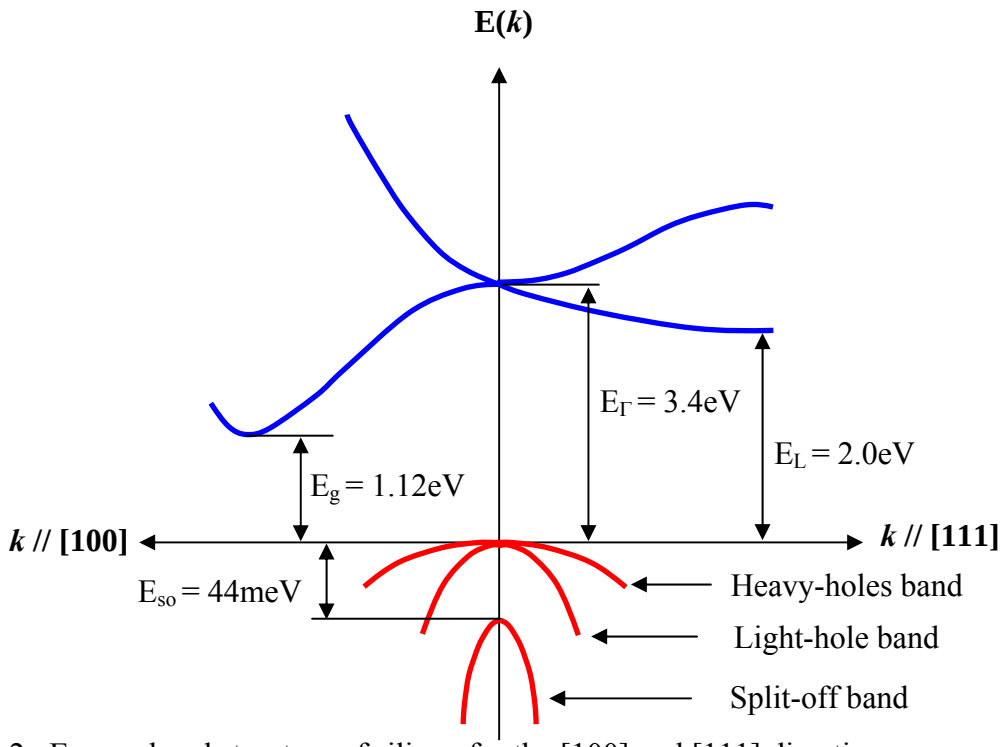

Figure 2-2. Energy band structure of silicon for the [100] and [111] direction.

Strain Effect on Conduction Band

In the region around conduction band edges, each located at six symmetry axes of [100], the energy dispersion (E-k) relation is given by

$$E(\vec{k}) = \frac{\hbar^2}{2}\left(\frac{k_t^2}{m_t^*} + \frac{(k_l - k_0)^2}{m_l^*}\right), \tag{2-9}$$

where the subscripts, t and l, represent transverse and longitudinal directions, respectively, and k_0 is the position of conduction band edges along the longitudinal direction. Fig. 2-3 shows six constant energy ellipsoids in k-space near the conduction band edges. When stress effects on the conduction energy band are concerned, we often refer to "in-plane" or "out-of-plane" effective masses. In this diagram, "in-plane" means a k_x-k_y plane which contains four valleys, and "out-of-plane" is a plane formed along the k_z-direction, which includes two valleys. The in-plane and out-of-plane effective masses for these two valleys in the k_z-direction are calculated, respectively, as

$$\hbar^2 \Big/ \frac{\partial^2 E(\vec{k})}{\partial k_t^2} = m_t^* \cong 0.19 m_0, \quad \hbar^2 \Big/ \frac{\partial^2 E(\vec{k})}{\partial k_l^2} = m_l^* \cong 0.92 m_0, \tag{2-10}$$

where m_0 is the free electron mass. For the four valleys lying on the k_x-k_y plane, the out-of-plane effective mass is $m_t^* (\cong 0.19 m_0)$. In this dissertation, the out-of-plane direction in MOSFETs is always referred to as a gate biasing direction, unless stated otherwise.

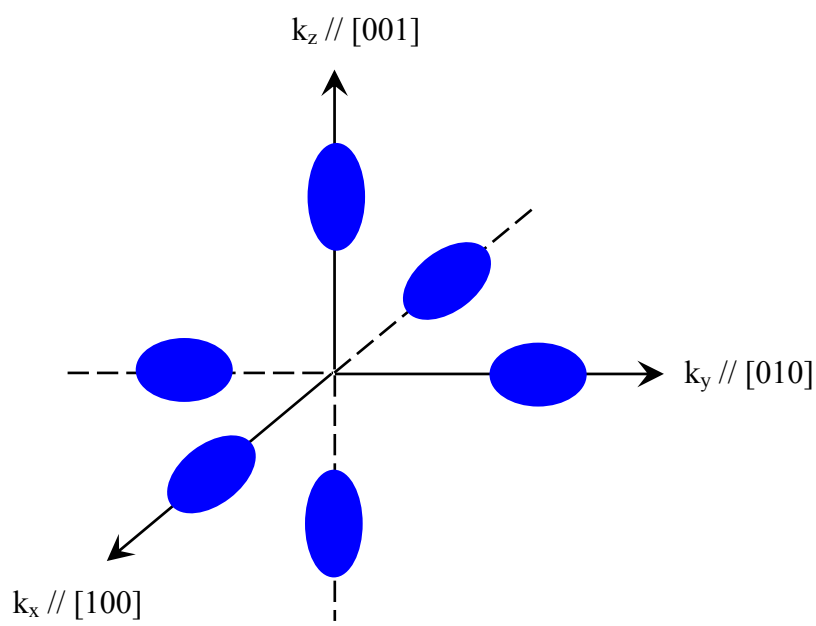

Figure 2-3. Six constant energy ellipsoids in k-space near the conduction band edges.

As mentioned in Chapter I, the strain effects on the conduction energy band were first quantified by Herring and Vogt. They found that the energy shift $\Delta E_c^{(i)}(\sigma)$ for the ith Δ- valley can be expressed in terms of strain components [2, 8],

$$\Delta E_C^{(i)}(\sigma) = \Xi_d \cdot Tr[\varepsilon_{ij}(\sigma)] + \Xi_u \cdot \varepsilon_{ii}(\sigma), \tag{2-11}$$

where Ξ_d and Ξ_u are deformation potential constants named a dilation (or a dilatation) and a shear (or a uniaxial) deformation potential constant, respectively. Here Tr[ε_{ij}] is a sum of the diagonal components of the strain matrix, or Tr[ε_{ij}] ≡ $\varepsilon_{xx} + \varepsilon_{yy} + \varepsilon_{zz}$. The two constant values are

theoretically known to be, Ξ_d = 1.1 eV and Ξ_u = 10.5 eV [12] for bulk Si, and recently confirmed by our gate leakage measurements on n-type MOSFETs in which Ξ_d = 1.0 ± 0.1 eV and Ξ_u = 9.6 ± 1.0 eV [13]. Note that Eq. (2-11) is applied to Δ-valleys and a more general case will be dealt with in Appendix A. Typically Eq. (2-11) can be rewritten as a sum of hydrostatic and shear strain components

$$\Delta E_C^{(i)}(\sigma) = \left(\Xi_d + \frac{\Xi_u}{3}\right) \cdot Tr[\varepsilon_{ij}(\sigma)] + \Xi_u \cdot \left(\varepsilon_{ii}(\sigma) - \frac{Tr[\varepsilon_{ij}(\sigma)]}{3}\right). \tag{2-12}$$

The first term represents a whole average energy level shift due to a hydrostatic strain component which corresponds to a volume change in a deformed solid. The second is a band splitting term due to a shear strain component which is responsible for the twisted deformation of a solid, and it causes the six-fold degenerate conduction bands (Δ_6) to split into two-fold degenerate (Δ_2) and four-fold degenerate (Δ_4) subbands. As an example, let us consider bulk Si under in-plane biaxial stress. First, using Table 2-1 and the constant values (Ξ_d = 1.1 eV and Ξ_d = 10.5 eV), we can calculate the average energy level shift due to a hydrostatic strain component:

$$\begin{aligned}\Delta E_C^{Hydro}(\sigma) &= \left(\Xi_d + \frac{\Xi_u}{3}\right) \cdot Tr[\varepsilon_{ij}(\sigma)] = 2\left(\Xi_d + \frac{\Xi_u}{3}\right)(S_{11} + 2S_{12})\sigma \\ &\cong 3.13 \times 10^{-8}\sigma \ [meV],\end{aligned} \tag{2-13}$$

with σ in a unit of Pascal. Under hydrostatic strain, the average energy level of the six-fold degenerate conduction bands is up-shifted for in-plane tension, while down-shifted for in-plane compression. In Fig. 2-4, the average energy level shift and band splitting are illustrated under in-plane biaxial stress. Next, the band splitting energy due to a shear strain component is calculated as

$$\Delta E^{(z)}_{C\_Shear}(\sigma) = \Xi_u \cdot \left(\varepsilon_{zz}(\sigma) - \frac{Tr[\varepsilon_{ij}(\sigma)]}{3} \right) = -\frac{2}{3}\Xi_u \left(S_{11} - 2S_{12} \right)\sigma$$
$$\cong -8.37 \times 10^{-8}\sigma \ [meV], \tag{2-14}$$

which corresponds to the Δ_2 band splitting along the k_z-direction, with referenced to the shifted average energy level due to a hydrostatic strain. Further, since the average energy level is not changed with shear strain as depicted in the figure, the following relation must hold:

$$\Delta E^{(z)}_{C\_Ave}(\sigma) = 2 \cdot \Delta E^{(z)}_{\Delta_2\_Spl}(\sigma) + 4 \cdot \Delta E^{(z)}_{\Delta_4\_Spl}(\sigma) = 0, \tag{2-15}$$

where the factors, 2 and 4, are attributed to the numbers of Δ_2- and Δ_4-valleys, respectively. From Eq. (2-14) and (2-15), we also obtain the Δ_4 band splitting energy,

$$\Delta E^{(z)}_{\Delta_4\_Spl}(\sigma) = \frac{1}{3}\Xi_u \left(S_{11} - 2S_{12} \right)\sigma \cong 4.19 \times 10^{-8}\sigma \, [meV]. \tag{2-16}$$

The general rule for the splitting directions is that $\Delta_2 \downarrow$ (downward) and $\Delta_4 \uparrow$ (upward) when compressive stress is applied along the splitting direction, while $\Delta_2 \uparrow$ and $\Delta_4 \downarrow$ with tensile stress applied along the splitting direction. As shown in the example of the in-plane tensile stress, $\Delta_2 \downarrow$ and $\Delta_4 \uparrow$ along the k_z-direction since the direction is under compressive stress, but $\Delta_2 \uparrow$ and $\Delta_4 \downarrow$ along the k_x- or k_y-direction. Using the same method so far, we can also obtain conduction band edge shifts for the other directions of stress. In table 2-2, conduction band splittings along the [001] direction are listed for [100], [110] and [111] uniaxial stresses and an in-plane biaxial stress.

Strain Effect on Valence Band

Near the band edge $(\vec{k} = 0)$, the energy dispersion (E-k) relation for heavy- and light-hole bands can be determined by the application of $\vec{k} \cdot \vec{p}$ perturbation to the band edge [7, 25] as

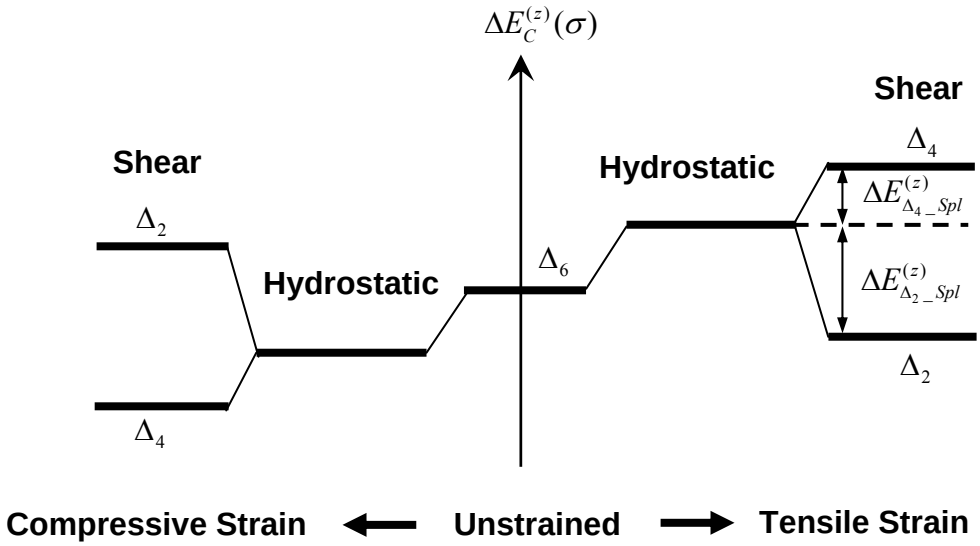

Figure 2-4. Average energy level shift and band splitting in the conduction band along the k_z direction under in-plane biaxial stress.

Table 2-2. Conduction band splittings along the [001] direction for [100], [001], [110] and [111] uniaxial stresses and an in-plane biaxial stress.

Stress type	Splitting direction	Band splitting
[100]	$\Delta_2\downarrow$ $\Delta_4\uparrow$	$-\frac{1}{3}\Xi_u\left(S_{11}-S_{12}\right)\sigma,\quad \frac{1}{6}\Xi_u\left(S_{11}-S_{12}\right)\sigma$
[001]	$\Delta_2\uparrow$ $\Delta_4\downarrow$	$\frac{2}{3}\Xi_u\left(S_{11}-S_{12}\right)\sigma,\quad -\frac{1}{3}\Xi_u\left(S_{11}-S_{12}\right)\sigma$
[110]	$\Delta_2\downarrow$ $\Delta_4\uparrow$	$-\frac{1}{3}\Xi_u\left(S_{11}-S_{12}\right)\sigma,\quad \frac{1}{6}\Xi_u\left(S_{11}-S_{12}\right)\sigma$
[111]	No band splitting	0
In-plane biaxial	$\Delta_2\downarrow$ $\Delta_4\uparrow$	$-\frac{2}{3}\Xi_u\left(S_{11}-2S_{12}\right)\sigma,\quad \frac{1}{3}\Xi_u\left(S_{11}-2S_{12}\right)\sigma$

*The splitting directions (arrows) are based on tensile stresses.

$$E(\vec{k})^{\pm} = Ak^2 \pm \sqrt{B^2k^4 + C^2(k_x^2k_y^2 + k_y^2k_z^2 + k_z^2k_x^2)} \;\; with\; HH('+'),\; LH('-'), \tag{2-17}$$

and for the split-off band we have

$$E(\vec{k})^{(SO)} = Ak^2 - \Lambda, \tag{2-18}$$

where A, B, and C are inverse mass parameters, and their values measured by a cyclotron resonance experiment [26] are $A \cong$ -4.27, $B \cong$ -0.63, and $C \cong$ 4.93 with units of $\hbar / 2m_0$. Fig. 2-5 and 2-6 show E-k diagrams and constant energy surfaces for the heavy-hole, light-hole, and split-off bands near $\vec{k} = 0$, with and without stress. Without stress, the constant energy surfaces of the heavy- and light-hole bands are warped due to their strong interaction with each other, while the split-off band has a spherical energy surface. When stress (a uniaxial [111] tension in Fig. 2-5) is applied, the warped energy surfaces develop into ellipsoids, a prolate ellipsoid for the heavy-hole band and an oblate ellipsoid for the light-hole band. For these ellipsoids of heavy- and light-hole bands, we can calculate the in- and out-of-plane effective masses of each hole as in the case of electrons [4, 7, 27]. Table 2-3 is cited from [27] and some values of the effective masses will be used in Chapter 3 and 4.

Table 2-3. Effective masses of heavy- and light-holes under stress, cited from [27].

Stress type	Direction	Effective mass
In-plane biaxial	In-plane	$m^*_{HH}(\sigma) = 0.21m_0;\;\; m^*_{LH}(\sigma) = 0.26m_0$
	Out-of-plane: [001]	$m^*_{HH}(\sigma) = 0.28m_0;\;\; m^*_{LH}(\sigma) = 0.20m_0$
[001] uniaxial	[001]	$m^*_{HH}(\sigma) = 0.28m_0;\;\; m^*_{LH}(\sigma) = 0.20m_0$
	[100]; [010]	$m^*_{HH}(\sigma) = 0.21m_0;\;\; m^*_{LH}(\sigma) = 0.26m_0$
[110] uniaxial	[110]	$m^*_{HH}(\sigma) = 0.54m_0;\;\; m^*_{LH}(\sigma) = 0.15m_0$
	$[1\bar{1}0]$	$m^*_{HH}(\sigma) = 0.16m_0;\;\; m^*_{LH}(\sigma) = 0.44m_0$
[111] uniaxial	[001]	$m^*_{HH}(\sigma) = 0.21m_0;\;\; m^*_{LH}(\sigma) = 0.26m_0$
	[111]	$m^*_{HH}(\sigma) = 0.86m_0;\;\; m^*_{LH}(\sigma) = 0.14m_0$
	$[1\bar{1}0]$; $[\bar{1}10]$	$m^*_{HH}(\sigma) = 0.17m_0;\;\; m^*_{LH}(\sigma) = 0.37m_0$

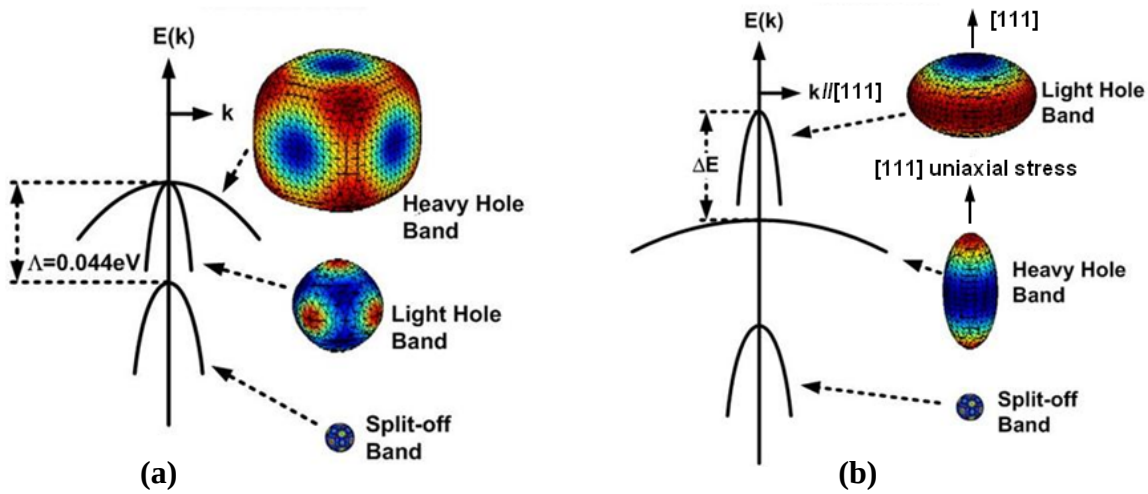

Figure 2-5. Stress effects on the valence energy bands near $\vec{k} = 0$. (Adapted from [27])(a) Unstressed. (b) Under [111] uniaxial compression.

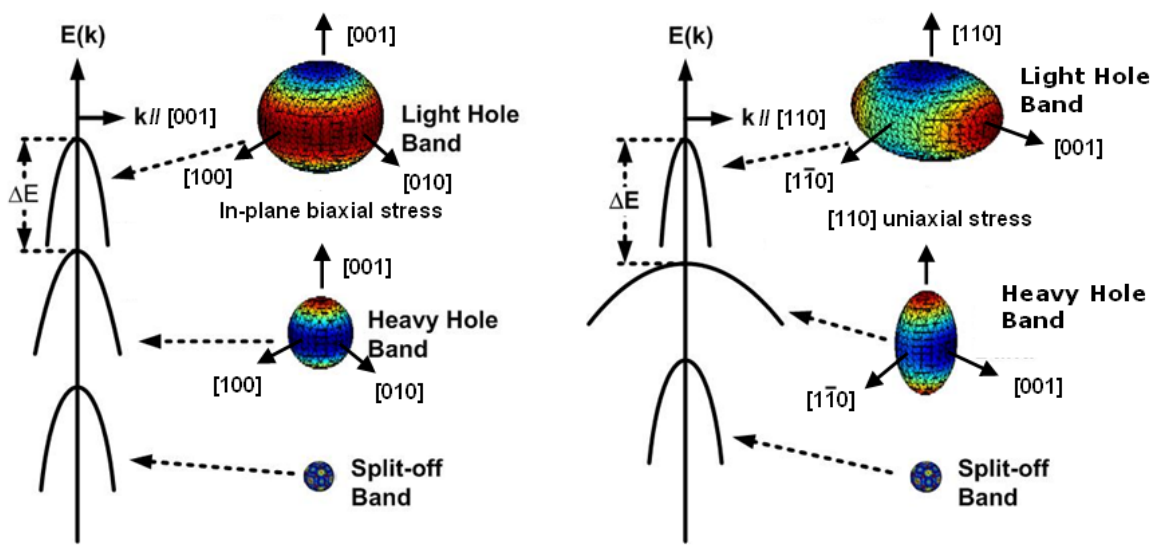

Figure 2-6. Stress effects on the valence energy bands near $\vec{k} = 0$. (Adapted from [27])(a) Under in-plane biaxial tension. (b) Under [110] uniaxial compression.

Based on the Pikus and Bir strain Hamiltonian (in the absence of spin-orbit interaction), the valence band edge shift (average energy level shift plus band splitting) under stress is given by [3, 8]

$$\Delta E_V^{(\pm)}(\sigma) = a \cdot Tr[\varepsilon_{ij}(\sigma)] \pm (-1)^j \sqrt{\frac{b^2}{2}\left[\left(\varepsilon_{xx}(\sigma) - \varepsilon_{yy}(\sigma)\right)^2 + c.p.\right] + d^2\left[\varepsilon_{xy}^2(\sigma) + c.p.\right]}, \quad (2\text{-}19)$$

where '+' and '−' signs correspond to the heavy- and light-hole bands, respectively, and the constants a, b, and d are deformation potentials and c.p. stands for cyclic permutation with respect to the indices x, y, and z. The deformation potentials are shown in [12] that a = 2.1 eV, b = -2.33 eV, and d = -4.75 eV. Note that the light- and heavy-hole bands split upward and downward, respectively, under out-of-plane uniaxial compression (or, in-plane biaxial tension) and reversely under out-of-plane uniaxial tension (or, in-plane biaxial compression). In connection with this opposite splitting for the compression and tension, we need a $(-1)^j$ term in the equation where j = 0 for the uniaxial tension (or, biaxial compression) and j = 1 for the uniaxial compression (or, biaxial tension). In Eq. (2-19), off-diagonal strain components (ε_{xy}, ε_{yz}, ε_{yz}) are used for [110] and [111] uniaxial stresses. As previously pointed out, since off-diagonal components are different for the two methods (conventional notation and tensor notation), the d^2 term in Eq (2-19) must be changed to $d^2/4$ [23, 28] to use the strain components obtained from the tensor notation. The valence band splitting is listed in table 4 for [100], [110] and [111] uniaxial stresses and an in-plane biaxial stress.

Basically, Eq (2-19) is valid for small magnitudes of stresses since it has been derived with spin-orbit interaction neglected. Actually in our stress measurements, the applied stress levels are not so high (< 300 MPa) that we can use Eq (2-19) to analyze our measurement data. However, in biaxially-strained $Si_{1-x}Ge_x$ MOSFETs the internally applied stress level to the channel is as high as ~1.0 GPa for 20% Ge contents. For this amount of high stress, Eq (2-19) is

not valid any more as shown in Fig. 2-7. Then, we need a more accurate expression in which the spin-orbit interaction effect is included. The following is the expression for the valence band edge shift based on the results of Hasegawa's 6×6 Hamiltonian including the spin orbit band [4, 8, 29, 30]:

Table 2-4. Valence band splitting for [100], [110], and [111] uniaxial stresses and an in-plane biaxial stress.

Stress type	Splitting direction		Band splitting
[100]	LH↓	HH↑	$\lvert b(S_{11}-S_{12})\sigma \rvert$
[110]	LH↓	HH↑	$\frac{\lvert\sigma\rvert}{2}\sqrt{b^2\left(S_{11}-S_{12}\right)^2+\left(\frac{d}{2}\cdot S_{44}\right)^2}$
[111]	LH↓	HH↑	$\left\lvert \frac{d}{2\sqrt{3}} S_{44}\sigma \right\rvert$
In-plane biaxial	LH↑	HH↓	$\lvert b(S_{11}-S_{12})\sigma \rvert$

*The splitting directions (arrows) are based on tensile stresses.

$$\Delta E_V(\sigma) = a\cdot Tr[\varepsilon_{ij}(\sigma)] + \begin{cases} -\delta \;\; for \;\; HH \\ \frac{\delta-\Lambda}{2}+\frac{1}{2}\sqrt{\Lambda^2+2\Lambda\cdot\delta+9\delta^2} \;\; for \;\; LH, \\ \frac{\delta+\Lambda}{2}-\frac{1}{2}\sqrt{\Lambda^2+2\Lambda\cdot\delta+9\delta^2} \;\; for \;\; SO \end{cases} \tag{2-20}$$

where the spin-orbit splitting energy Λ = 44 meV, and $\delta = b(\varepsilon_{zz} - \varepsilon_{xx})$ for both [001] uniaxial and in-plane biaxial stresses, and $\delta = \frac{2}{\sqrt{3}} d\cdot\varepsilon_{xy}$ for a [111] uniaxial stress. For a high level of [110] stress, its effects on the valence band edge are too complicated and controversial to obtain an analytic expression [7, 10, 29, 30]. Instead, we can use Eq. (2-19) for a low level of [110] stress. Note that calculation results for [100] and [010] uniaxial stresses are the same as that of a [001] stress since these three directions are symmetric in a cubic crystal and the valence band edge shift is observed same from everywhere due to the center location of the edge in k-space. In Fig. 2-7, the valence band edge shift (average energy level shift plus band splitting) is plotted in

terms of the applied in-plane biaxial stress using Eq. (2-19) and (2-20). In the presence of the spin-orbit interaction, the heavy-hole band is still a pure state but the light-hole and split-off

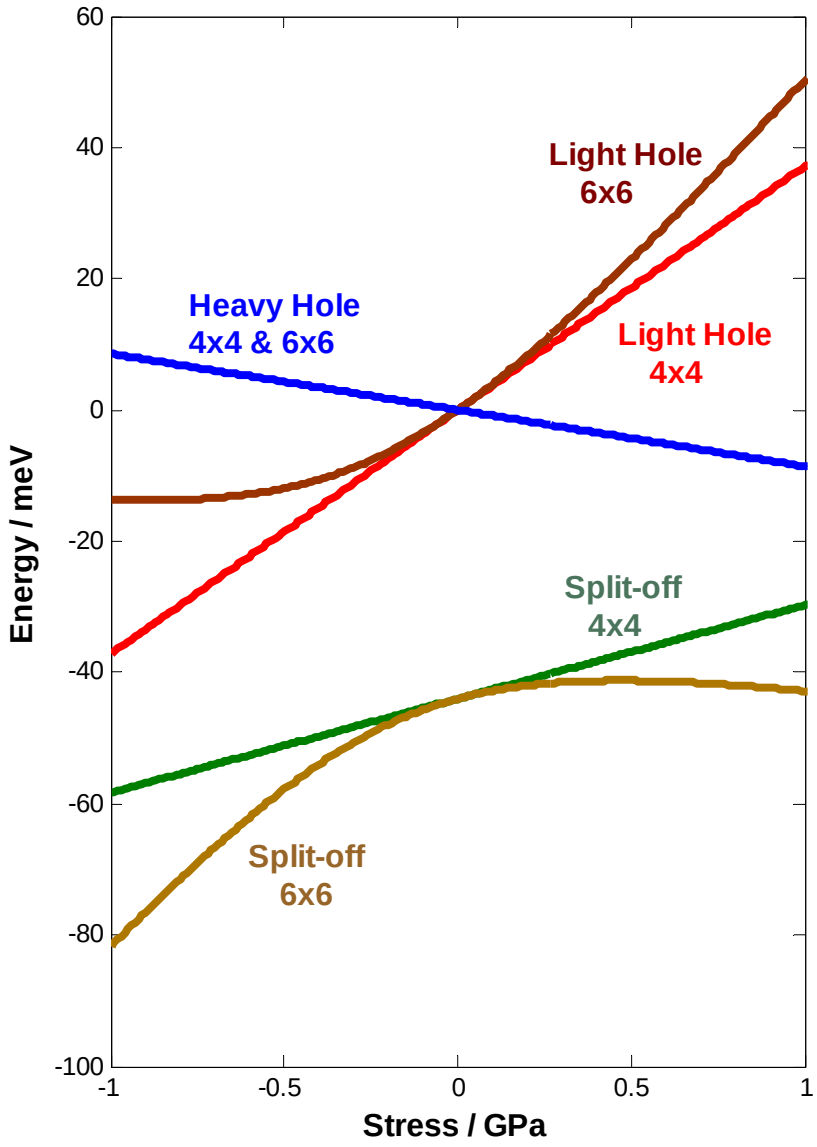

Figure 2-7. Valence band edge shift (average energy level shift plus band splitting) vs. in-plane biaxial stress with (6×6 Hamiltonian) and without spin-orbit interaction (4×4 Hamiltonian). At zero stress the heavy- and light-hole energies are chosen to be zero and accordingly the split-off energy to be -44 meV.

bands are mixed with each other [29]. Because of this band mixing, the light-hole and split-off bands are quite different for with and without spin-orbit interaction at a high stress level. In Fig.

2-8, only the band splitting term is plotted, which exhibits the same result as in [27]. A total sum of band splittings ($\Delta E_{HH}^{Shear}(\sigma)+\Delta E_{LH}^{Shear}(\sigma)+\Delta E_{SO}^{Shear}(\sigma)$) in the valence band is also zero like in the conduction band, each band with the same weighting factor.

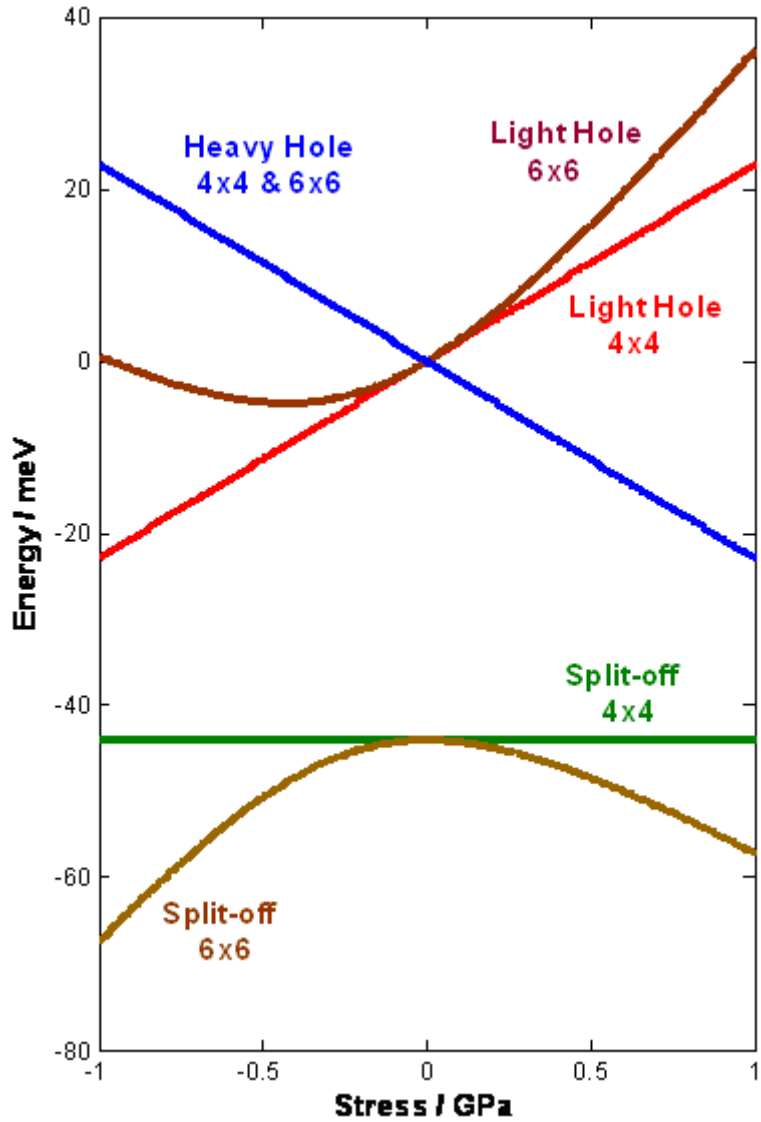

Figure 2-8. Band splitting in the valence band vs. in-plane biaxial stress with (6×6 Hamiltonian) and without spin-orbit interaction (4×4 Hamiltonian). Note that $\Delta E_{V}^{Shear}(\sigma)=\Delta E_{HH}^{Shear}(\sigma)+\Delta E_{LH}^{Shear}(\sigma)+\Delta E_{SO}^{Shear}(\sigma)=0,$ each band with the same weighting factor.

Fig. 2-9 shows a schematic diagram of the valence band edge shift for an in-plane biaxial stress together with that of the conduction band. The energy bandgap is shown to be changed with strain because of the conduction and valence band edge shifts.

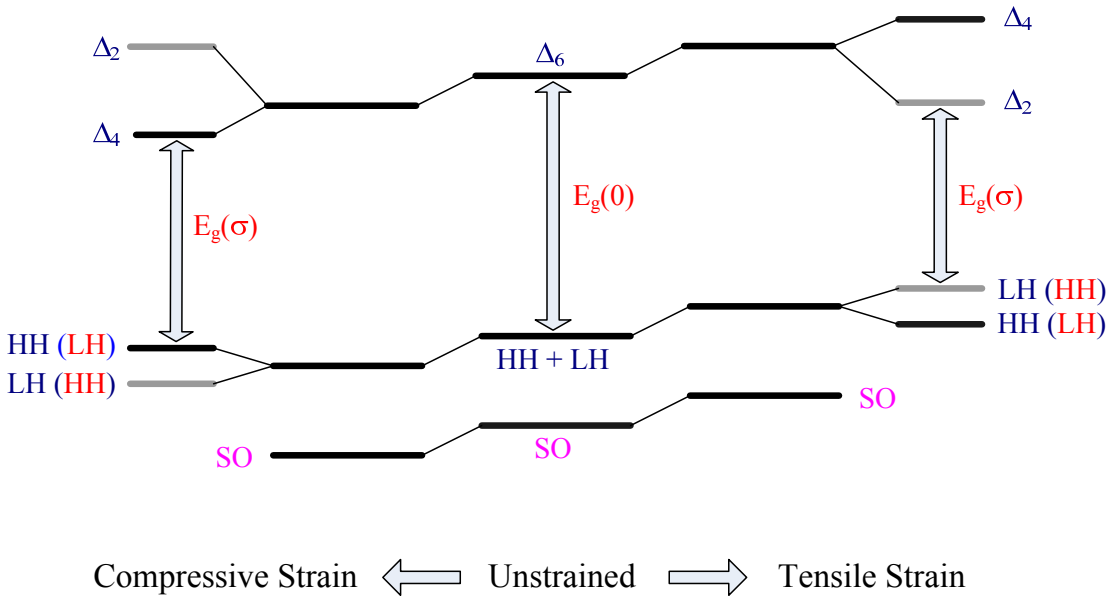

Figure 2-9. Conduction and valence band edge shifts under in-plane biaxial (uniaxial) stress along the out-of-plane direction. The new energy bandgap is determined by Δ_2 and light-hole (heavy-hole) subbands for biaxial (uniaxial) tension, and Δ_4 and heavy-hole (light-hole) subbands for biaxial (uniaxial) compression.

CHAPTER 3
STRAIN EFFECT ON THRESHOLD VOLTAGE

In the previous chapter, we have presented how to express strain components for a different type of stresses and calculated deformation potential energies on the conduction and valence bands in terms of strain. Based on this calculation method for deformation potentials, we can obtain key band parameters (e.g., energy bandgap, electron affinity, valence band offset, and DOS effective masses) to affect the threshold voltage as a function of strain. In this chapter, we start with an experimental technique in which a Si wafer is bent to introduce stress into a MOSFET channel.

Wafer Bending Experiment

Two types of fixtures have been designed to simulate uniaxially- and biaxially- strained MOSFETs as shown in Fig.1-1. Fig. 3-1 shows these fixtures; a uniaxial and a biaxial jig. The uniaxial jig used in applying stress is a four point bending fixture. Such a bending structure has been well studied and a relation between the applied force and stress under uniform stress is given by [31-34]

$$\sigma = \frac{3F(L-D)}{wt^2}, \tag{3-1}$$

where F is the applied force, D and L are the inner and outer support distances respectively, and w and t are the sample's width and thickness as shown in Fig. 3-2. This formula is accurate when the sample is not severely bent to the applied forces and the dimensions w and t are small enough compared with D and L [32]. Under these conditions, the stress directions applied on the both surfaces of the sample can be approximated to be tangential, and the magnitude of stress applied everywhere between the inner supports can be treated as a constant. A detailed diagram is shown in Fig. 3-2. Eq. (3-1) is a useful formula in calibrating stress sensors [32, 34].

However, we can not use it to directly relate the jig parameters with the measured physical quantities.

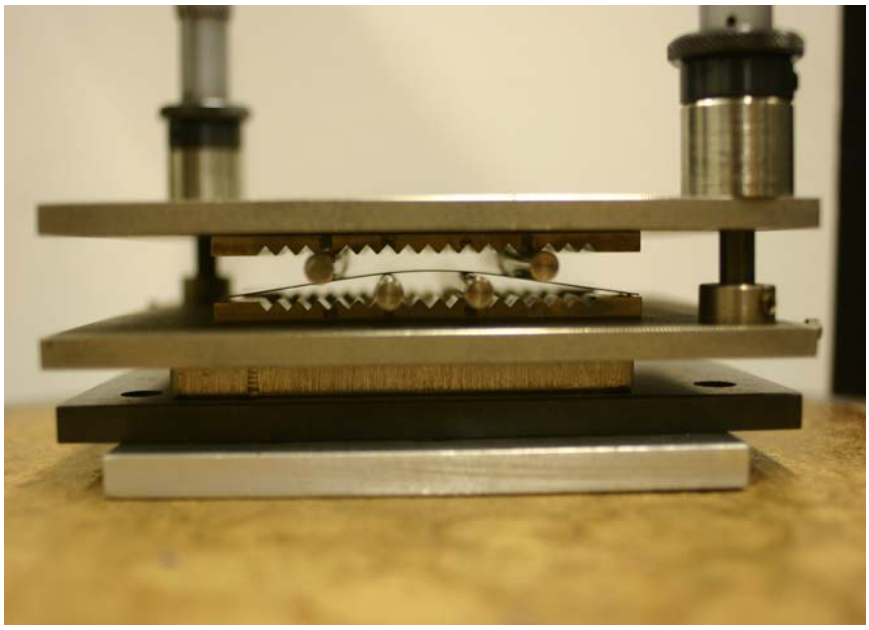

(a)

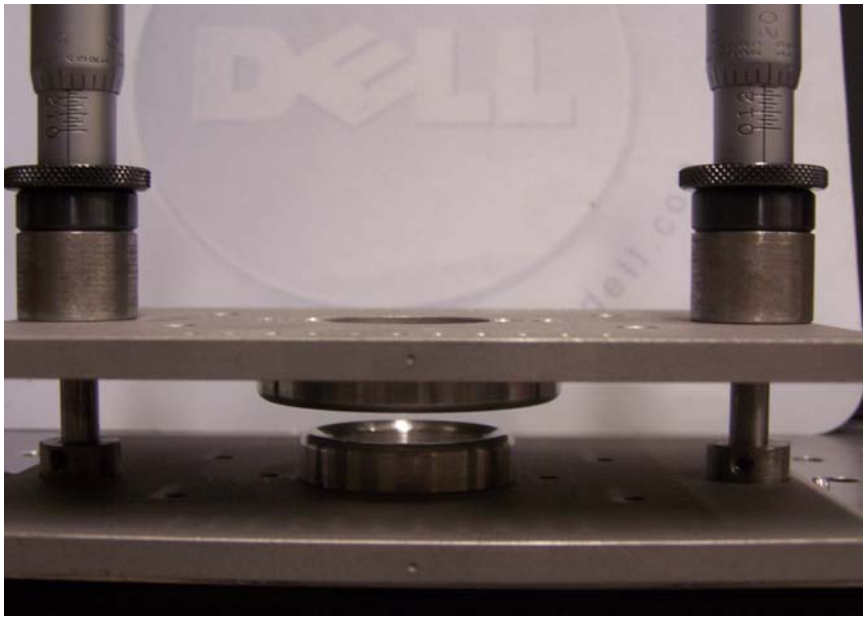

(b)

Figure 3-1. Two types of fixtures to simulate uniaxially-strained and biaxially-strained MOSFETs. (a) For a uniaxial stress, two pairs of cylindrical rods are used and a sample is inserted between the pairs. (b) Two rings with different diameters are used for a biaxial stress.

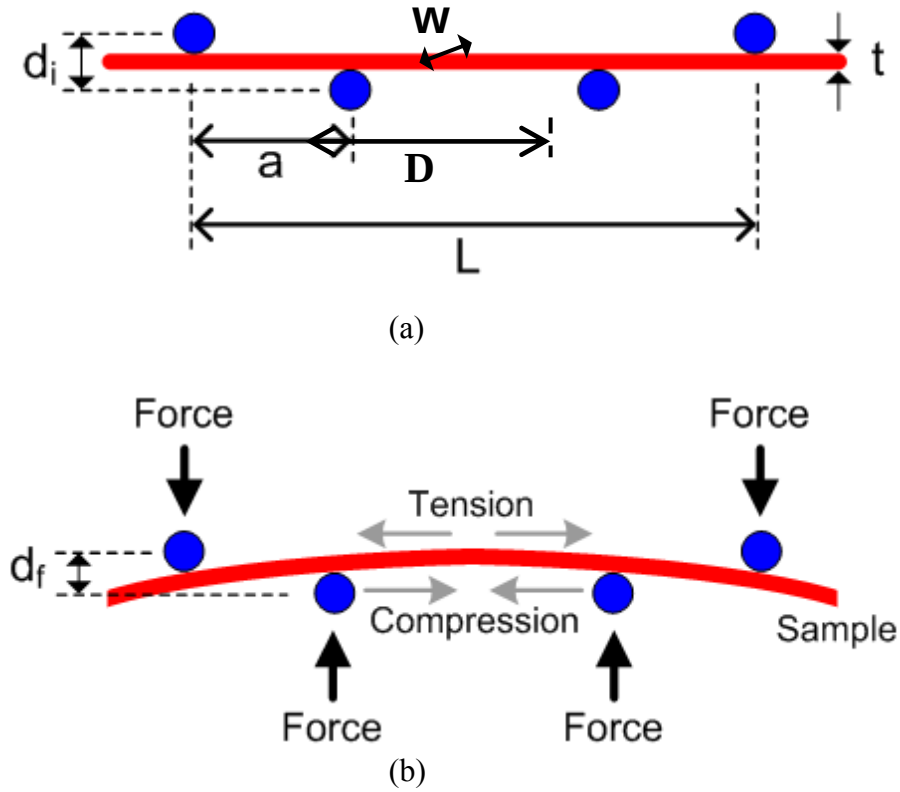

Figure 3-2. Illustration of a uniaxial wafer bending jig. The displacement (d) is defined as $d \equiv d_i - d_f$. (a) an unstressed sample (b) a stressed sample.

Another form of Eq. (3-1) fit for our experiments is found in some literatures [35, 36]:

$$\sigma = Y \cdot \varepsilon = Y \cdot \frac{t \cdot d}{2a\left(\frac{L}{2} - \frac{2a}{3}\right)}. \tag{3-2}$$

Here, σ and ε are the stress and strain values at the center of the sample respectively, Y is Young's modulus of Si along the stress direction, $a = \frac{L-D}{2}$, and the deflection d is the vertical displacement between the upper and lower plates of the uniaxial jig when we apply stress. In Fig. 3-2, d is defined as $d \equiv d_i - d_f$, and actually measured by the change in micrometer graduations. By analogy with the uniaxial jig, our ring-type biaxial jig has the same strain-deflection relation

if the inner (D) and outer support distances (L) are replaced by the diameters of the inner and outer concentric rings respectively, that is

$$\varepsilon_{ring} = \frac{t \cdot d}{2\left(R_{out} - R_{in}\right)\left(R_{out} - \frac{2\left(R_{out} - R_{in}\right)}{3}\right)}, \tag{3-3}$$

where $\varepsilon_{\text{ring}}$ is the strain value of the sample at the center of the concentric rings, and R_{in} and R_{out} are the radii of the inner and outer rings, respectively. Note that the stress σ_{ring} depends on its direction because Young's modulus of Si is not isotropic. Fig. 3-3 is a plot of Young's modulus as a function of direction ϕ in the (001) plane. The relation between Young's modulus and direction ϕ is given by [37]

$$Y(\phi) = \left[S_{11} + \left(S_{11} - S_{12} - \frac{S_{44}}{2} \right)\left(\cos^4\phi + \sin^4\phi - 1 \right) \right]^{-1}. \tag{3-4}$$

In general, the measured physical quantities by this ring-type biaxial jig are not directly converted to the values of an in-plane (x- and y-direction) biaxial stress. In other words, there is some conversion factor between these two types of stress. Let us consider two orthogonal stress vectors rotated by an angle of ϕ about the [001] axis as shown in Fig 3-4. This pair of stress vectors forms a new in-plane biaxial stress and the components of these two vectors are written as

$$\vec{\sigma}(\phi) = \sigma(\phi)\cdot\left(\cos\phi,\ \sin\phi,\ 0\right),\quad \vec{\sigma}(\phi + \pi/2) = \sigma(\phi)\cdot\left(-\sin\phi,\ \cos\phi,\ 0\right). \tag{3-5}$$

Using Eq. (2-7), we obtain second order stress tensor elements for each stress vector as follows:

$$\left(\sigma_{ij}(\phi)\right) = \sigma(\phi)\cdot\begin{pmatrix} \cos^2\phi & \sin\phi\cos\phi & 0 \\ \sin\phi\cos\phi & \sin^2\phi & 0 \\ 0 & 0 & 0 \end{pmatrix}, \tag{3-6}$$

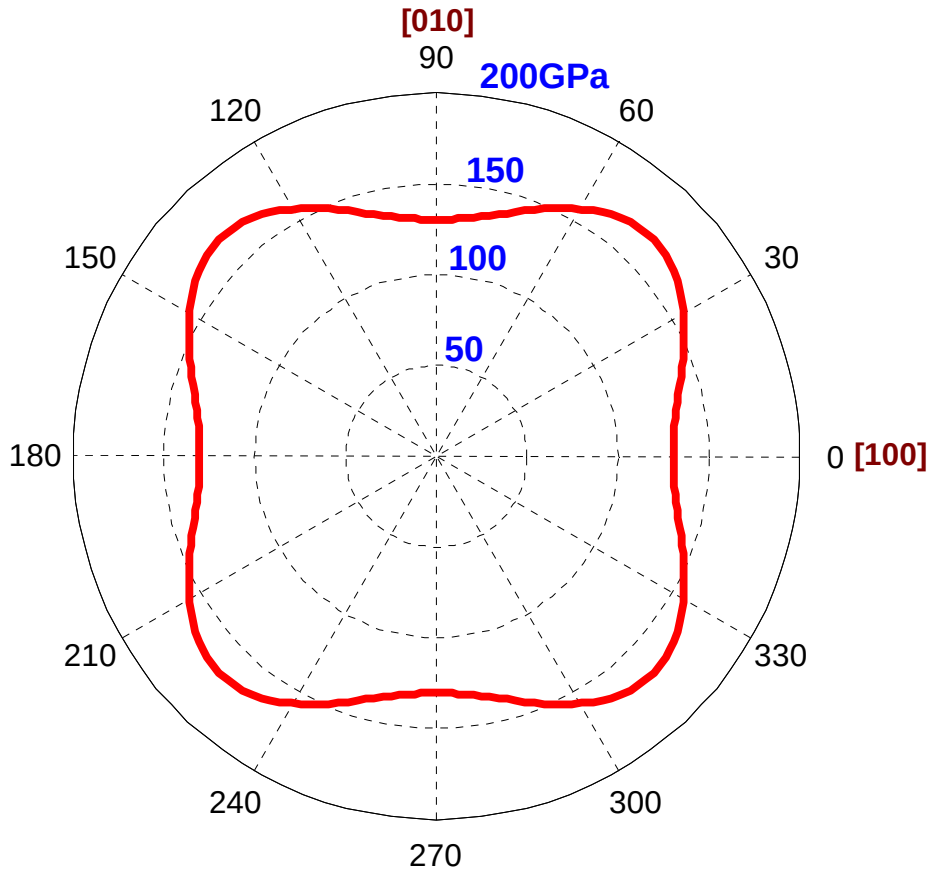

Figure 3-3. Young's modulus of Si versus direction ϕ in the (001) plane. The contours of the concentric circles correspond to a Young's modulus of 50, 100, 150, and 200 GPa.

$$\left(\sigma_{ij}(\phi+\pi/2)\right)=\sigma(\phi)\cdot\begin{pmatrix}\sin^2\phi & -\sin\phi\cos\phi & 0\\ -\sin\phi\cos\phi & \cos^2\phi & 0\\ 0 & 0 & 0\end{pmatrix}. \tag{3-7}$$

As previously done in Eq. (2-8), second order strain tensor components for each stress are expressed as,

$$\left(\varepsilon_{ij}(\phi)\right)=\sigma(\phi)\cdot\begin{pmatrix}S_{11}\cos^2\phi+S_{12}\sin^2\phi & S_{44}\sin\phi\cos\phi/2 & 0\\ S_{44}\sin\phi\cos\phi/2 & S_{12}\cos^2\phi+S_{11}\sin^2\phi & 0\\ 0 & 0 & S_{12}\end{pmatrix}, \tag{3-8}$$

$$\left(\varepsilon_{ij}(\phi+\pi/2)\right)=\sigma(\phi)\cdot\begin{pmatrix} S_{11}\sin^2\phi+S_{12}\cos^2\phi & -S_{44}\sin\phi\cos\phi/2 & 0 \\ -S_{44}\sin\phi\cos\phi/2 & S_{12}\sin^2\phi+S_{11}\cos^2\phi & 0 \\ 0 & 0 & S_{12} \end{pmatrix}. \tag{3-9}$$

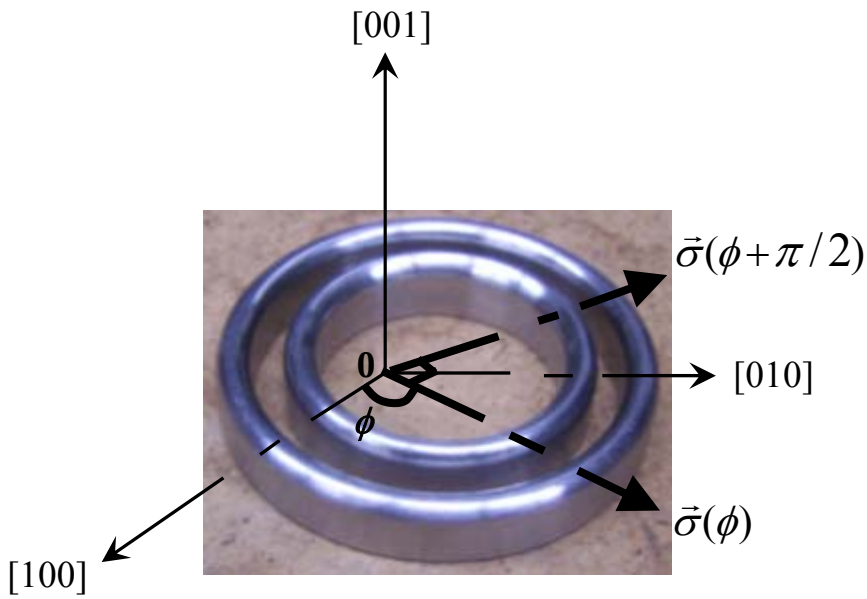

Figure 3-4. Illustration of a ring-type biaxial stress. The coordinate origin lies at the center of the concentric rings. Two orthogonal stress vectors form a new pair of biaxial stress.

Combining these two matrices of Eq. (3-8) and (3-9) results in

$$\left(\varepsilon_{ij}(\phi)\right)+\left(\varepsilon_{ij}(\phi+\pi/2)\right)=\sigma(\phi)\cdot\begin{pmatrix} S_{11}+S_{12} & 0 & 0 \\ 0 & S_{11}+S_{12} & 0 \\ 0 & 0 & 2S_{12} \end{pmatrix} \tag{3-10}$$

Finally, we obtain the strain components for a new biaxial stress, which have the same form as those of the in-plane (x- and y-direction) biaxial stress as we expected,

$$\varepsilon_{xx}^{bi}(\phi)=\varepsilon_{yy}^{bi}(\phi)=(S_{11}+S_{12})\sigma(\phi),\ \ \varepsilon_{zz}^{bi}(\phi)=2S_{12}\sigma(\phi). \tag{3-11}$$

Here note that $\varepsilon_{ii}^{bi}(\phi) \neq \varepsilon_{ii}^{bi}(0)$ for $i = x, y$, and z. Now, we can calculate the band edge shift in the conduction (or, valence) band using the expressions of Eq. (3-11) to compare the in-plane (x- and y-direction) biaxial stress. The band edge shift for Δ_2 valleys, from Eq. (2-12), is calculated as

$$\begin{aligned}\Delta E_{\Delta_2}^{(z)}\left(\sigma(\phi)\right) &= 2\Xi_u(S_{11}+2S_{12})\sigma(\phi)+2\Xi_d S_{12}\sigma(\phi) \\ &= \left[2\Xi_u(S_{11}+2S_{12})+2\Xi_d S_{12}\right]Y(\phi)\varepsilon(\phi).\end{aligned} \tag{3-12}$$

Since the strain is independent of stress directions as shown in Eq. (3-3), $\varepsilon(\phi) = \varepsilon(0)$ and $Y(0) = Y(\pi/2) = 1/S_{11}$ from Eq. (3-4). As a result, Eq. (3-12) can be rewritten as

$$\begin{aligned}\Delta E_{\Delta_2}^{(z)}\left(\sigma(\phi)\right) &= \left[2\Xi_u(S_{11}+2S_{12})+2\Xi_d S_{12}\right]Y(0)\varepsilon(0) \times \\ &\quad \left[1+\left(1-\frac{S_{12}}{S_{11}}-\frac{S_{44}}{2S_{11}}\right)\left(\cos^4\phi+\sin^4\phi-1\right)\right]^{-1} \\ &= \Delta E_{\Delta_2}^{(z)}\left(\sigma(0)\right)\cdot\left[1+\left(1-\frac{S_{12}}{S_{11}}-\frac{S_{44}}{2S_{11}}\right)\left(\cos^4\phi+\sin^4\phi-1\right)\right]^{-1}.\end{aligned} \tag{3-13}$$

In the relation, the term $\Delta E_{\Delta_2}^{(z)}\left(\sigma(0)\right)$ is the same as the Δ_2 band edge shift of an in-plane (x- and y-direction) biaxial stress and the additional term arises from the anisotropic property of Young's modulus of Si. Its minimum and maximum values are approximately 130 GPa at $\phi = 0°$ and 169 Gpa at $\phi = 45°$, respectively, and repeated every 90° as shown in Fig. 3-3. Considering this anisotropic property, we need to take an average value of $\Delta E_{\Delta_2}^{(z)}\left(\sigma(\phi)\right)$ as a meaningful quantity:

$$\begin{aligned}\left\langle \Delta E_{\Delta_2}^{(z)}\left(\sigma(\phi)\right)\right\rangle &= \Delta E_{\Delta_2}^{(z)}\left(\sigma(0)\right)\cdot\left\langle\left[1+\left(1-\frac{S_{12}}{S_{11}}-\frac{S_{44}}{2S_{11}}\right)\left(\cos^4\phi+\sin^4\phi-1\right)\right]^{-1}\right\rangle \\ &= \Delta E_{\Delta_2}^{(z)}\left(\sigma(0)\right)\cdot\frac{\int_0^{\frac{\pi}{2}}\left[1+\left(1-\frac{S_{12}}{S_{11}}-\frac{S_{44}}{2S_{11}}\right)\left(\cos^4\phi+\sin^4\phi-1\right)\right]^{-1}d\phi}{\int_0^{\frac{\pi}{2}}d\phi}\end{aligned} \tag{3-14}$$

Let us define the integral part in Eq. (3-14) as a conversion factor κ between the ring-type biaxial and in-plane biaxial stresses. κ is calculated to be 1.139. That means the ring-type biaxial stress causes a larger band edge shift by a factor of κ for the same strain. Since this difference comes from Young's modulus anisotropy alone, we can simply include this factor κ into the stress-strain relation of Eq. (3-2):

$$\sigma_{ring}^{bi}\left(\equiv\left\langle\sigma_{ring}^{bi}(\phi)\right\rangle\right)=\left\langle Y(\phi)\right\rangle\cdot\varepsilon_{ring}=\kappa\cdot\sigma_{in-plane}^{bi}. \tag{3-15}$$

The κ value of 1.139 is evaluated for a (001)-Si wafer, which can be neglected roughly, but for a (110)-Si wafer κ is expected to be larger since we have larger anisotropic values of Young's modulus [37]. The κ value for a (110)-wafer is calculated in the appendix B. During this proposal, however, we will only deal with a (001)-Si wafer, and actually all measurements have been made on (001)-wafer Si MOSFETs.

Strain Effect on Threshold Voltage

It is shown in Fig. 2-9 that the energy bandgap of Si is changed with strain. This bandgap change (specifically, bandgap narrowing) is a critical factor to affect MOSFET operation properties. In thermal equilibrium, the new bandgap causes charge carriers in the energy bands to additionally increase, and accordingly Fermi energy level will be adjusted to meet the charge neutrality condition.

Strain-Induced Fermi Energy Level Shift

In a non-degenerate p-type substrate, the mass action law (a product of the conduction and valence band charge carrier densities, *n* and *p*) under stress is stated, on the assumption that all the acceptor impurities are ionized, as

$$n(\sigma)p(\sigma)=n_i^2(\sigma)=n_i^2(0)\exp\left(-\frac{\Delta E_g(\sigma)}{kT}\right) \tag{3-16}$$

$$with\ \ p(0) \cong N_A\ \ and\ \ n(0) \cong \frac{n_i^2(0)}{N_A},$$

where "0'' in the parentheses represents zero stress, N_A is the p-type impurity doping density, and n_i is the intrinsic charge density. Based on Eq. (3-16), the additional charge Carriers, $\Delta n(\sigma)$ and $\Delta p(\sigma)$, generated by the bandgap narrowing are expressed as

$$\Delta n(\sigma) = \Delta p(\sigma) \cong \frac{n_i^2(0)}{N_A}\left[\exp\left(-\frac{\Delta E_g(\sigma)}{kT}\right) - 1\right], \tag{3-17}$$

$$with\ \ \Delta E_g(\sigma) < 0.$$

Even at a small stress, the minority charge carrier density, $n(\sigma)$, increases noticeably. For example, $\Delta n(\sigma) = \sim n(0)$ for an in-plane biaxial tension of 200 MPa. However, there is a negligible increase in the majority charge carrier density, or $p(\sigma) \cong N_A$. Note that the impurity doping density (N_A) is usually on the order of 10^{15}–10^{18} cm^{-3}, but the intrinsic charge density (n_i) is on the order of 10^{10} cm^{-3}. Hence, the new Fermi energy level is determined so that the minority carrier density increases and the majority carrier density remains unchanged. Under the invariance condition of the majority carrier density with stress [38, 39], or

$$p(\sigma) = N_V(\sigma) \cdot \exp\left(-\frac{E_F(\sigma) - E_V(\sigma)}{kT}\right) \cong N_A, \tag{3-18}$$

we obtain the following expression for Fermi energy level shift:

$$\Delta E_F(\sigma)\left(\equiv E_F(\sigma) - E_F(0)\right) = \Delta E_V(\sigma) + kT \cdot \ln\left[\frac{N_V(\sigma)}{N_V(0)}\right]. \tag{3-19}$$

Roughly speaking, if all the holes always remain at the valence band edge, the second term is not necessary, but in real case it is required to account for a carrier repopulation mechanism between the heavy- and light-hole bands due to the stress-induced band splitting [40] as explained in the section 2.2.1. In Eq. (3-19), the valence band effective density of states (N_V) is defined more

specifically in terms of density of state (DOS) heavy- and light-hole effective masses (m^*_{HH} and m^*_{LH}) [40]:

$$N_V = 2\left[2\pi kT/h^2\right]^{3/2}\left[\left(m^{*\,3/2}_{HH} + m^{*\,3/2}_{LH}\right)^{2/3}\right]^{3/2} \tag{3-20}$$

with a hole DOS effective mass $m^*_p \equiv \left(m^{*\,3/2}_{HH} + m^{*\,3/2}_{LH}\right)^{2/3}$,

where all the DOS effective masses are 3-dimentional (3-D) ones and quite different from 2-D or 1-D effective masses dealt with in a quantized potential well formed by a gate bias. Before stress is applied, the hole effective mass, $m^*_p(0)$, is represented as a sum of heavy- and light-hole effective masses, each with the same weighting factor. With increasing stress, $m^*_p(\sigma)$ gradually changes and finally will be one of the heavy- and light-hole effective masses depending on the stress type. For example, the light hole band is in lower energy state for in-plane biaxial tension, and all the heavy holes will transfer to the light hole band at infinite stress. As a result, the total hole effective mass will be a light hole effective mass. If stated more concisely,

$$m^*_p(\sigma) = \begin{cases} \left[m^*_{HH}(0)^{3/2} + m^*_{LH}(0)^{3/2}\right]^{2/3} & at\ zero\ stress \\ m^*_{HH}(\sigma)\ or\ m^*_{LH}(\sigma)\ \ at\ \sigma = \infty. \end{cases} \tag{3-21}$$

Also, the ratio of the heavy- and light-hole numbers are expressed at a certain stress level σ, based on a Maxwell-Boltzman distribution function for the non-degenerate valence energy band.

$$\frac{\#\ of\ HH}{\#\ of\ LH} \propto \exp\left(-\frac{\left|\Delta E^{Shear}_{HH}(\sigma)\right| + \left|\Delta E^{Shear}_{LH}(\sigma)\right|}{kT}\right) \equiv H_{hole}(\sigma) \tag{3-22}$$

for a lower energy state of the light hole band,

where $\Delta E_{HH}^{Shear}(\sigma)$ and $\Delta E_{LH}^{Shear}(\sigma)$ are band splitting energies for heavy- and light-hole bands.

For an in-plane biaxial stress as an example, $m_p^*(\sigma)$ is written, using Eq. (3-21) and (3-22), as follows [28]:

$$m_p^*(\sigma)=\begin{cases}\left[\left(H_{hole}(\sigma)\cdot m_{HH}^*(0)\right)^{3/2}+m_{LH}^*(0)^{3/2}\right]^{2/3} & for\ tension\\ \left[m_{HH}^*(0)^{3/2}+\left(H_{hole}(\sigma)\cdot m_{LH}^*(0)\right)^{3/2}\right]^{2/3} & for\ compression,\end{cases} \tag{3-23}$$

where $m_{HH}^*(0)=0.49m_0$ and $m_{LH}^*(0)=0.16m_0$.

Using the same procedure, we also obtain the following expressions for a non-degenerate n-type Si substrate:

$$\Delta E_F(\sigma)=\Delta E_C(\sigma)+kT\cdot\ln\left[\frac{N_C(0)}{N_C(\sigma)}\right], \tag{3-24}$$

$$N_C(\sigma)=2\left[2\pi kT/h^2\right]^{3/2}\left[\left(g_{\Delta_2}(\sigma)+g_{\Delta_4}(\sigma)\right)\cdot\sqrt{m_l m_t^2}\right], \tag{3-25}$$

$$\text{with}\quad g_{\Delta_2}(\sigma)+g_{\Delta_4}(\sigma)=\begin{cases}\left[g_{\Delta_2}(0)+H_{elec}(\sigma)\cdot g_{\Delta 4}(0)\right]\\ \qquad for\ \Delta_2\ valleys\ in\ lower\ energy\ state\\ \left[H_{elec}\cdot(\sigma)g_{\Delta_2}(0)+g_{\Delta 4}(0)\right]\\ \qquad for\ \Delta_4\ valleys\ in\ lower\ energy\ state.\end{cases} \tag{3-26}$$

Here, $g_{\Delta_2}(0)$ and $g_{\Delta 4}(0)$ are defined as zero stress degeneracy factors and related to the six-fold degeneracy factor (Δ_6) as follows:

$$g_{\Delta_6}(\sigma)=\begin{cases}g_{\Delta_2}(0)+g_{\Delta_4}(0)=6\ at\ \sigma=0\\ g_{\Delta_2}(\sigma)+g_{\Delta_4}(\sigma)=2,\ or\ 4\ at\ \sigma=\infty.\end{cases} \tag{3-27}$$

The repopulation factor for electrons, $H_{elec}(\sigma)$, is also represented similarly to that of holes in Eq. (3-22):

$$H_{elec}(\sigma) \equiv \exp\left(-\frac{\left|\Delta E^{(z)}_{\Delta_2\_Spl}(\sigma)\right| + \left|\Delta E^{(z)}_{\Delta_4\_Spl}(\sigma)\right|}{kT}\right) \propto \frac{\#\ of\ \Delta_4\ valley\ electrons}{\#\ of\ \Delta_2\ valley\ electrons} \tag{3-28}$$

for a lower Δ_2 *valley energy state.*

In Fig. 3-5, Fermi energy level shifts are plotted as a function of in-plane biaxial stress for both n- and p-type substrates together with each term of band edge shifts and DOS changes.

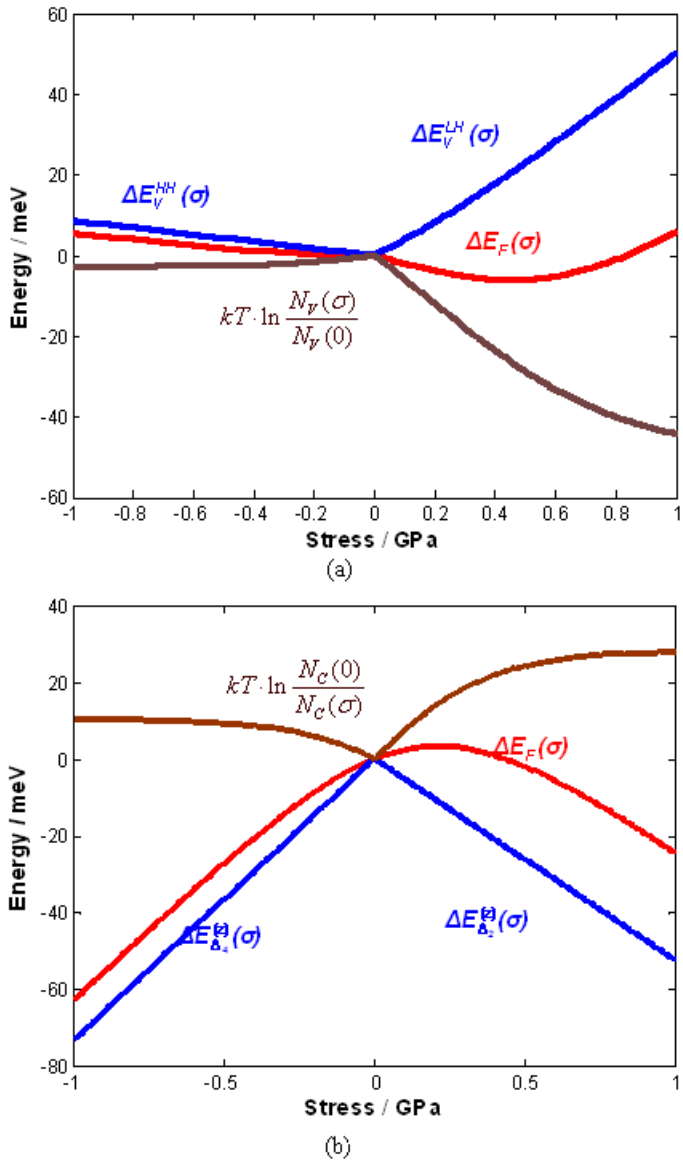

Figure 3-5. Fermi energy level shift vs. in-plane biaxial stress. (a) For an n-type substrate, the lowest energy state is a LH-band for tension and a HH-band for compression, respectively. (b) For a p-type substrate, the lowest energy state is a Δ_2 band for tension and a Δ_4 band for compression, respectively.

The band edges (lowest energy states) are Δ_2 and LH bands, respectively, for an n-type and a p-type substrate under tensile stress, and Δ_4 and HH bands under compressive stress.

Strain-Induced Threshold Voltage Shift

In this section, we briefly review the threshold voltage expressions for both uniaxially- and biaxially-strained n-MOSFETs. The formulas have been already obtained and published in [28, 41], but it would be worthwhile to comment on them because we have recently found some parts incorrect. As shown in [41], the threshold voltage (V_{th}) shift is expressed in terms of the flat-band voltage (V_{FB}) shift and surface potential (ψ_S) change:

$$q\Delta V_{th}(\sigma) = q\Delta V_{FB}(\sigma) + m \cdot \Delta\Psi_S(\sigma), \tag{3-29}$$

where m is the body effect coefficient and defined as $m = 1 + C_d / C_{ox}$ [40]. The ratio of the depletion capacitance to oxide capacitance (C_D / C_{OX}) depends on both Si-channel doping density and oxide thickness, but in general m lies between 1.1 and 1.4. If we neglect the strain effects on the oxide charge, $\Delta V_{FB}(\sigma)$ is directly related to $\Delta E_F(\sigma)'s$ in Eq. (3-19) and (3-44) as

$$q\Delta V_{FB}(\sigma) = \begin{cases} -\Delta E_F^{Gate}(\sigma) + \Delta E_F^{Si}(\sigma) = -\Delta E_C(\sigma) - kT\ln\dfrac{N_C(0)}{N_C(\sigma)} + \Delta E_V(\sigma) + kT\ln\dfrac{N_V(\sigma)}{N_V(0)} \\ \textit{for a nitride capping layered MOSFET} \\ \Delta E_F^{Si}(\sigma) = \Delta E_V(\sigma) + kT\ln\dfrac{N_V(\sigma)}{N_V(0)} \quad \textit{for a } Si/Si_{1-x}Ge_x \textit{ MOSFET}, \end{cases} \tag{3-30}$$

where the flatband voltage shift (ΔV_{FB}) is only a function of the work function difference between the polygate and Si substrate, and the two different expressions are attributed to the different device structures, whether the gate is stressed or not. It is also assumed that the strained poly-crystalline gate has the same (001) growth direction as that of the Si substrate, so applied stresses affect the same effects on the gate conduction band. The schematic energy band diagram for the n^+-polygate and p-type substrate is shown in Fig. 3-6. As derived in [40, 41], in order to

get the expression for $\Delta\Psi_S(\sigma)$ in terms of band parameters, we use the relation between the quantized inversion charge density and surface potential,

$$Q_{in}^{QM}(\sigma) \cong \frac{8\pi q \cdot kT \cdot m_{\Delta_2}^{2D}}{h^2 \cdot N_A} \cdot \frac{n_i^2(\sigma)}{N_C(\sigma)} \cdot \exp\left(\frac{-E_{\Delta_2}(\sigma)}{kT}\right) \cdot \exp\left(\frac{q\psi_S(\sigma)}{kT}\right), \tag{3-31}$$

where $m_{\Delta_2}^{2D}$ is the 2-D DOS effective mass and $E_{\Delta_2}(\sigma)$ is the lowest energy state in the inversion potential well. The wrong part in [41] is our assumption that the ground state energy (E_{Δ_2}) is not changed with stress, contrary to other literatures [13, 42]. Note in Eq. (3-31) that the total inversion charge density (Q_{in}^{QM}) has been approximated to that of the ground energy state since most electrons (particularly, in current short-channel devices) occupy the lowest energy state at a threshold voltage level and moreover, the ground and second lowest energy states are lowered and raised by a tensile stress, respectively. Fig. 3-7 illustrates the energy level shifts of the ground (E_{Δ_2}) and second lowest energy state (E_{Δ_4}) in the potential well for a tensile stress. In Eq. (3-31), taking the logarithm of both sides first and applying the same inversion charge condition at threshold before and after stress leads to:

$$\ln \frac{n_i^2(\sigma)/N_C(\sigma)}{n_i^2(0)/N_C(0)} + \frac{-\Delta E_{\Delta_2}(\sigma) + q\Delta\psi_S(\sigma)}{kT} = 0. \tag{3-32}$$

Here we need to notice the carrier density product term, $n_i^2(\sigma)$. As already stated in Eq. (3-16), the charge carrier densities (n and p) in the energy bands increase or decrease only through the energy bandgap change (ΔE_g). The strain-induced band splitting causes the carriers in each subband (Δ_2/Δ_4, or HH/LH subbands) to repopulate favorably in lower energy states, but does not change the carrier densities in real space.

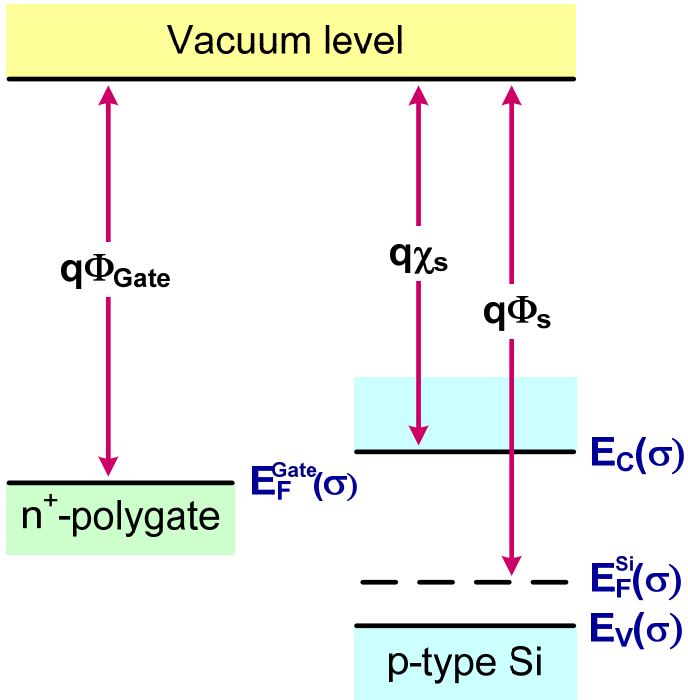

Figure 3-6. Energy band diagram of the n^+-polygate and p-type Si substrate. $q\Phi_{Gate}$ and $q\Phi_S$ are the work functions of the gate and substrate, respectively, and $q\chi_S$ is the electron affinity.

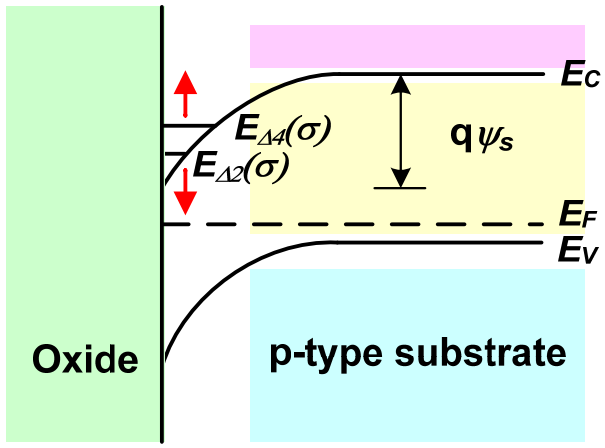

Figure 3-7. Lowest two energy levels of inversion electrons at the threshold voltage. Under uniaxial [110] or in-plane tensile stress, the ground and second lowest energy levels are shifted oppositely along the out-of-plane direction (field direction) as shown in the figure.

In conjunction with a unit of carrier densities (# of carriers per unit area or unit volume) as well, the carrier densities are not changed spatially since "repopulation" is only a carrier redistribution

process occurred in the energy domain. Another mistake has been made in this part [41]. As a result, $n_i^2(\sigma)$ is written as

$$n_i^2(\sigma) = n_i^2(0)\exp\left(-\frac{\Delta E_g(\sigma)}{kT}\right). \tag{3-33}$$

From Eq. (3-32) and (3-33), the surface potential change $(\Delta\psi_S)$ is expressed as

$$q\Delta\psi_S(\sigma) = \Delta E_g(\sigma) + \Delta E_{\Delta_2}(\sigma) + kT \cdot \ln\frac{N_C(\sigma)}{N_C(0)}. \tag{3-34}$$

Finally, plugging Eq. (3-30) and (3-34) into Eq. (3-29) yields the following threshold voltage shift expressions for uniaxial and biaxial strained n-MOSFETs,

$$q\Delta V_{th}(\sigma) = \begin{cases} \Delta E_V(\sigma) + kT\ln\frac{N_V(\sigma)}{N_V(0)} + m\Delta E_g(\sigma) + (m-1)\Delta E_C(\sigma) + (m+1)kT\ln\frac{N_C(\sigma)}{N_C(0)} \\ \textit{for a nitride capping layered n-MOSFET} \\ \Delta E_V(\sigma) + kT\ln\frac{N_V(\sigma)}{N_V(0)} + m\cdot\left[\Delta E_g(\sigma) + \Delta E_C(\sigma) + kT\ln\frac{N_C(\sigma)}{N_C(0)}\right] \\ \textit{for a } Si/Si_{1-x}Ge_x \textit{ n-MOSFET}, \end{cases} \tag{3-35}$$

where $\Delta E_{\Delta_2}(\sigma)$ has been replaced by $\Delta E_C(\sigma)$ since the ground energy level shift is equivalent to the conduction band edge shift for tensile stresses. Basically, these equations have been derived on the assumption that all the physical quantities vary linearly with stress, namely $\Delta x(\sigma) = x(\sigma) - x(0)$. Therefore, it is expected that they will be fitted better to a lower stress level. Each term in Eq. (3-35) reflects each physical phenomenon occurred in strained Si MOSFETs. The first two terms are introduced due to the Fermi energy level shift and account for the valence band offset and repopulation between HH and LH subbands. Symmetrically, the conduction band offset (or electron affinity change) and repopulation (between Δ_2 and Δ_4 subbands) terms are included in the formulas. Lastly, the bandgap change term, which causes the conduction

band carriers to increase, is also a main component. In Fig. 3-8, the physical phenomena occurred in strained MOSFETs are illustrated.

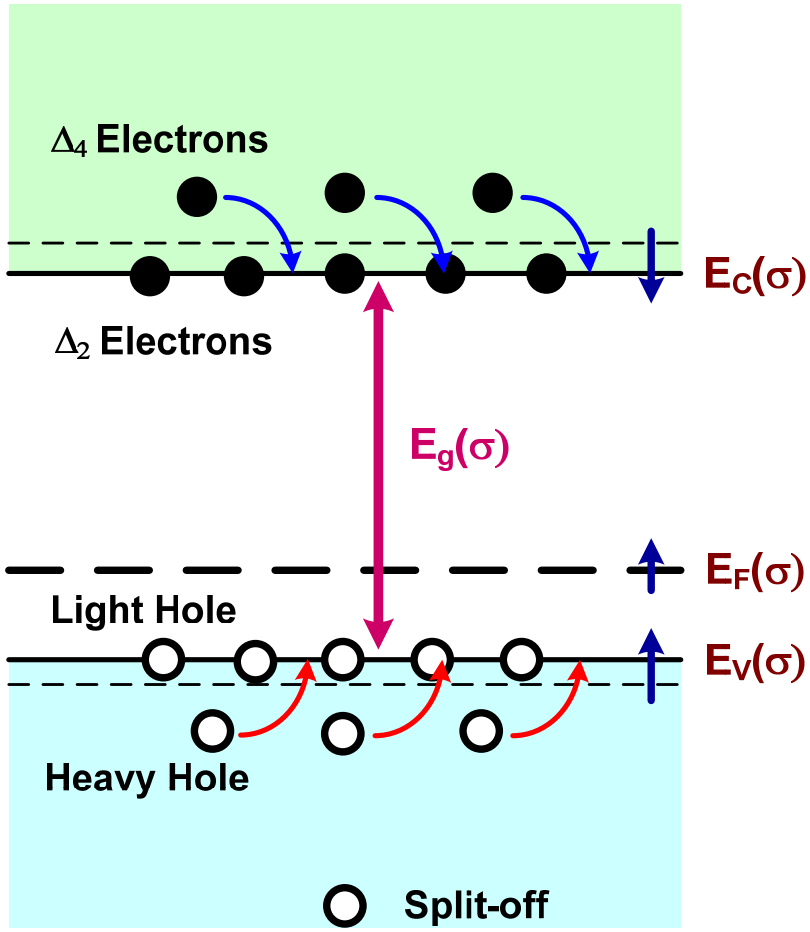

Figure 3-8. Illustration of each component constituting the threshold voltage shift formulas. The diagram is drawn based on an in-plane biaxial tension. Totally there are five components in the formulas, and each component corresponds to each physical phenomenon occurred in strained MOSFETs.

Results and Discussion

In order to check the validity of the newly corrected formulas of Eq. 3-35, let us first examine the electron occupancy in each energy state of the inversion layer at the threshold voltage. In Table 3-1, each portion of the electron populations in three lowest energy states is listed for different uniform substrate doping densities of N_A. At lower doping densities (N_A <

10^{17}cm^{-3}), electrons are more populated in the second lowest energy state (Δ_4 subband) than in the ground state (Δ_2 subband) due to the larger degeneracy factor $(g_{\Delta_2} = 2 \ vs. \ g_{\Delta_4} = 4)$ and the 2-D density of state effective mass $(m_{\Delta_2}^{2D} = 0.190m_0 \ vs. \ m_{\Delta_4}^{2D} = 0.417m_0)$. At $N_A = 10^{18}$ cm^{-3}, about 80 percent of the total inversion electrons occupy the ground energy state. Then, our formulas of Eq. 3-35 based on one band approximation should be best fit for $N_A = \sim 10^{18}$ cm^{-3} with a little substrate degeneracy. In addition, the directions in energy level shifts, as shown in Fig. 3-8, are a favorable factor for the formulas to become accurate.

Table 3-1. Electron population in three lowest energy states at the threshold voltage for a uniform substrate doping density of NA.

N_A [cm^{-3}]	E_S [V/cm]	$E_0(\Delta_2)$ [%]	$E_1(\Delta_4)$ [%]	$E_2(\Delta_2)$ [%]	Sum [%]
10^{15}	1.503×10^4	6.5	21.7	4.8	33
5×10^{15}	3.547×10^4	13.0	34.7	7.5	55.2
10^{16}	5.125×10^4	17.2	40	8.5	65.7
5×10^{16}	1.201×10^5	31.9	45.7	9.3	86.9
10^{17}	1.730×10^5	41.1	43.3	8.5	92.9
5×10^{17}	4.031×10^5	69.9	24.9	4.4	99.2
10^{18}	5.797×10^5	82.6	14.8	2.4	99.8
5×10^{18}	1.3448×10^6	98.2	1.6	0.2	100

*ES is the surface electric field right below the oxide layer. Lowest 60 energy levels have been involved in the calculation.

In Fig. 3-9, the threshold voltage shifts are plotted as a function of stress for both uniaxially- and biaxially-strained n-MOSFETs. The uniaxial data have been obtained by the wafer-bending experiments in which both the gate and Si-channel are stressed as in the case of tensile-strained capping layered MOSFETs. The n-MOSFETs used in the experiments have [110]-channel directions, and mechanical stresses are applied along the channel direction (longitudinal stresses). The biaxial data cited in the references are measured ones for tensile-strained $Si/Si_{1-x}Ge_x$ MOSFETs. In these Si-Ge heterostructured MOSFETs, the magnitude of internal stresses applied to the channel depends on Ge contents. For Ge-contents of x, the applied stress can be calculated as follows:

$$strain,\ \varepsilon = \frac{\left[(1-x)\cdot a_{Si} + x\cdot a_{Ge}\right] - a_{Si}}{a_{Si}}\ \ with\ lattice\ constants\ of\ a_{Si}\ and\ a_{Ge}$$

$$stress,\ \sigma = Y_{[100]}\cdot\varepsilon \cong 129\,GPa\cdot\frac{\left[(1-x)\cdot(54.3nm) + x\cdot(56.6nm)\right] - 54.3nm}{54.3nm}.$$

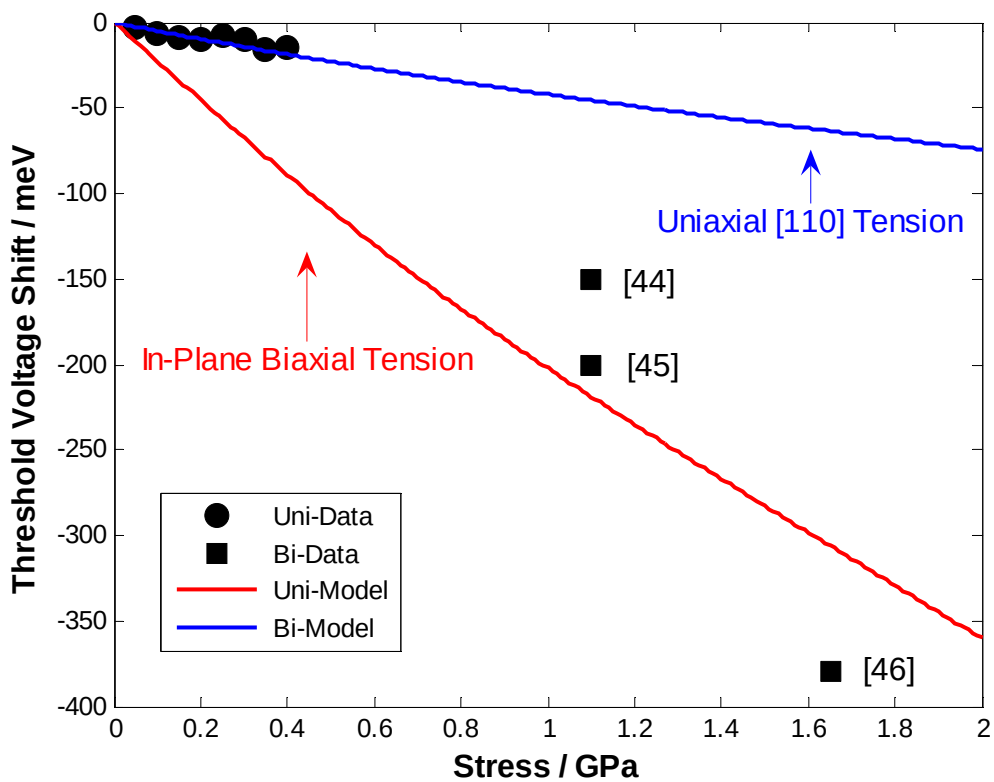

Figure 3-9. Threshold voltage shifts vs. stress. The plot has been made for tensile- strained n-MOSFETs at m = 1.3. The numbers in the square brackets represent the experimental data obtained in the references.

The three data used are for 20%- and 30%-Ge relaxed layers of MOSFETs, and the applied stress to each device channel is calculated as 1.1 GPa and 1.65 GPa, respectively. In plotting the models for both uniaxial and biaxial stresses, a field-induced repopulation effect has been considered. At the threshold voltage, all the valley electrons already split into Δ_2 and Δ_4 subbands in the inversion potential well. As shown in Table 3-1, more than 70 % inversion electrons are in the ground energy state for $N_A > 5\times10^{17}\text{cm}^{-3}$ even without stress. In consideration of this effect, the conduction band DOS term's (the fifth term in Eq. 3-35) contribution is limited

to its 20%. Even if our one band threshold voltage models seem rather rough, they agree well with the measured data as shown in Fig 3-9. More accurate and desirable models can be obtained simply by including a Δ_2–Δ_4 coupling term. Now, let us rewrite the total inversion charge density expression of Eq. (3-31) including the next lowest energy state [40].

$$Q_{in}^{QM}(\sigma) \cong \frac{8\pi qkT}{h^2 N_A} \cdot \frac{n_i^2(\sigma)}{N_C(\sigma)} \left[g_{\Delta_2} m_{\Delta_2}^{2D} \exp\left(\frac{-E_{\Delta_2}(\sigma)}{kT} \right) + g_{\Delta_4} m_{\Delta_4}^{2D} \exp\left(\frac{-E_{\Delta_4}(\sigma)}{kT} \right) \right] \times \exp\left(\frac{q\psi_S(\sigma)}{kT} \right) \tag{3-36}$$

A simple manipulation of Eq. (3-36) leads to

$$q\Delta\psi_S(\sigma) = \Delta E_g(\sigma) + \Delta E_{\Delta_2}(\sigma) + kT \cdot \ln \frac{N_C(\sigma)}{N_C(0)} + kT \cdot \ln \frac{\alpha_1(0) + \alpha_2(0) \exp\left(-\frac{\Delta E_{\Delta_4}(\sigma) - \Delta E_{\Delta_2}(\sigma)}{kT} \right)}{\alpha_1(0) + \alpha_2(0)}, \tag{3-37}$$

$$\textit{with} \;\; \alpha_1(0) = \exp\left(\frac{E_{\Delta_4}(0) - E_{\Delta_2}(0)}{kT} \right) \;\; \textit{and} \;\; \alpha_2(0) = \frac{g_{\Delta_4} \cdot m_{\Delta_4}^{2D}}{g_{\Delta_2} \cdot m_{\Delta_2}^{2D}}.$$

Comparing this new coupling term with the already existing DOS change term, $kT \cdot \ln \frac{N_C(\sigma)}{N_C(0)}$, we can find some similarity between them, that is

$$\begin{aligned} \ln \frac{N_C(\sigma)}{N_C(0)} &= \ln \frac{g_{\Delta_2} + H_{elec}(\sigma) \cdot g_{\Delta_4}}{g_{\Delta_2} + g_{\Delta_4}} \quad \text{from Eq.(3-24) through (3-28)} \\ &= \ln \frac{1 + H_{elec}(\sigma) \cdot \left[\left(g_{\Delta_4} \cdot m_{\Delta_4}^{3D} \right) / \left(g_{\Delta_2} \cdot m_{\Delta_2}^{3D} \right) \right]}{1 + \left(g_{\Delta_4} \cdot m_{\Delta_4}^{3D} \right) / \left(g_{\Delta_2} \cdot m_{\Delta_2}^{3D} \right)}, \text{ with } m_{\Delta_2}^{3D} = m_{\Delta_4}^{3D} = \sqrt[3]{m_x m_y m_z} \end{aligned} \tag{3-38}$$

for a lower energy state of Δ_2 subband,

and $$\ln\frac{\alpha_1(0)+\alpha_2(0)\exp\left(-\frac{\Delta E_{\Delta_4}(\sigma)-\Delta E_{\Delta_2}(\sigma)}{kT}\right)}{\alpha_1(0)+\alpha_2(0)}=\ln\frac{1+H_{elec}(\sigma)\cdot\left(\alpha_2(0)/\alpha_1(0)\right)}{1+\alpha_2(0)/\alpha_1(0)}$$

$$=\ln\frac{1+H_{elec}(\sigma)\cdot\left[\left(g_{\Delta_4}\cdot m_{\Delta_4}^{2D}\cdot e^{-E_{\Delta_4}(0)}\right)/\left(g_{\Delta_2}\cdot m_{\Delta_2}^{2D}\cdot e^{-E_{\Delta_2}(0)}\right)\right]}{1+\left[\left(g_{\Delta_4}\cdot m_{\Delta_4}^{2D}\cdot e^{-E_{\Delta_4}(0)}\right)/\left(g_{\Delta_2}\cdot m_{\Delta_2}^{2D}\cdot e^{-E_{\Delta_2}(0)}\right)\right]} \tag{3-39}$$

for a lower energy state of Δ_2 subband,

where the same definition has been used for the electron repopulation factor, $H_{elec}(\sigma)$, as in Eq. 3-28. The difference between Eq. (3-38) and (3-39) can be easily understood as two different repopulation mechanisms; one is a repopulation process occurred in the conduction band with no electric field (3-D repopulation), and the other is a repopulation process occurred in the quantized potential well under the gate field (2-D repopulation). The exponential terms in Eq. (3-39) can be defined as preoccupation factors (or the initial condition of a 2-D repopulation process) since they represent the relative occupation probabilities (or the relative initial energy levels) between the Δ_2- and Δ_4-subbands in the inversion layer before stress is applied. In a same sense, the preoccupation factors will be unity for a 3-D repopulation process, which means there is no band splitting between the subbands before stress. A strain gauge is a good example of the 3-D repopulation. Under the gate bias, two different repopulation processes (2-D and 3-D) are occurred simultaneously in strained MOSFETs, one in the conduction band and the other in the valence band. Fig. 3-10 shows the analogy between the 2-D and 3-D repopulation processes and their related parameters. Note that the effective masses of Δ_2- and Δ_4-subbands are the same for a 3-D repopulation process, but different for a 2-D one, that is

$$m_{\Delta_2}^{2D}=\sqrt{m_x m_y}=0.19m_0,\ m_{\Delta_4}^{2D}=\sqrt{m_y m_z}=0.92m_0,\ and\ m_{\Delta_2}^{3D}=m_{\Delta_4}^{3D}=\sqrt[3]{m_x m_y m_z}. \tag{3-40}$$

Now, we can obtain a more accurate two-band model from the one band model, simply by replacing the 3-D repopulation term (the fifth term in Eq. 3-35) with a 2-D one. This two-band model should be applied to MOSFETs with lower substrate doping densities such as $N_A < 10^{17}$ cm^{-3} beyond the coverage of the one-band model. A three-band model can be also easily made. This time, however, we have to add another 2-D repopulation term to the existing five components of the two-band model instead of replacing it. For example, a three-band model has the following form:

$$q\Delta\psi_S(\sigma) = \Delta E_g(\sigma) + \Delta E_{\Delta_2}(\sigma) + kT \cdot \ln \frac{\alpha_1(0) + \alpha_2(0)\exp\left(-\frac{\Delta E_{\Delta_4}(\sigma) - \Delta E_{\Delta_2}(\sigma)}{kT}\right)}{\alpha_1(0) + \alpha_2(0)} +$$

$$kT \cdot \ln \frac{\alpha_1'(0) + \alpha_2'(0)\exp\left(-\frac{\Delta E_{\Delta_2}(\sigma) - \Delta E_{\Delta_2}(\sigma)}{kT}\right)}{\alpha_1'(0) + \alpha_2'(0)}. \qquad (3\text{-}41)$$

$$with \;\; \alpha_1'(0) = \exp\left(\frac{E_{\Delta_2}'(0) - E_{\Delta_2}(0)}{kT}\right) \;\; and \;\; \alpha_2'(0) = \alpha_2(0) = \frac{g_{\Delta_4} \cdot m_{\Delta_4}^{2D}}{g_{\Delta_2} \cdot m_{\Delta_2}^{2D}}.$$

Interestingly, this new term is zero since the third lowest energy state is the same kind of Δ_2 subband as the ground energy state, and thus has the same band splitting energy. For the same reason, we do not have five-, seven-, and nine-band models and etc. Here, we notice that there is no repopulation among Δ_2 subbands, or among Δ_4 subbands. A four-band model has non-zero sixth term in addition to the five components of the two-band model. The sixth term is of the same form as that of the 2-D repopulation term of the two-band model with the following initial coefficients:

$$\alpha_1''(0) = \exp\left(\frac{E_{\Delta_4}'(0) - E_{\Delta_2}(0)}{kT}\right) \;\; and \;\; \alpha_2''(0) = \alpha_2(0) = \frac{g_{\Delta_4} \cdot m_{\Delta_4}^{2D}}{g_{\Delta_2} \cdot m_{\Delta_2}^{2D}}. \qquad (3\text{-}42)$$

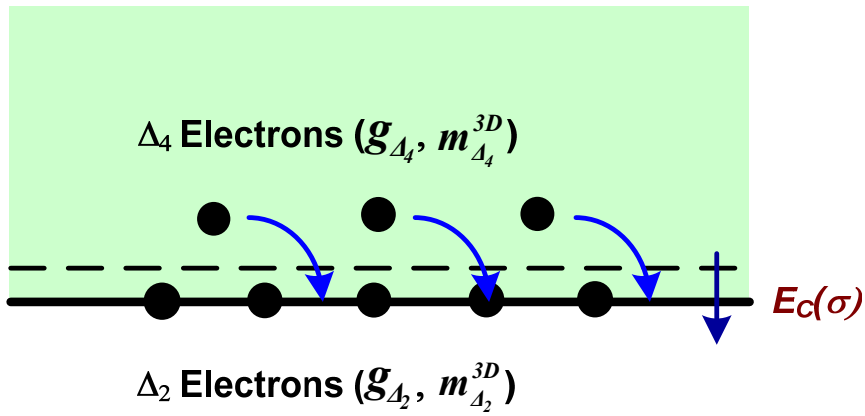

(a)

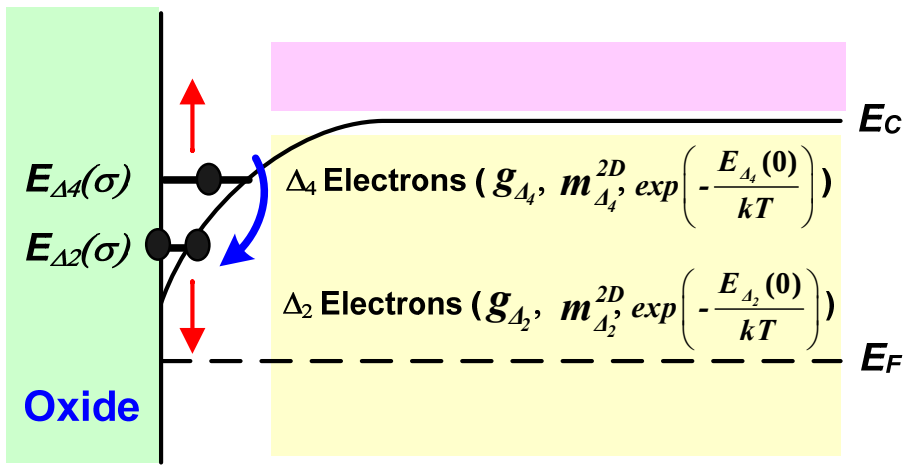

(b)

Figure 3-10. Illustration of 2-D and 3-D repopulation processes occurred in the conduction band edges under uniaxial [110] or in-plane tensile stress. (a) In a 3-D process, 3-D parameters (degeneracy factors and 3-D DOS effective masses) are related. (b) In a 2-D process, which is occurred under gate bias, in addition to the 2-D parameters (degeneracy factors and 2-D DOS effective masses) preoccupation factors are involved, and they determine their initial energy levels in the inversion layer before stress is applied.

Similarly, the six-band model has non-zero seventh term in addition to the six components of the four-band model. The seventh term is all the same as the sixth term of the four-band model except for

$$\alpha_1^{'''}(0) = \exp\left(\frac{E^{''}_{\Delta_4}(0) - E_{\Delta_2}(0)}{kT}\right). \tag{3-43}$$

The six-, eight-, ten-band models, and etc. can be made repeatedly simply by adding one more 2-D repopulation term at a time with a corresponding initial energy level in the constant $\alpha_1^{(n)}(0)$. The initial energy levels can be also determined quite accurately based on the energy eigenvalue formula obtained from the triangular potential well approximation [40].

$$E_j = \left[\frac{3hqE_s}{4\sqrt{2m^z_{\Delta_2/\Delta_4}}} \left(j + \frac{3}{4} \right) \right]^{2/3}, \quad j = 0,1,2,..... \tag{3-44}$$

Note that the energy eigenvalues of this formula are very accurate at the threshold voltage level unlike in the strong inversion region. The surface electric field (E_s) is also given by [40]

$$E_s = \frac{|Q_{d,\max}|}{\varepsilon_S} = \left. \frac{[2\varepsilon_S q N_A \psi_S]^{\frac{1}{2}}}{\varepsilon_S} \right|_{\psi_S = 2(kT/q)\ln(N_A/n_i)} = 2\left[\frac{N_A kT}{\varepsilon_S} \ln \frac{N_A}{n_i} \right]^{\frac{1}{2}}. \tag{3-45}$$

Using Eq. (3-44) and (3-45), we can determine the initial energy levels of all Δ_2- and Δ_4-subbands for each 2-D repopulation term, and thus easily produce any order of n-MOSFET threshold voltage shift models no matter how large they are. A model containing more subbands will be better fitted, especially for lower substrate doping MOSFETs since their subband energy levels are located more closely in the inversion potential well due to lower surface electric fields as shown in Table. 3-1.

Summary

The threshold voltage shift models applicable to both uniaxially- and biaxially-strained n-MOSFETs have been reviewed and corrected based on the already published papers [28, 41]. Each model contains five components, each component representing its corresponding physical phenomenon occurred in the strained MOSFETs. The existence of the two components (the valence band offset and subband repopulation terms) is attributed to the majority carrier charge neutrality condition. The other three components (the energy bandgap change, conduction band

offset and subband repopulation terms) are required to account for the change in the inversion charge carriers. First, the energy bandgap change (bandgap narrowing) causes each subband carrier density to increase. Unlike in the valence band, the inversion carrier densities of the conduction subbands are not so high at the threshold voltage level that even a small bandgap change brings about non-negligible increase in the carrier density of each subband, hence making the threshold voltage (V_{th}) lower. The conduction band offset, which is equivalent to the ground energy level shift in the inversion layer for tension, also affect the threshold voltage. For example, the downshift of the conduction band offset lowers V_{th} as in a tensile stress, while the upshift raises it as in a compressive stress. Lastly, the 2-D repopulation term causes V_{th} to be lowered or raised depending on the carrier transfer direction. The concept of 2-D and 3-D repopulation processes has been introduced, based on which we can build up the multiband threshold voltage shift models easily in a repetition way. Especially, the multiband models are required to precisely describe the threshold voltage shift for p-MOSFETs. Fig. 3-11 shows two types of strained p-MOSFETs which are commonly adopted in the industry as a standard. Since HH and LH out-of-effective masses are similar as listed in Table 2-3, their energy levels are formed very closely in the inversion layer at the threshold voltage level. For example, it is calculated using the out-of-plane effective masses in Table 2-3 that the two lowest energy level differences are only ~10meV and ~20meV for a uniaxial [110] and an in-plane biaxial stress, respectively, at a doping density of ~ 10^{18} cm^{-3} (compared with ~80meV for n-MOSFETs at the same condition). Note that hole effective masses are dependent upon a stress type.

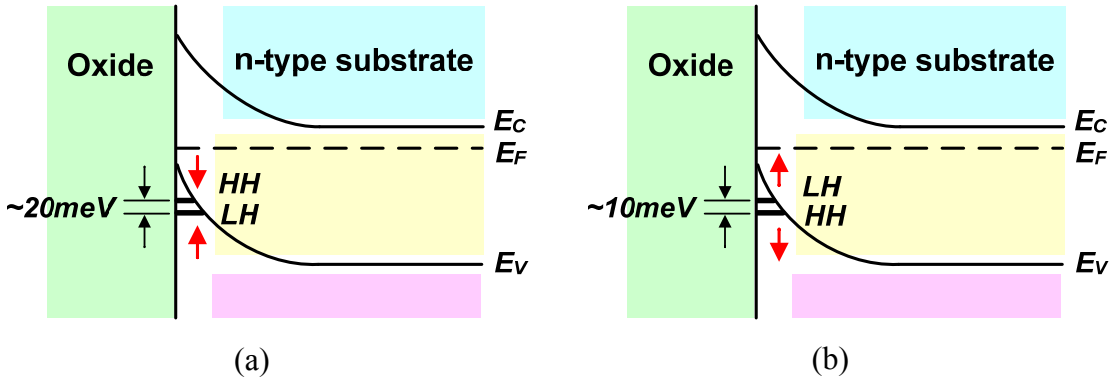

Figure 3-11. Two types of strained p-MOSFETs commonly adopted in the industry as a standard. (a) In-plane tensile-strained and (b) uniaxially compressive-strained p-MOSFETs are shown to have their lowest two subband energy levels closely located each other at the threshold voltage level due to similar HH and LH out-of-plane effective masses.

CHAPTER 4
STRAIN EFFECT ON GATE TUNNELING CURRENT

Strain effects on the energy bands in Si MOSFETs were shown to be classified into two main categories. One is the bandgap narrowing effect which causes the minority carriers to increase in the energy subbands, thus affecting the device operation properties such as threshold voltage shift. The others are the band edge shifts and splitting. These effects make the charge carriers repopulate favorably in lower energy states. In this chapter, we discuss how strain affects and alters the gate tunneling current, especially in the region where the gate is biased above the threshold voltage ($V_G > V_{th}$), and also introduce an experimental method of determining deformation potential constants for n-MOSFETs. Unlike in the subthreshold voltage region, the inversion charge carriers start to abruptly increase beyond the threshold voltage, so that we can neglect the charge carriers generated by the bandgap narrowing in the strong inversion region. Instead, the subband energy level shift and the repopulation between the subbands are dominant mechanisms to account for the change in the gate tunneling current with strain.

Measurement of Direct Tunneling Current

Measurements on the gate tunneling currents have been made for both n- and p-MOSFETs, with the drain, source, and body all tied to ground and the gate positively-biased using a Keithley 4200 DC characterization system, under all types of mechanical stresses; uniaxial and biaxial, longitudinal and transverse, and compressive and tensile. The stresses were applied to measure the industrial long channel devices ranging from 1 μm to 4 μm, using the four-point bending jig for a uniaxial stress and the ring-type jig for a biaxial stress, as shown in Fig. 3-1. The n- (or p-) MOSFET samples used consist of arsenic doped n^+ (or p^+) poly Si gate on top of 1.3nm nitrided SiO_2 gate dielectric on ~10^{17} cm^{-3} boron doped p (or n) well. In Fig 3-2, the measured data at a gate voltage of 1.0 V are plotted as a function of the applied stress [20]. Under all types of tensile

stresses, the hole and electron gate direct tunneling (DT) current increases and decreases, respectively, while the trend is opposite under compressive stresses.

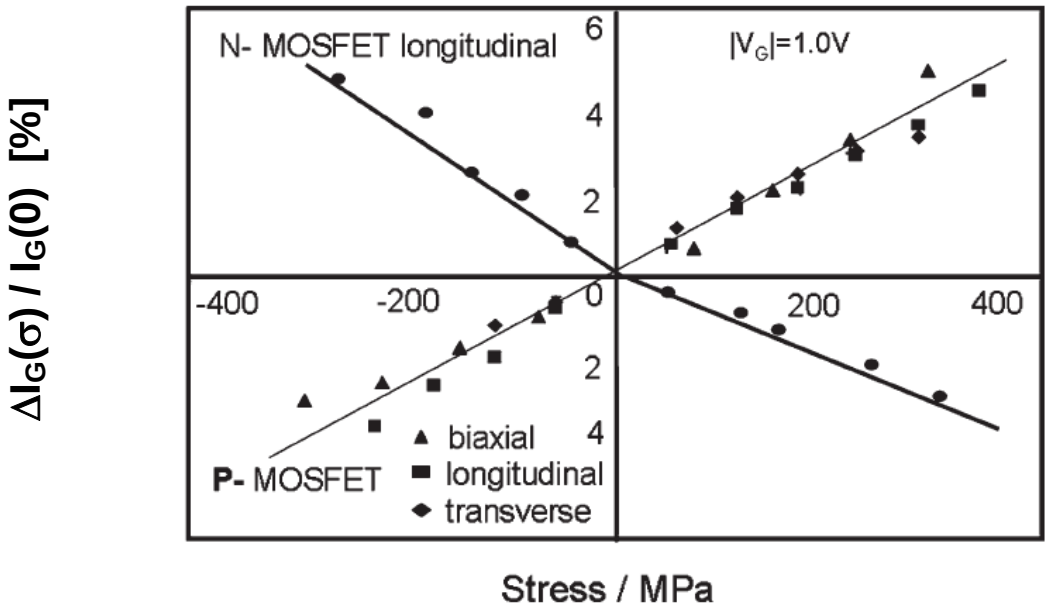

Figure 4-1. Change in n- and p-MOSFET gate tunneling current versus stress [20]. All types of tensile stresses increase the hole gate tunneling current, while decrease the electron gate tunneling current. For compressive stresses, the trend is opposite.

Direct Tunneling Current Model from Inversion Electron

Before modeling the gate tunneling current, we explain qualitatively the experimentally observed trend in both n- and p-MOSFETs. In the strong inversion region (e.g., $V_G = 1.0$ V as in the plot), the charge carrier density is high enough to neglect the electron-hole pair carriers created by the strain-induced bandgap narrowing. Therefore, the strain effects left to affect the inversion charge carriers are the subband energy level shift, repopulation and Fermi level shift as explained in Chapter 3.

Explanation for Direct Tunneling Current Change with Stain

To simplify our analysis, consider only the lowest two energy levels ($\mathcal{E}_0$, $\mathcal{E}_1$) in the inversion layer. In n-MOSFETs, the electron tunneling current decreases for tensile stress since the $\mathcal{E}_0$ state (Δ_2 subband) lowers as shown in Fig. 3-7, thus making Δ_2 subband electrons bound in

a higher potential barrier as well as decreasing the population in $\mathcal{E}_1$ state (Δ_4 subband with higher tunneling probability) through repopulation. Reversely for compressive stress, the electrons in $\mathcal{E}_0$ are in a lower potential barrier and the population in $\mathcal{E}_1$ increases, which causes the tunneling current to increase. It is also expected that Fermi level shift alters the tunneling current by affecting the inversion charge carriers. As stated in the mass action law of Eq. 3-16, the carrier density, $n(\sigma)$, is not changed with Fermi level shift, but the carrier population in each subband will be altered. When Fermi level moves toward the conduction band, the relative electron population (# in $\mathcal{E}_1$ / # in $\mathcal{E}_0$) increases. This effect increases the tunneling current slightly. In p-MOSFETs, the tunneling current change is somewhat complicated to explain since the out-of-plane effective masses vary not only with the magnitude of applied stresses [4, 7], but with the stress type as shown in Table 2-3. According to the calculation results in Table 2-3, the out-of-plane effective masses are as follows:

$$HH / LH = \begin{cases} 0.28m_0 / 0.20m_0 & \textit{for an in-plane biaxial stress} \\ 0.21m_0 / 0.26m_0 & \textit{for a uniaxial } [110] \textit{ stress.} \end{cases} \tag{4-1}$$

Fig. 4-2 shows the ground and second lowest energy states in the inversion potential well where the ground energy state is a heavy-hole (light-hole) band for an in-plane biaxial stress (a uniaxial [110] stress) since the out-of-plane effective mass of the HH (LH) is heavier. When compressive stress is applied, HH ↑ (↓) and LH ↓ (↑) for a biaxial (uniaxial) stress as shown in the figure. These subband energy shifts cause the tunneling current in p-MOSFETs to decrease for both uniaxial and biaxial stresses. On the other hand, HH ↓ (↑) and LH ↑ (↓) for a biaxial (uniaxial) tension, which increases the tunneling current. Our tunneling current model for p-MOSFETs explains this trend well [45].

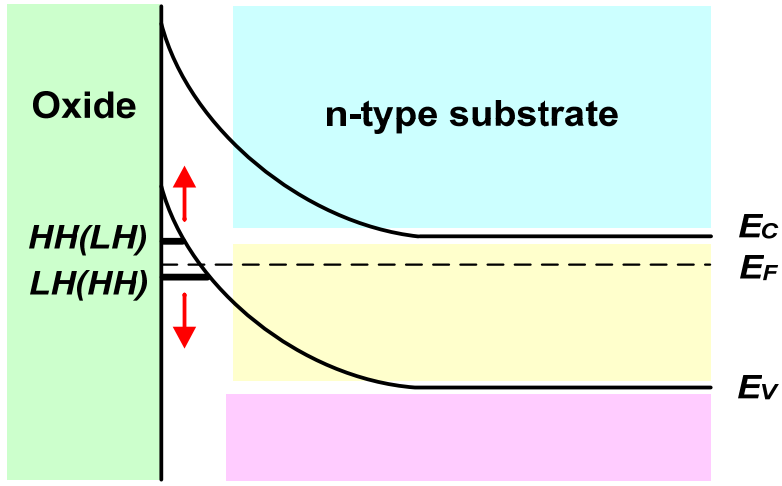

Figure 4-2. Ground and second lowest energy states of p-MOSFETs in the inversion potential well. A heavy-hole (light-hole) band is a ground energy state for an in-plane biaxial (a [110] uniaxial) stress. The arrow directions represent the subband energy level shift under compressive stress.

Physical Model for Direct Tunneling Current in n-MOSFET

It has been previously reported that stress alters the gate tunneling currents on both (001) n- and p-MOSFETs, with tensile stress typically used for n-MOSFETs [46]. For the purpose of deformation potential measurements, however, we use compressive stress since electrons primarily only populate the lowest two energy levels under this condition. In other words, the electron population of the Δ_2 valley next lowest subband, $E'_{\Delta_2}(\sigma)$, is negligible under compressive stress, which simplifies the interpretation of the tunneling current data. A schematic drawing of the direct tunneling process from the Δ_2 and Δ_4 subbands and the effect of stress on the subband energies are shown in Fig. 4-3. The direct tunneling electron current density J_G can be expressed in terms of the charge density (N_{ij}) and lifetime (τ_{ij}) of each energy subband in the inversion layer [47, 48], which are functions of stress, σ,

$$J_G(\sigma) = \sum_{i,j} \frac{qN_{ij}(\sigma)}{\tau_{ij}(\sigma)}, \tag{4-2}$$

where the subscript i denotes Δ_2 (or Δ_4) valley and j each subband belonging to one of these two valleys, respectively. When stress is applied, the change of tunneling current density $\Delta J_G(\sigma)$ is written as,

$$\Delta J_G(\sigma) = \sum_{i,j}\left[\frac{\partial J_G}{\partial N_{ij}}\Delta N_{ij}(\sigma) + \frac{\partial J_G}{\partial \tau_{ij}}\Delta\tau_{ij}(\sigma)\right]. \tag{4-3}$$

Above the threshold voltage, most electrons (e.g., ~90% at $V_G = V_{th}$ and $N_A = \sim 10^{17}$ cm^{-3} as shown in Table 3-1) occupy the lowest two energy states, or each ground state for Δ_2 and Δ_4 valleys as shown in Fig. 4-3.

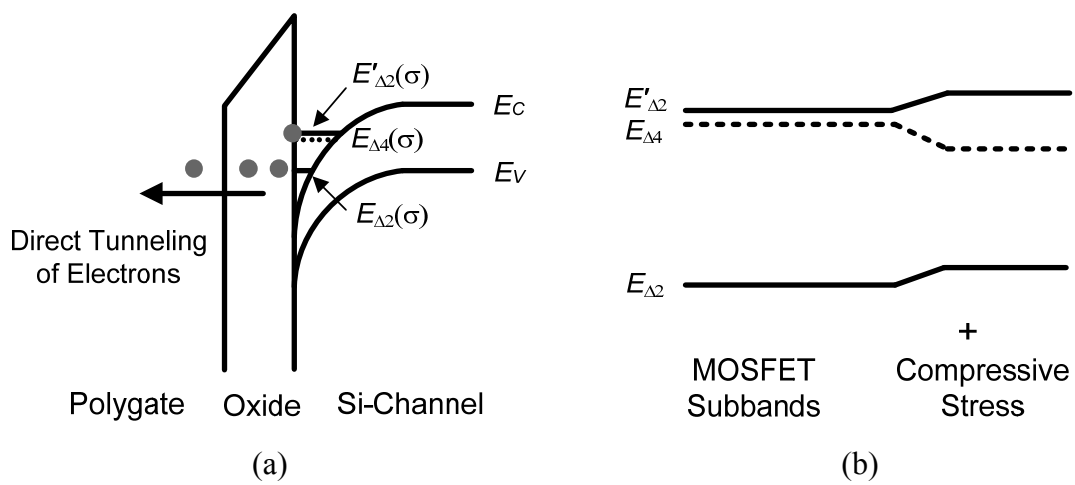

Figure 4-3. (a) Schematic band diagram for the gate direct tunnel current in an n-MOSFET on a (100)-wafer. (b) Δ_2 and Δ_4 energy level shifts under compressive stress and MOSFET inversion layer confinement. Under compressive stress, Δ_2 energy levels are raised while Δ_4 energy level (dotted line) is lowered.

From Eq. 4-2, the relative change of tunneling current $\Delta I_G(\sigma)/I_G(0)$, referenced at zero stress, is calculated as follows, to first order in $\Delta\tau(\sigma)/\tau(0)$,

$$\frac{\Delta I_G(\sigma)}{I_G(0)} \cong A(0)\frac{\Delta N_{\Delta 4}(\sigma)}{N_{\Delta 4}(0)} - B(0)\frac{\Delta\tau_{\Delta 2}(\sigma)}{\tau_{\Delta 2}(0)} - C(0)\frac{\Delta\tau_{\Delta 4}(\sigma)}{\tau_{\Delta 4}(0)}, \tag{4-4}$$

where $A(0) = \dfrac{-1+\tau_{\Delta 2}(0)/\tau_{\Delta 4}(0)}{N_{\Delta 2}(0)/N_{\Delta 4}(0)+\tau_{\Delta 2}(0)/\tau_{\Delta 4}(0)}$, $B(0) = \dfrac{N_{\Delta 2}(0)/N_{\Delta 4}(0)}{N_{\Delta 2}(0)/N_{\Delta 4}(0)+\tau_{\Delta 2}(0)/\tau_{\Delta 4}(0)}$, and

$C(0) = \dfrac{N_{\Delta 4}(0)/N_{\Delta 2}(0)}{N_{\Delta 4}(0)/N_{\Delta 2}(0)+\tau_{\Delta 4}(0)/\tau_{\Delta 2}(0)}$.

Note in the approximation we use $\Delta N_{\Delta 2}(\sigma) + \Delta N_{\Delta 4}(\sigma) \cong 0$ (neglecting higher subbands), and assume linear relationships for parameters, τ and N, are valid since the applied stresses are small (<300 MPa). The approximation has been checked numerically and introduced little error. The tunneling lifetimes of the electrons in each Δ_2 and Δ_4 ground state under compressive [110] stress are given by [47]:

$$\tau_{\Delta 2/\Delta 4}(\sigma) = \frac{1}{T_{\Delta 2/\Delta 4}(\sigma)} \frac{\pi\hbar}{E_{\Delta 2/\Delta 4}(\sigma)}, \tag{4-5}$$

and quantized energy levels, $E_{\Delta_2}(\sigma)$ and $E_{\Delta_4}(\sigma)$, are expressed, using Table 2-2 and Eq. (3-44), as

$$E_{\Delta_2}(\sigma) = \left(\frac{9hqF_{eff,\Delta 2}}{16\sqrt{2m^*_{\Delta 2}}}\right)^{2/3} + (\Xi_d + \frac{\Xi_u}{3})(S_{11}+2S_{12})\sigma + (\frac{\Xi_u}{3})(S_{12}-S_{11})\sigma, \tag{4-6}$$

$$E_{\Delta_4}(\sigma) = \left(\frac{9hqF_{eff,\Delta 4}}{16\sqrt{2m^*_{\Delta 4}}}\right)^{2/3} + (\Xi_d + \frac{\Xi_u}{3})(S_{11}+2S_{12})\sigma - (\frac{\Xi_u}{6})(S_{12}-S_{11})\sigma, \tag{4-7}$$

where $T_{\Delta 2/\Delta 4}(\sigma)$ is the transmission probability of a modified WKB method [47, 48], and the quantization effective masses, $m^*_{\Delta 2} = 0.92m_0$ and $m^*_{\Delta 4} = 0.19m_0$, and the elastic compliance constants, $S_{11} = 7.68\times10^{-12}$ m^2/N and $S_{12} = -2.14\times10^{-12}$ m^2/N. In the above expressions, the 2nd and 3rd terms are hydrostatic and shear strain components, respectively, and the stress, σ, has negative values for compression, but the plots (Fig. 4-4 and 4-6) are made on a positive scale for

convenience. The effective electric fields ($F_{eff,\Delta 2}$ and $F_{eff,\Delta 4}$) are introduced into our model to compensate for triangular potential approximation errors in the inversion condition,

$$F_{eff,\ \Delta 2/\Delta 4} = \frac{Q_{d,\max} + \eta_{\Delta 2/\Delta 4} Q_{inv}}{\varepsilon_{Si}}, \tag{4-8}$$

where $Q_{d,max}$ is the maximum depletion sheet charge density, Q_{inv} is the inversion sheet charge density, and ε_{Si} is the Si dielectric constant. The correction factors used in our model are $\eta_{\Delta 2}$= 0.75 [48], and $\eta_{\Delta 4}$= 1 [47]. Figures 4-4 (b)-(d) show which terms in Eq. (4-4) contribute to the change in the gate leakage at low and high gate voltage. At low gate biases, the stress-induced repopulation term, the 1st term in Eq. (4-4), contributes greatly to tunnel current as shown in Fig. 4-4 (b), while its effect reduces gradually as the gate bias increases as shown in Fig. 4-4 (c) and (d).

Extraction of Conduction Band Deformation Potential Constant

Stress alters the tunneling current in two ways: (1) Stress-induced energy level splitting causing a repopulation between Δ_2 and Δ_4 subbands as shown in Fig 4-5. The life time of Δ_2 subband is significantly longer due to the high out-of-plane mass ($0.92m_0$ vs. $0.19m_0$). (2) The shift in the energy levels alters the SiO_2/Si barrier height. The change in the gate current versus applied compressive stress for different gate voltages is shown in Fig. 4-4 (a). We observe the change, $\Delta I_G(\sigma)/I_G(0)$, is positive (increases) and is larger at low gate voltage. At high gate voltage, the change is a weak function of voltage. Both of these trends can be understood from how the vertical electric field and compressive stress shift and split the energy levels. At high gate voltage (high vertical field), Δ_2 is many kT below Δ_4, electron primarily populating Δ_2 subband. Hence at high gate voltage, a smaller change in the tunneling current results since compressive stress only alters the gate current by lowering the SiO_2/Si barrier height (shifting Δ_2 to higher energy as seen in Fig. 4-3).

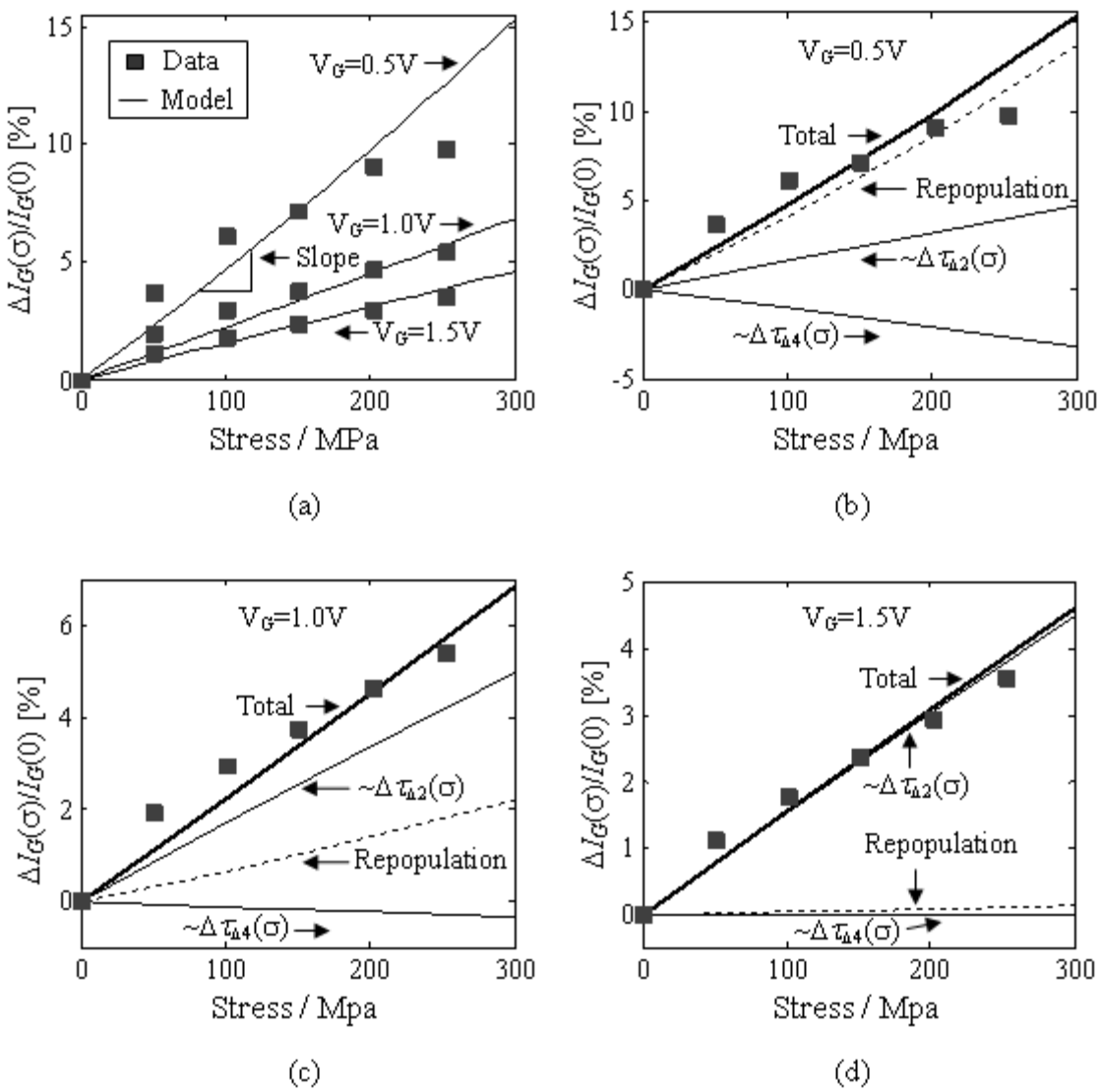

Figure 4-4. (a) Relative direct tunnel current change [$\Delta I_G(\sigma)/I_G(0)$] versus applied compressive stress at different gate voltages. Data (squares) were measured on industrial MOSFETs. The solid lines are our model. (b)-(d) Breakout of the various contribution to $\Delta I_G(\sigma)/I_G(0)$ at different gate voltages: [electron repopulation from Δ_2 to Δ_4 (dominates at low V_G), change in lifetime of Δ_2 or Δ_4 electrons due to change in barrier height].

For low gate voltage, electrons populate both Δ_2 and Δ_4 subbands, so in addition to the stress-induced change in barrier height, stress also increases the population of electrons in Δ_4 which further increases the tunneling current (due to the shorter lifetime in Δ_4 than Δ_2). Capturing the change in tunneling current with stress (or slopes of curves in Fig. 4-4) for the full

range of gate voltage, Fig. 4-6 shows the change in $d[\Delta I_G(\sigma)/I_G(0)]/d\sigma$ versus applied gate voltages.

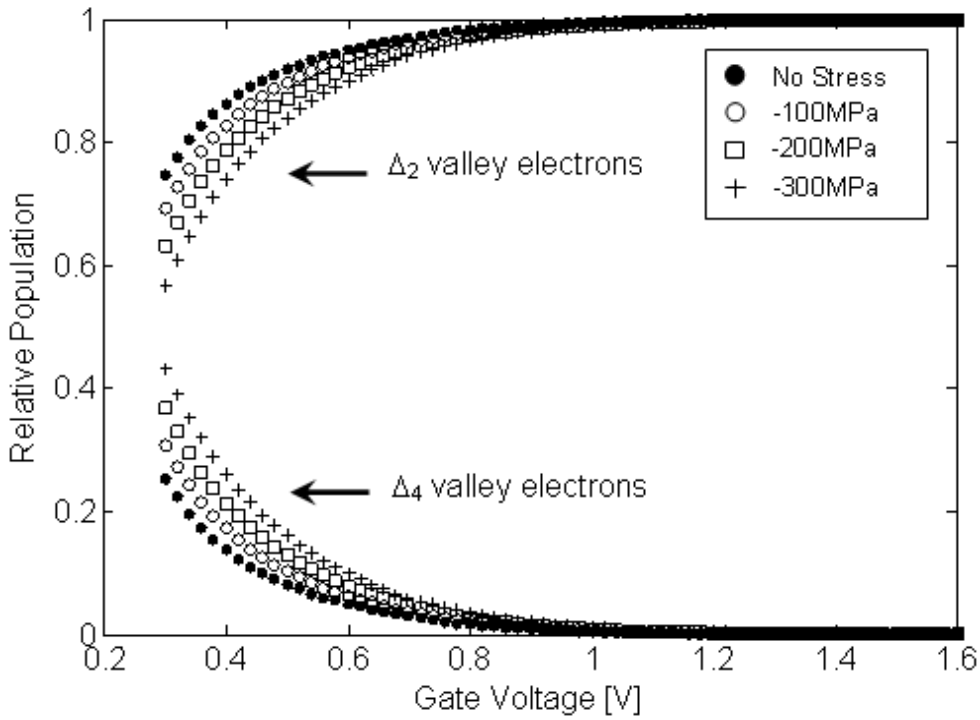

Figure 4-5. Stress-induced repopulation between Δ_2 and Δ_4 ground state electrons. Negative signs in stress mean compression, and the electron population in Δ_2 and Δ_4 subbands decreases and increases, respectively, with increasing compressive stress.

The slope was extracted from the raw data of $I_G(\sigma)$ with the method of least squares. In Fig 4-6, two deformation potential constants (Ξ_d and Ξ_u) are used to match the measured data. The model fits well with the data over a gate bias range of 0.4V to 1.6V, which encompasses the entire direct current region [48]. The best fit [$\Delta E_{\Delta_2}(\sigma) \cong -1.705\times10^{-11}\sigma$ [eV] and $\Delta E_{\Delta_4}(\sigma) \cong 2.995\times10^{-11}\sigma$ [eV] with σ in units of Pa] results in $\Xi_d \cong 1.0 \pm 0.1$ eV and $\Xi_u \cong 9.6 \pm 1.0$ eV. The obtained values of deformation potential constants are very close to theoretical values for bulk Si by Fischetti and Laux (Ξ_d = 1.1 eV, and Ξ_u= 10.5 eV) [12].

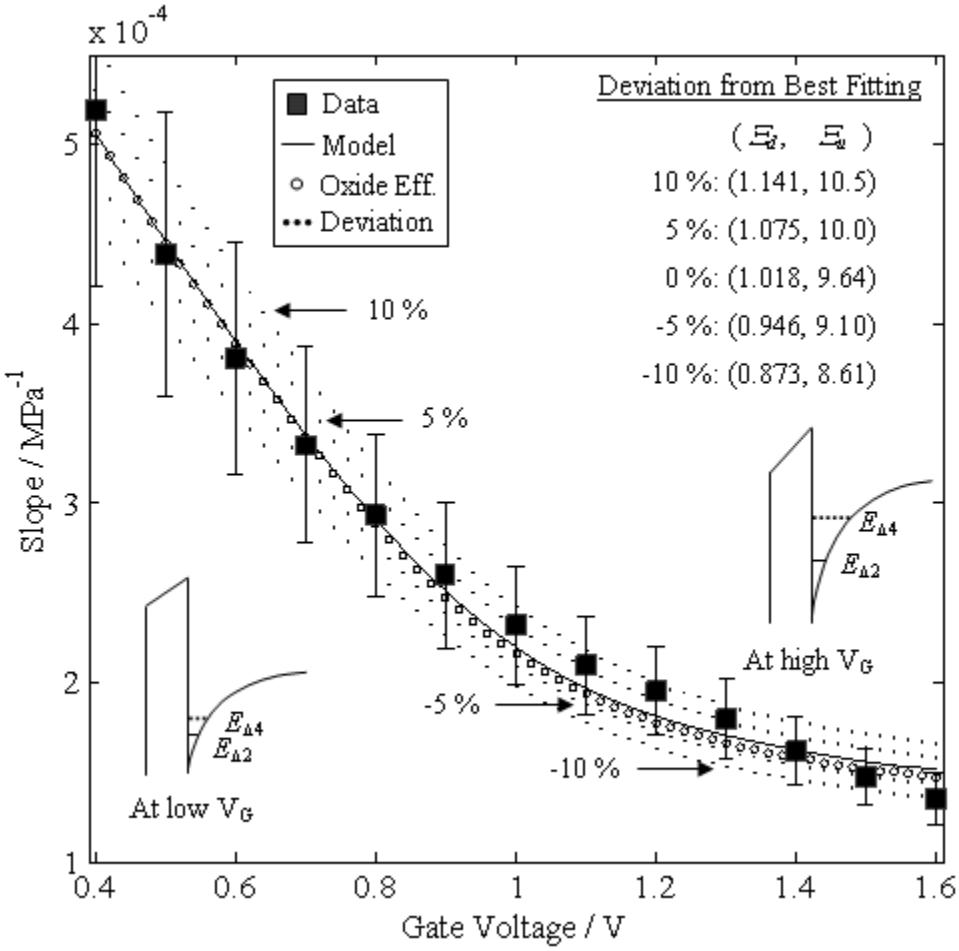

Figure 4-6. Change in slopes ($d[\Delta I_G(\sigma)/I_G(0)]/d\sigma$) versus gate voltage with 95% confidence error bars. Best fit for the entire data set occurs for Ξ_d and Ξ_u of 1.0 eV and 9.6 eV. Deviations from the best fitting values are shown by changing the deformation potentials by ~10%. The insets represent schematic band diagrams at low and high gate biases. Higher slopes at low V_G are due to a larger stress-induced repopulation between Δ_2 and Δ_4 subbands since their energy levels are closer to each other.

The sensitivity to different values of deformation potentials is also shown in Fig. 4-6. The low gate bias slopes are set by the stress-induced band splitting energy, $\Delta E_{\Delta_4}(\sigma)$. The entire curve is adjusted up or down by the magnitude of the SiO_2/Si barrier height [$\Delta E_{\Delta_2}(\sigma)$] since the change in $\Delta E_{\Delta_2}(\sigma)$ results in a parallel shift without any change in the already determined low gate bias slopes. To illustrate the goodness of the model fit, ±10% deviations in both $\Delta E_{\Delta_2}(\sigma)$ and $\Delta E_{\Delta_4}(\sigma)$ are plotted, in which Ξ_d ranges from 0.873 to 1.141 eV, and Ξ_u ranges from 8.61 to

10.5 eV. These fits are shown as the dashed lines in Fig. 4-6 and significant deviation is observed for 5% differences in the deformation potential constants. Stress effects on the oxide thickness are less than 0.05% at $\sigma = -300$ MPa assuming SiO_2 contracts the same amount as Si along the stress direction, and has negligible effects on the model prediction and least-squares fit of deformation potential constants.

Summary

The gate tunneling current has been shown to increase or decrease depending on the stress type, and exhibit an opposite trend for n- and p-MOSFETs. This tunneling current change is explained well by the strain-induced energy level shift and repopulation. The gate bias dependence on $\Delta I_G(\sigma)/I_G(0)$ as a function of mechanical stress for n-MOSFETS has been used to extract the conduction band deformation potential constants. The hydrostatic deformation potential constant, which is traditionally hard to measure, is extracted from the tunneling current and shows excellent agreement with recent numerical calculations [12, 29, 30]. These values of deformation potential constants suggest the strain- induced conduction band shift is approximately $\Delta E_C(\sigma) = -1.71\times10^{-11}\sigma$ eV for uniaxial [110] strain and $\Delta E_C(\sigma) = -3.65\times10^{-11}\sigma$ [or, $\Delta E_C(x) = -0.23x$ in terms of Ge content x] eV for in-plane biaxial strain. The measured conduction band shift in real MOSFET samples is smaller than that typically assumed for biaxial strain, $\Delta E_C(\sigma) = -9.04\times10^{-11}\sigma$ [or, $\Delta E_C(x) = -0.57x$] eV [41, 49]. However, this smaller value of conduction band shift is consistent with both the theoretical calculations and magnitude of the strain-induced MOSFET threshold voltage shift as shown in Fig. 3-9.

CHAPTER 5
STRAIN EFFECT ON LOW-FREQUENCY *1/F* NOISE CHARACTERISTICS

Introduction

Low-frequency *1/f* (or flicker) noise in strained-silicon MOSFETs is certainly an important and interesting research subject since it is often a limiting factor in the device design. It is known that *1/f* noise is up-converted to produce phase noises or degrade SNR (Signal to Noise Ratio) in RF and mixed-mode circuits. In the application of strained MOSFETs to high-performance and high-speed CMOS or RF circuits, this low-frequency noise specifically deserves attention and research.

The *1/f* noise in MOSFETs is believed to occur due to carrier trapping and detrapping at the oxide-Si interface and several models for this surface effect have been proposed [50-53]. Ralls and etal. supported these models by ascribing their random telegraph signal observation in the channel conductance to a phenomenon of the electron capture and emission by the interface trap states [54]. In addition, Welland and Koch even obtained precise trap profile images on the silicon surface of the MOS structures through the scanning tunneling microscopy [55]. To the contrary, bulk mobility fluctuations have been also proposed by Hooge [56, 57] as a main source of *1/f* noise generation in MOSFETs. He concretely pointed out an inversely proportional relationship between the magnitude in *1/f* noise spectrum and total number of charge carriers based on his huge data. These two different viewpoints of a *1/f* noise generation mechanism caused a long-term debate over "bulk mobility fluctuations versus carrier number fluctuations by a surface effect."[58] Currently, a combined model (the number and its correlated mobility fluctuations) is generally accepted as a main source of *1/f* noise generation in MOSFETs [59-65]. Fig. 5-1 shows a *1/f* noise generation mechanism at the oxide-silicon interface. During the current flow, channel charge carriers interact with interface traps (empty or filled) in the gate

oxide. As a result, the charge carriers can be captured, or emitted, or altered by the interface traps, which causes both carrier number and correlated mobility fluctuations.

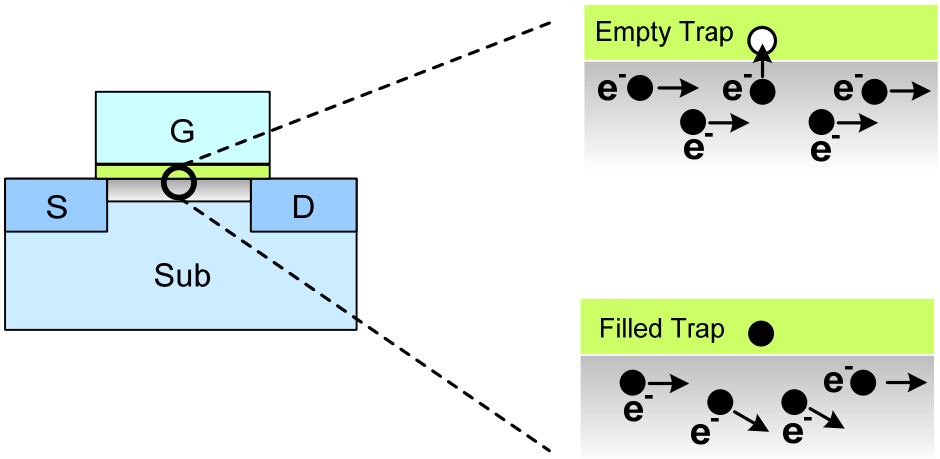

Figure 5-1. Illustration of *1/f* noise generation at the SiO_2/Si interface, adapted from [64].

Conventional Charge Trapping Model

In MOSFETs, the most common *1/f* noise model is a charge trapping model in which the carrier number and its correlated mobility fluctuations are described by random telegraph signals (RTSs) in time domain. It is known that each trapping and the subsequent detrapping produce a RTS, and the observed *1/f* power spectrum is a result of the superposition of each RTS. Actually in the submicron-size MOSFETs (channel area A<1μm^2), only a single trap can be activated near the quasi-Fermi level over the entire channel. The trapping and detrapping of a channel charge carrier by this trap result in discrete channel current resembling RTSs. Fig. 5-2 shows a typical time-domain waveform of the drain current, in which the average capture ($\overline{\tau}_c$) and emission time ($\overline{\tau}_e$) and the average drain current RTS amplitude ($\overline{i}_d$) are specified.

Each single RTS contributes to the resultant *1/f* noise power spectrum of drain current in larger channel-area MOSFETs. The drain current spectrum of a single RTS has a Lorentzian shape,

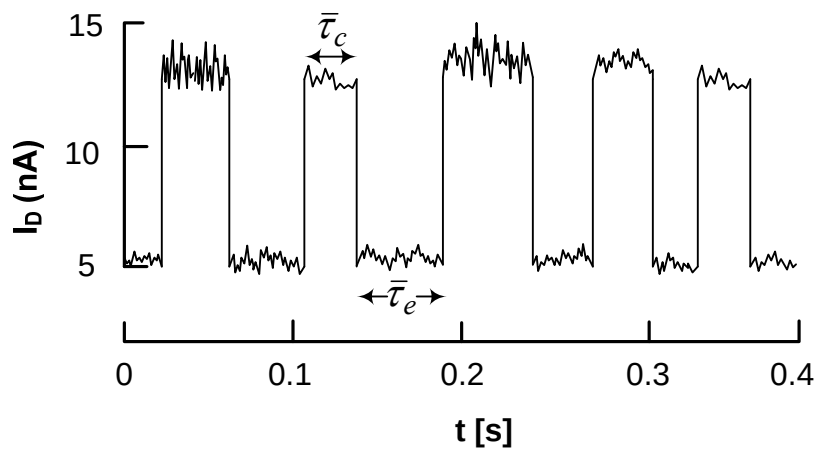

Figure 5-2. Discrete modulation of the channel charge current due to a single trap.

$$S_{\bar{i}_d}(\omega) \propto \bar{i}_d^{\,2} \cdot \frac{\tau(z)}{1+\omega^2\tau^2(z)}, \tag{5-1}$$

where $\tau(z) = \left[1/\bar{\tau}_c(z) + 1/\bar{\tau}_e(z)\right]^{-1}$ is the effective time constant of a trap located at z from the oxide-channel interface. Based on the conventional number fluctuation model, we can obtain an expression for the drain current noise power spectral density (PSD) due to total RTSs. According to the number fluctuation theory, the PSD of the mean square fluctuation in the number of trapped carriers in the volume element ΔV and energy E_t and $E_t + \Delta E_t$ is given by

$$S_{\Delta N_t}(\omega) = 4n_t(E_t, z) \cdot f_t(1-f_t) \cdot \Delta E_t \cdot \Delta V \cdot \frac{\tau(E,z)}{1+\omega^2\tau^2(E,z)}. \tag{5-2}$$

Since the fluctuation in the trapped carriers N_t is equal to the fluctuation in the channel charge carriers N in strong inversion, or $S_{N_t}(\omega) = S_N(\omega)$, we can write down the total drain current noise PSD (S_{ID}) using the general relation $S_{I_D}(\omega)/I_D^2 = S_N(\omega)/N^2$:

$$\begin{aligned} S_{I_D}(\omega) &= \left(\frac{I_D}{N}\right)^2 \cdot \int_{-\infty}^{\infty} dE_t \int_0^L dx \int_0^W dy \int_0^{t_{ox}} 4n_t(E_t,z) \cdot f_t(1-f_t) \cdot \frac{\tau(E,z)}{1+\omega^2\tau^2(E,z)} \cdot dz \\ &\cong \left(\frac{I_D}{N}\right)^2 \cdot L \cdot W \cdot \underbrace{\int_{-\infty}^{\infty} 4n_t(E_t,z) \cdot f_t(1-f_t) \cdot dE_t}_{\text{(A)}} \underbrace{\int_0^{t_{ox}} \frac{\tau(E,z)}{1+\omega^2\tau^2(E,z)} \cdot dz}_{\text{(B)}} \end{aligned} \tag{5-3}$$

where

x-axis along the channel length, y-axis along the channel width, z-axis into the oxide from the interface

$S_N(\omega) = Noise\ PSD\ of\ the\ mean\ square\ fluctuation\ in\ the\ number\ of\ occupied\ traps$
$I_D = Average\ channel\ current\ under\ total\ RTS's$
$N = Total\ channel\ charge\ carrier\ number$
$n_t = Trap\ density\ with\ a\ unit\ of\ [cm^{-3} \cdot eV^{-1}]$
$L = Channel\ length$
$W = Channel\ width$
$Trap\ occupation\ function\ with\ trap\ energy\ E_t\ and\ quasi\ Fermi\ energy\ level\ E_{fn}$

$$f_t = \left[1 + \exp\left(\frac{E_t - E_{fn}}{kT}\right)\right]^{-1}$$

In Eq. (5-3), it is assumed that the oxide trap distribution is negligibly affected along the channel direction for a low drain bias (e.g., V_D=0.1V for our measurements). The integrals (A) and (B) are commonly dealt with in most literatures under two assumptions: ① Uniform spatial distribution of oxide traps, $n_t(E_t, z) = n_t(E_t)$ ② Trapping time constant,

$$\tau(E,z) = \tau_0(E)\exp(\gamma z)\ \ with\ \gamma = \frac{4\pi}{h}\sqrt{2m_{ox}^{*}\Phi_B}\,.$$

From the assumption ①, the integral (A) in Eq. (5-3) is calculated as,

$$(\mathrm{A}) \cong 4n_t(E_{fn}) \cdot \int_{-\infty}^{\infty} f_t(1-f_t) \cdot dE_t \ \text{ assuming } n_t \text{ is not changed much within a few } kT \text{ around } E_{fn}$$

$$= 4n_t(E_{fn}) \cdot \int_{-\infty}^{\infty} \frac{\exp\left(\frac{E_t - E_{fn}}{kT}\right)}{\left[1 + \exp\left(\frac{E_t - E_{fn}}{kT}\right)\right]^2} \cdot dE_t = 4n_t(E_{fn}) \cdot \int_{-\infty}^{\infty} \frac{kT \cdot d\left[1 + \exp\left(\frac{E_t - E_{fn}}{kT}\right)\right]}{\left[1 + \exp\left(\frac{E_t - E_{fn}}{kT}\right)\right]^2} \cdot dE_t$$

$$= 4n_t(E_{fn}) \cdot \left[\frac{-kT}{X}\right]_1^{\infty} = 4kT \cdot n_t(E_{fn})\ \ with\ \ X \equiv 1 + \exp\left(\frac{E_t - E_{fn}}{kT}\right). \qquad (5\text{-}4)$$

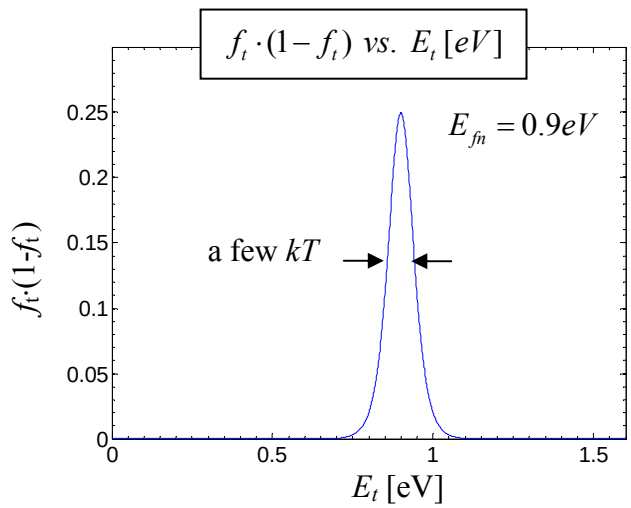

Figure 5-3. Contribution to noise PSD by oxide traps only within a few kT around E_{fn}

As shown in Fig. 5-3, since the product of trap occupancy functions $f_t(1-f_t)$ gives its sharp peak around E_{fn} in the trap energy distribution, oxide traps only within a few kT around E_{fn} mainly contribute to *1/f* noise power spectrum. The assumption ② has been made based on the WKB theory for the gate tunneling of channel carriers. $\tau_0(E)$ is the time constant at the interface and γ is the attenuation coefficient of the carrier wave function in the oxide. Also, m_{ox}^* is the effective mass of the carrier in the oxide and Φ_B is the tunneling barrier height seen by the carriers at the interface. From the relation $\tau(E,z) = \tau_0(E) \cdot \exp(\gamma z)$, we obtain $d\tau = \gamma \cdot \tau \cdot dz$.

Then,

$$(\mathrm{B}) = \int_{\tau_0}^{\tau_1} \frac{\tau}{1+\omega^2\tau^2} \cdot \frac{1}{\gamma} \cdot \frac{d\tau}{\tau} \quad with \;\; \tau_0 = \tau(z=0) \;\; and \;\; \tau_1 = \tau(z = t_{ox})$$

$$= \frac{1}{\gamma \cdot \omega} \cdot \int_{\tau_0}^{\tau_1} \frac{d\tau}{1+\omega^2\tau^2}$$

$$= \frac{1}{\gamma \cdot \omega}\left[\tan^{-1}(\omega\tau)\right]_{\tau_0}^{\tau_1} = \frac{1}{\gamma \cdot 2\pi f}\left[\tan^{-1}(\omega\tau_1) - \tan^{-1}(\omega\tau_0)\right]$$

$$\cong \frac{1}{4\gamma \cdot f} \tag{5-5}$$

since $\tan^{-1}(\omega\tau) \cong \frac{\pi}{2}$ *for* $\omega\tau \gg 1$ *and* $\tan^{-1}(\omega\tau) \cong 0$ *for* $\omega\tau \ll 1$.

The lower and upper values in the integral, τ_0 *and* τ_1, can be roughly estimated using the relation $\tau(E,z) = \tau_0(E) \cdot \exp(\gamma z)$, where $\tau_0(E)$ and γ have typical values of ~10^{-10} s and ~10^{8} cm^{-1}, respectively. For a MOSFET with t_{ox}=5nm, $\tau_0 =\sim 10^{-10} s$ *and* $\tau_1 > 10^{11} s$. Thus in the frequency range of $10^{-8} Hz < 2\pi f < 10^{9} Hz$, we can observe *1/f* noise power spectrum unless it is buried by thermal noise at high frequencies. For a thinner oxide device (e.g., t_{ox}=1.3nm for our samples), the low frequency region of the *1/f* noise spectrum is severely limited by the time constant τ_1 (response of the slow surface states). Plugging (5-4) and (5-5) into (5-3) leads to

$$S_{I_D}(f) = \frac{kT \cdot LW \cdot n_t(E_{fn})}{\gamma \cdot N^2} \cdot \frac{I_D^2}{f}. \tag{5-6}$$

If we check the unit of the right-hand side, γ has a unit of $[cm^{-1}]$ and n_t a unit of $[cm^{-3} \cdot eV^{-1}]$, which gives a unit of $[A^2 / Hz]$ totally. It should be noted that the attenuation coefficient γ is obtained for the rectangular potential barrier (approximation of a trapezoidal potential barrier) at the oxide-Si channel interface. In the expression of a trapping time constant, $\tau(E,z) = \tau_0(E)\exp(\gamma z)$, the quantity γz is given for a trapezoidal barrier as follows [72],

$$\gamma z = \frac{8\pi}{3h} \cdot \sqrt{2m_{ox}^*} \cdot \frac{(\Phi_B - q \cdot |\varepsilon_{ox}| \cdot z)^{3/2} - \Phi_B^{\ 3/2}}{q \cdot |\varepsilon_{ox}|}, \tag{5-7}$$

where ε_{ox} is the electric field in the oxide. Expanding the nominator in Eq. (5-7) in terms of z, we obtain

$$(\Phi_B - q\cdot|\varepsilon_{ox}|\cdot z)^{3/2} - \Phi_B^{\ 3/2} = \frac{3q\cdot|\varepsilon_{ox}|\cdot\Phi_B^{\ 1/2}\cdot z}{2} - \frac{3q^2\cdot|\varepsilon_{ox}|^2\cdot z^2}{8\Phi_B^{\ 1/2}} + \ \ldots\ldots\ldots$$
$$\cong \frac{3q\cdot|\varepsilon_{ox}|\cdot\Phi_B^{\ 1/2} z}{2} \quad for \ \frac{q\cdot|\varepsilon_{ox}|\cdot z}{\Phi_B} \ll 1\,. \tag{5-8}$$

For a negligible oxide band bending as in operations of old devices (t_{ox}>5nm), we can approximate γz as a rectangular barrier case with little errors, that is

$$\gamma z = \left[\frac{4\pi}{h}\sqrt{2m_{ox}^{*}\Phi_B}\right]\cdot z \tag{5-9}$$

However, this rectangular barrier approximation leads to a considerable error for modern thin-oxide MOSFETs (t_{ox}<1.5nm) especially when a high gate bias is applied. In order to reduce this error, it is possible to include the 2nd term in Eq. (5-8), that is

$$\gamma' z = \frac{4\pi}{h}\sqrt{2m_{ox}^{*}\Phi_B}\cdot\left[1-\frac{q\cdot|\varepsilon_{ox}|\cdot t_{ox}}{4\Phi_B}\right]\cdot z, \tag{5-10}$$

where we replaced z^2 with $t_{ox}\cdot z$ to keep a form of $\gamma' z$. The time constant then changes to

$$\tau(E,z) = \tau_0(E)\cdot\exp(\gamma' z) \ \ with\ \gamma' = \gamma\cdot\left[1-\frac{q\cdot|\varepsilon_{ox}|\cdot t_{ox}}{4\Phi_B}\right] \tag{5-11}$$

Also, it should be desirable to use a modified WKB method for a thin oxide MOSFET. In gate tunneling models based on a modified WKB method, a compensation factor (T_R) is introduced to account for the discontinuity at the oxide-Si channel interface in calculating the transmission probability of channel carriers [47,48]. If we use this modified WKB approximation method, the time constant $\tau(E,z)$ is further changed to

$$\tau(E,z) = \frac{\tau_0(E)}{T_R} \cdot \exp(\gamma' z), \tag{5-12}$$

since the time constant is inversely proportional to the transmission probability. Therefore, the new time constant, $\tau(E, z)$, is a function of gate bias. Returning to Eq. (5-6), the drain current noise PSD can be expressed as, when we include the correlated mobility fluctuations [59, 65, 72],

$$S_{I_D}(f) = \frac{kT \cdot LW \cdot n_t(E_{fn})}{\gamma \cdot N^2} \cdot \left(1 + S \cdot \mu \cdot N\right)^2 . \frac{I_D^2}{f}, \tag{5-13}$$

where S is the scattering coefficient and μ is the correlated mobility fluctuation. In general, the scattering coefficient S is a function of both the channel charge density associated with a screening effect and the trap distance from channel charge carriers.

The conventional charge trapping model has been briefly reviewed so far. The exact $1/f$ noise spectrum results from the assumption that the oxide trap distribution is spatially uniform for the calculation convenience in Eq. (5-3). Now, we examine a special case of the trap distribution to obtain a more general form of the $1/f^{\alpha}$ spectrum. In general, a trap distribution is functions of energy and space, and often treated as exponential functions in literature. We choose then a functional form of the trap density as,

$$n_t(E,z) = n_{t0} \cdot \exp(\xi \cdot q\left|V_{ox}\right| \cdot \frac{z}{t_{ox}} + \eta z), \tag{5-14}$$

where ξ and η are trap distribution coefficients over energy and space with units of meV^{-1} and nm^{-1}, respectively, and the two terms in the exponential argument are due to oxide band bending and nonuniform spatial distribution into the oxide depth. Fig. 5-4 shows the coordinate system in which the traps are distributed along the z-axis and the field direction. When a gate voltage is applied, traps are shifted from the original place by an amount of oxide band bending.

The integral part (B) in Eq. (5-3) is written using the trap distribution $n_t(E,z)$ in Eq. (5-14) as,

$$\text{(B)} = \int_0^{t_{ox}} \frac{\tau \cdot \exp(\xi \cdot q\left|V_{ox}\right| \cdot \frac{z}{t_{ox}} + \eta z)}{1+\omega^2\tau^2} \cdot dz \tag{5-15}$$

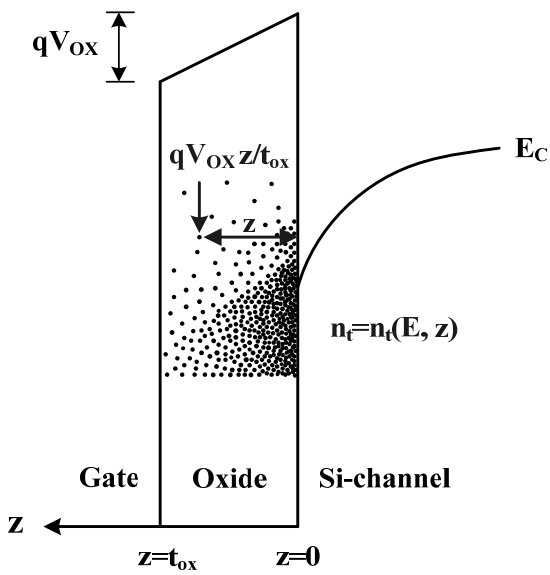

Figure 5-4. Shifts in trap location due to oxide band bending.

Similarly as carried out in Eq. (5-5), we can calculate the integral (B) in Eq. (5-15).

$$\begin{aligned}\text{(B)} &= \frac{1}{\gamma}\int_{\tau_0}^{\tau_1} \frac{\exp\left[(\xi \cdot q\left|V_{ox}\right| / t_{ox} + \eta) \cdot z\right]}{1+\omega^2\tau^2} \cdot d\tau \\ &= \frac{1}{\gamma \cdot (\tau_0)^{(\xi \cdot q|V_{ox}|/t_{ox}+\eta)/\gamma}} \cdot \frac{1}{\omega^{1+(\xi \cdot q|V_{ox}|/t_{ox}+\eta)/\gamma}} \cdot \underbrace{\int_{\tau_0}^{\tau_1} \frac{(\omega\tau)^{(\xi \cdot q|V_{ox}|/t_{ox}+\eta)/\gamma}}{1+\omega^2\tau^2} \cdot d(\omega\tau)}_{\text{C}}\end{aligned} \tag{5-16}$$

The integral (C) in Eq. (5-16) can be easily calculated if we use the following relation,

$$\int_0^{\infty} \frac{x^{p-1}}{1+x} \cdot dx = \Gamma(p) \cdot \Gamma(1-p) = \frac{\pi}{\sin p\pi} \quad where \;\; 0 < p < 1. \tag{5-17}$$

We change the integral (C) into the form of Eq. (5-17).

$$
\begin{aligned}
(\mathrm{C}) &= \frac{1}{2}\int_{\tau_0}^{\tau_1} \frac{(\omega\tau)^{-1+\eta/\gamma}}{1+(\omega\tau)^2}\cdot d(\omega\tau)^2 \\
&\cong \frac{1}{2}\int_{0}^{\infty} \frac{[(\omega\tau)^2]^{\frac{1+\eta/\gamma}{2}-1}}{1+(\omega\tau)^2}\cdot d(\omega\tau)^2 \quad \text{for } (\omega\tau_0)^2 \ll 1 \text{ and } (\omega\tau_1)^2 \gg 1 \\
&= \frac{\pi}{2\sin\left(\frac{1+\eta/\gamma}{2}\cdot\pi\right)}
\end{aligned}
\tag{5-18}
$$

Using Eq. (5-3), (5-13), (5-16), and (5-18) we obtain for the drain current noise PSD,

$$
S_{I_D}(f) = \frac{kT\cdot L\cdot W\cdot n_t(E_{fn})}{\gamma\cdot N^2}\cdot\left(1+S\cdot\mu\cdot N\right)^2\cdot\frac{2\pi(\tau_0)^{1-\alpha}}{\sin(\alpha\pi/2)}\cdot\frac{I_D^2}{(2\pi f)^{\alpha}} \propto \frac{1}{f^{\alpha}}, \tag{5-19}
$$

where $\alpha = 1+\dfrac{\xi\cdot q\left|V_{ox}\right|/t_{ox}+\eta}{\gamma}$.

The exponent α in $1/f^{\alpha}$ noise spectrum is expressed with two terms; one is due to energy distribution of traps, which is dependent of gate bias, and the other is due to spatial distribution of traps, which is independent of gate bias. Typical values of ξ and η are ~0.02/mev and ~3/nm.

Wafer Bending Experiment on *1/f* Noise

Measurements of *dc* Currents and Drain Current Noise PSD

A schematic block diagram for the measurements of *1/f* noise and *dc* currents is shown in Fig. 5-5. The *dc* currents (drain and gate currents) and drain current noise PSD were measured for each applied mechanical stress at the same bias condition. A Keithley 4200 *dc* characterization system was used to measure *dc* currents at the drain and gate terminals, and a Stanford Research (SR) 785 spectrum analyzer was used to measure the drain current noise PSD, respectively. One battery powered SR 570 current amplifier was used to amplify the drain current noise (S_{ID}) under an applied drain bias (V_D). A second battery powered LNA was employed to apply a variable gate bias (V_G). In order to minimize external electromagnetic

interference, all equipment and cables were placed inside a shielded probe station and battery powered except for the spectrum analyzer and semiconductor parameter analyzer (Keithley 4200). The noise PSD data were obtained using a SR 785 spectrum analyzer up to 12.8kHz by measuring five frequency spans (100Hz, 400Hz, 1.6kHz, 6.4kHz, and 12.8kHz) using a Hanning window. Each frequency span contained 800 data points (800 FFT lines), and each data record was typically averaged from 100 to 1000 times by the SR 785 spectrum analyzer. Extraction of the current noise PSD of an n-channel MOSFET device under test (DUT) is illustrated in Fig. 5-6. In order to measure the current noise PSD of the setup, the input of the amplifier (SR 570) is open circuited. The plot of the current noise PSDs of the setup and a DUT with and without the subtraction of the setup noise PSD is shown in the figure. The noise PSD of the DUT is extracted by subtracting the noise PSD contribution of the setup from the measured total current PSD. All the measurements on our MOSFET samples were made using the same sensitivity of 20μA/V for the SR 570.

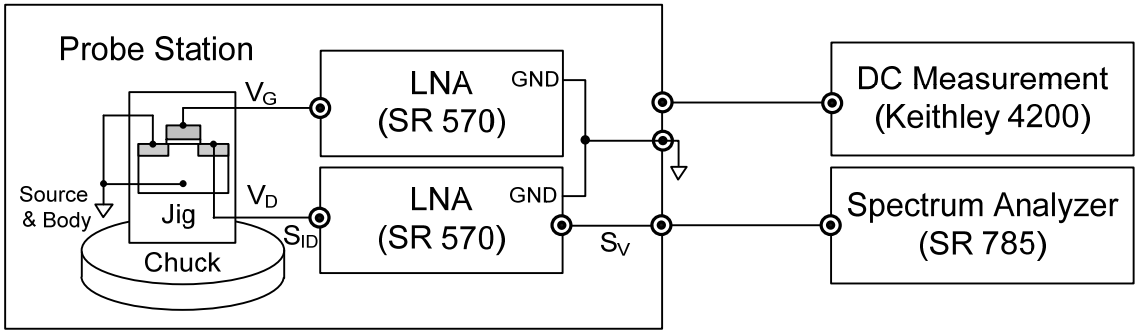

Figure 5-5. Schematic block diagram for *1/f* noise and *dc* current measurements.*1/f* noise and *dc* currents (both drain and gate currents) were measured for each applied mechanical stress using a spectrum analyzer, two LNAs, and a Keithley 4200 system. The SR 570 current amplifier has a current input (S_{ID}) and a *dc* voltage output.

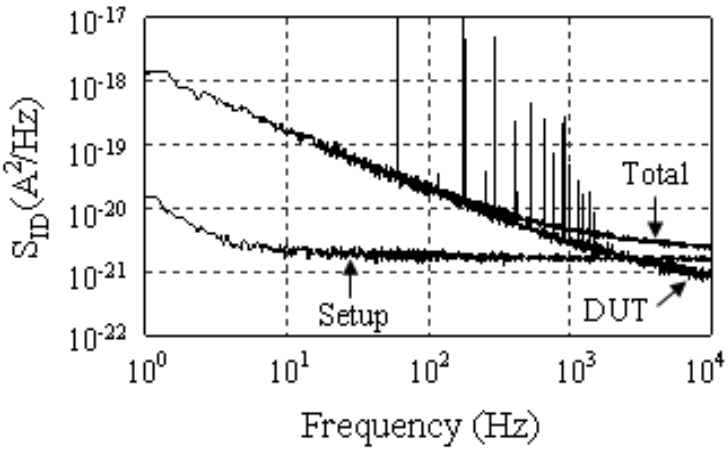

Figure 5-6. Noise power spectrums for an n-channel MOSFET with and without the setup noise. Measurements were made on a sample with a channel length L=2μm, a width W=50μm, and a threshold voltage V_t=0.36V at *dc* biases V_G=0.6V and V_D=0.1V. The DUT noise power spectrum is obtained by subtracting the setup noise from the measured total noise.

Measurement Results

n-MOSFET under tensile stress

The drain current *1/f* noise was measured on an n-channel MOSFET with a channel length L=2μm, a width W=50μm, and a threshold voltage V_{th}=0.36V under tensile stress. The MOSFET was biased in the linear region at V_G=0.6V and V_D=0.1V, and six uniaxial tensile stresses were applied up to 225MPa. The measured *dc* currents and *1/f* noise power spectrums are shown in Fig. 5-7. The drain (I_D) and gate currents (I_G) are observed to consistently increase and decrease, respectively, with increasing tensile stress as expected from previous studied [46, 73]. Under a stress of 200MPa, the drain current increases by about 7%, and the gate current decreases by about 2.4%. The drain current noise PSD is observed to increase for tensile stress as shown in Fig. 5-7 (d), although the trend is not clear at some frequencies without further averaging as discussed in section 5.3.2.4.

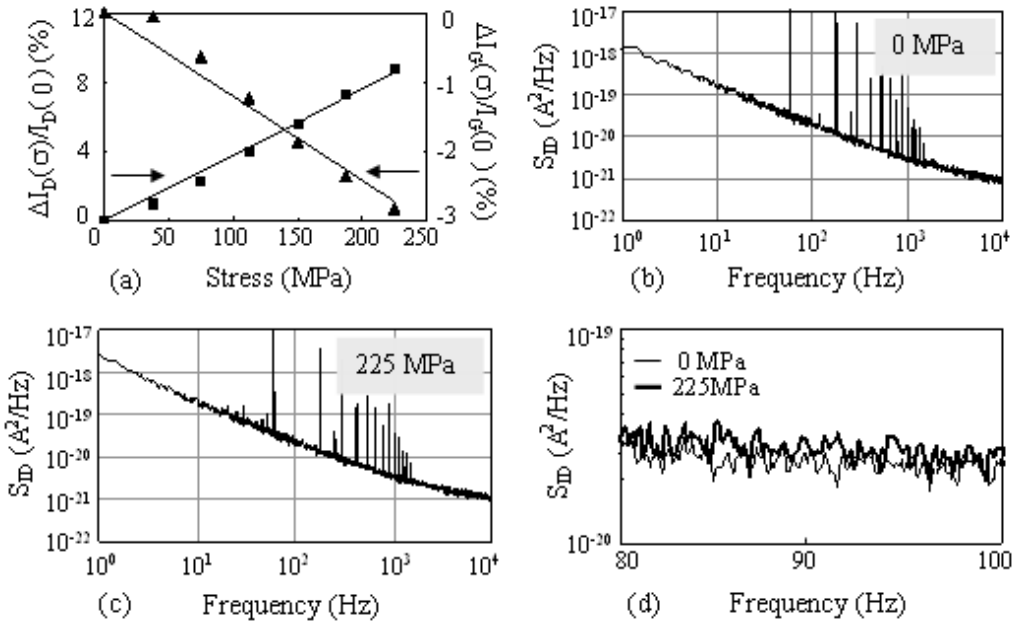

Figure 5-7. Measurements of an n-MOSFET under tensile stress. Measurements were made on a sample with a channel length L=2μm, a width W=50μm, and a threshold voltage V_t=0.36V at *dc* biases V_G=0.6V and V_D=0.1V. (a) Relative changes in drain and gate tunneling currents. (b)-(c) Observed noise power spectrums for different stresses. (d) Comparison of drain current noise PSD for different stresses.

n-MOSFET under compressive stress

The measured n-channel sample has a channel length L=2μm, a width W=50μm, and a threshold voltage V_{th}=0.28V. The sample was biased in the linear region at V_G=0.6V and V_D=0.07V, and six uniaxial compressive stresses were applied up to 189MPa. The measured *dc* currents and *1/f* noise power spectrums are shown in Fig. 5-8. As opposed to the tensile stress case, with increasing compressive stress, the drain current (I_D) decreases and the gate current (I_G) increases as also shown previously [13, 74]. The drain current decreases by about 6%, and the gate tunneling current increases by about 2.5 % at a compressive stress level of 200MPa. The drain current noise PSD is shown to decrease in Fig. 5-8 (d).

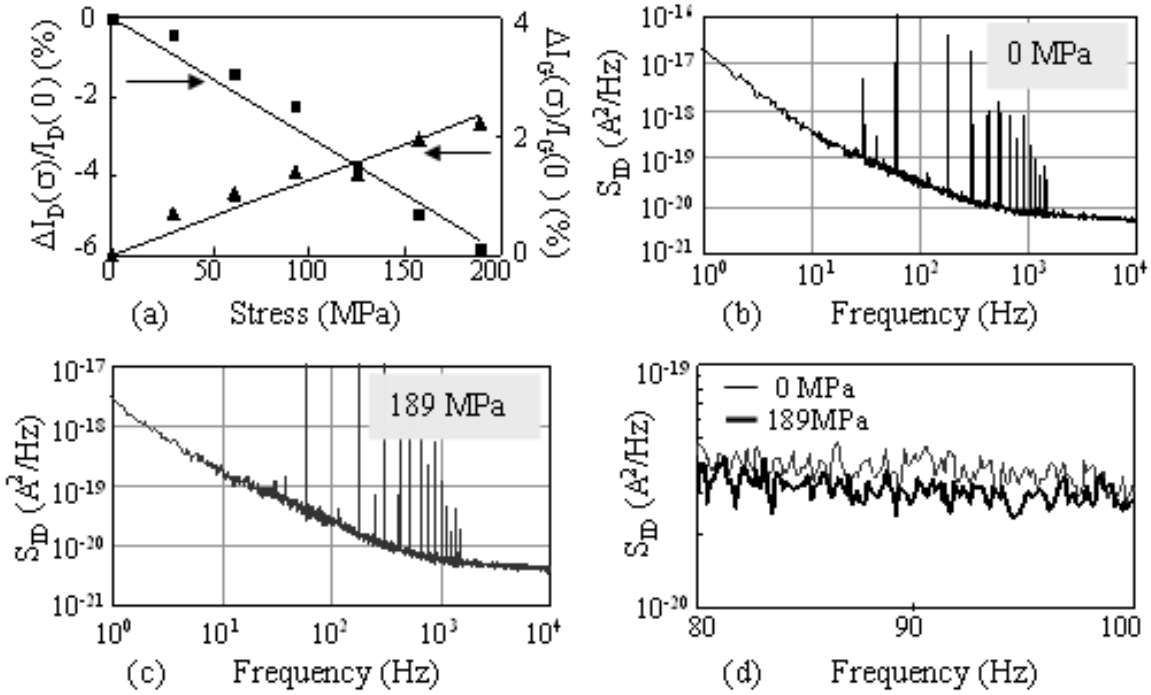

Figure 5-8. Measurements of an n-MOSFET under compressive stress. Measurements were made on a sample with a channel length L=2μm, a width W=50μm, and a threshold voltage V_t=0.28V at *dc* biases V_G=0.6V and V_D=0.07V. (a) Relative changes in drain and gate tunneling currents. (b)-(c) Observed noise power spectrums for different stresses. (d) Comparison of drain current noise PSD for different stresses.

p-MOSFET under compressive stress

The measured *dc* currents and *1/f* noise power spectrums are also plotted for a p-MOSFET in Fig. 5-9. Measurements were made under compressive stress for two different gate biases, V_G= -0.6V and -0.8V, at the same drain bias, V_D=-0.1V. Compressive stresses were applied up to 189MPa. For these two measurements, the drain (I_D) and gate (I_G) currents are commonly observed to increase and decrease, respectively, with increasing compressive stress [45, 74]. The change is about 10% for drain currents and -2% for gate currents at a compressive stress level of 200MPa. The noise PSDs increase for both of the two measurements as shown in Fig. 5-9 (d).

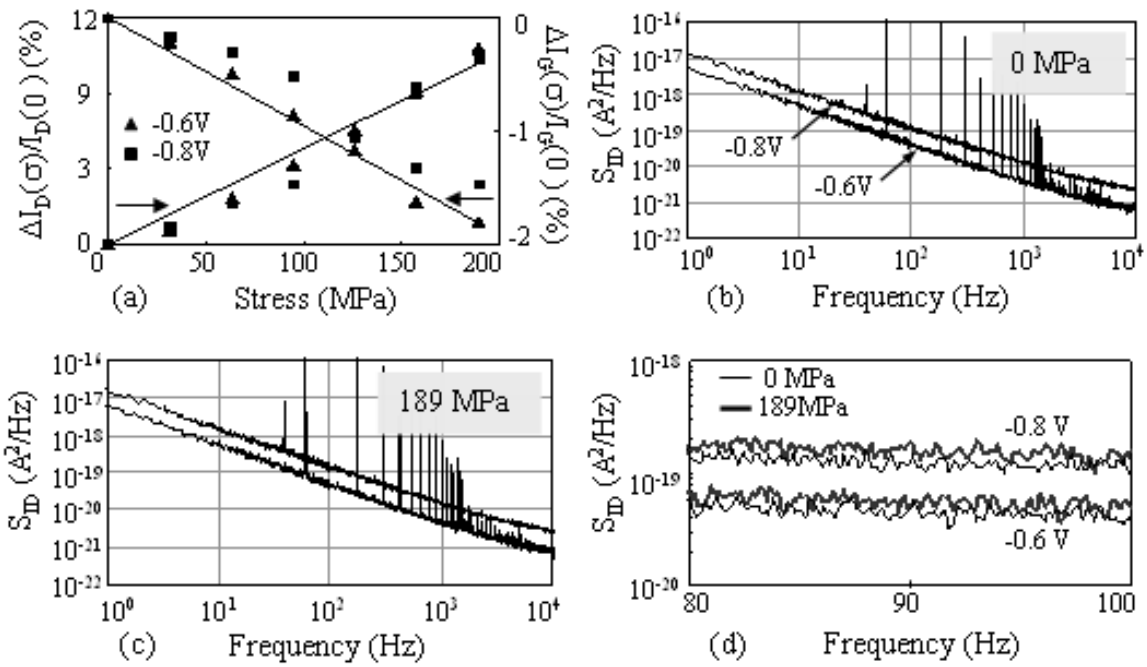

Figure 5-9. Measurements of a p-MOSFET under compressive stress. Measurements were made on a sample with a channel length L=1μm, a width W=50μm, and a threshold voltage V_t=-0.36V at *dc* biases V_D=-0.1V and V_G=-0.6V, and V_D=-0.1V and V_G=-0.8V. (a) Relative changes in drain and gate tunneling currents. (b)-(c) Observed noise power spectrums for different stresses. (d) Comparison of drain current noise PSD for different stresses.

Data analysis

In this subsection, we first examine the averaging of the raw drain current noise data obtained by the spectrum analyzer. Unlike drain or gate tunneling current measurements, the noise PSD values are measured with large uncertainties. More accurate PSD data can be obtained through a higher number of averages, which are generally limited by the measurement time. As shown in Fig. 5-7 (d) through 5-9 (d), the magnitude of the fluctuations is almost comparable to the maximum noise PSD change for our stress level, although the noise data have been already averaged from 100 to 1000 times by the spectrum analyzer. More averaging is then required to differentiate even a few percent change in the noise PSD which may be accomplished using linear regression analysis either globally or locally by noting the *1/f* frequency dependence of the

noise spectra. Since the drain current *1/f* noise PSD generally follows the following frequency dependence,

$$S_{ID}(f) = \frac{S_{ID}(1Hz)}{f^{\alpha}}, \tag{5-20}$$

we can extract the noise magnitude and exponent by a least squares fit (LSF) of the noise spectrum on a log-log plot. Over the frequency range that Eq. (5-20) holds, the PSD can be expressed as a linear function of frequency on a log-log plot,

$$\log[S_{ID}(f)] = \log[S_{ID}(1Hz)] - \alpha \cdot \log f, \tag{5-21}$$

as illustrated in Fig 5-11 (a). If the PSD data follows a $1/f^{\alpha}$ dependence over a wide frequency range, then a frequency-independent noise exponent, α, and magnitude, $S_{ID}(1Hz)$, may be extracted via LSF. This is the case for the measured p-channel MOSFET PSD data shown in Fig. 5-11 (b)-(c). However, in some devices, the low frequency PSD data exhibits some frequency structure associated with a trap-related Lorentzian such as in the measured n-channel MOSFET PSD data seen in Fig. 5-8 (b)-(c). When Eq. (5-20) applies only locally for a smaller range of frequencies, the PSD at each frequency is first averaged using a moving average, and then the best fit slope is computed. Fig. 5-10 illustrates the method used to extract the average values locally from the measured raw data. The moving average is obtained as follows. Consider an average value of noise PSD, $\overline{S_{ID}(f_M)}$, at a specific frequency of f_M. The neighboring data point pairs are chosen such that each pair satisfies the condition $\log f_M - \log f_{L_i} = \log f_{H_i} - \log f_M$, where $\log f_{L_i}$ and $\log f_{H_i}$ are each frequency pair centered about a target frequency, $\log f_M$. N pairs are averaged to estimate an average value of the noise PSD, $\overline{S_{ID}(f_M)}$, at a specific frequency of f_M. On a linear scale, $\overline{S_{ID}(f_M)}$, at f_M is obtained as follows,

$$\overline{S_{ID}(f_M)} = \left[\prod_{i=0}^{N-1} S_{ID}(f_{L_i}) \cdot S_{ID}(f_{H_i}) \right]^{1/2N} \tag{5-22}$$

where $S_{ID}(f_{L_0})$ and $S_{ID}(f_{H_0})$ are defined as $S_{ID}(f_{L_0}) = S_{ID}(f_{H_0}) \equiv S_{ID}(f_M)$, and N is the number of chosen neighboring data pairs.

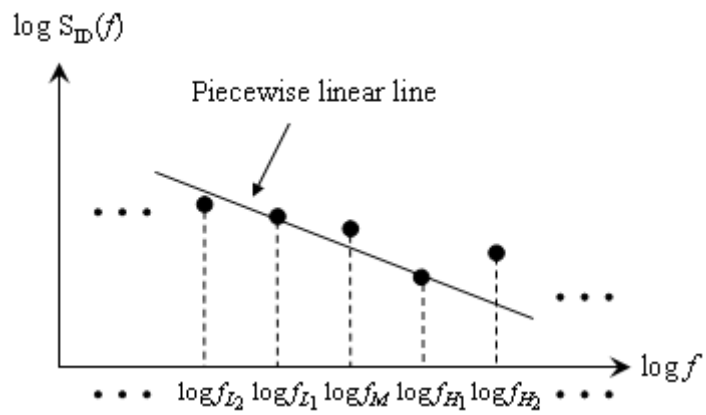

Figure 5-10. Schematic illustration for extracting a local average value of noise PSD at a specific frequency of interest from the measured raw data. Raw noise data fluctuate against a piecewise linear line on a log-log plot. To reduce the deviation in PSD values due to these fluctuations, a local averaging method can be used. The local average value of the PSD, $\overline{\log\left[S_{ID}(f_M)\right]}$, at a frequency of f_M is obtained through averaging of chosen neighboring data pairs of PSD values, $\log\left[S_{ID}(f_{L_i})\right]$ and $\log\left[S_{ID}(f_{H_i})\right]$, which are chosen such that $\log f_M - \log f_{L_i} = \log f_{H_i} - \log f_M$.

The extraction of the noise exponent, α, and magnitude, $S_{ID}(1Hz)$, is illustrated for the measured p-channel MOSFET PSD which follows a $1/f^{\alpha}$ dependence over a wide frequency range as shown in Fig. 5-11 (a). For each applied uniaxial longitudinal compressive stress, α and $S_{ID}(1Hz)$ are extracted via LSF of the PSD over a frequency range of 30Hz to 1 kHz and plotted in Figs. 5-11 (b)-(c) as a function of stress for a gate bias of -0.6V. The normalized change in $S_{ID}(1Hz)$ relative to the unstressed case, $\Delta S_{ID}(1Hz;\sigma)/S_{ID}(1Hz;0)$, is plotted as a function of stress in Fig. 5-11 (d). When the PSD follows a $1/f^{\alpha}$ dependence over a wide frequency range, the global and local LSF results show good agreement as seen in Fig. 5-11 (d) for two gate biases.

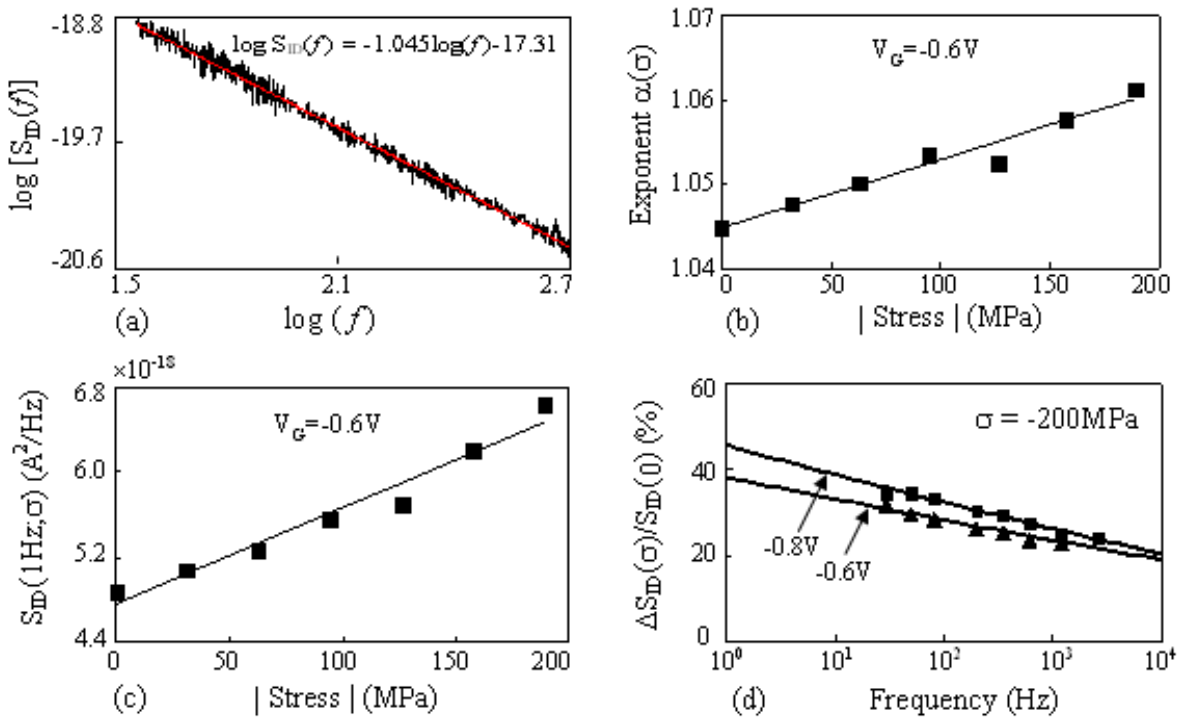

Figure 5-11. Analysis of p-channel MOSFET data under compressive stress. (a) Extraction of the noise magnitude and exponent α on a log-log plot. (b) Extracted exponent α value vs. applied stress (c) Extracted noise magnitude vs. applied stress (d) Relative changes in noise PSD vs. frequency at different gate voltages. The lines are plotted based on the extracted noise magnitude and exponent values, and the symbols are averaged values obtained using 50 pairs of neighboring noise PSD data.

From the measured n-channel MOSFET PSD for different applied mechanical stresses σ, the local averaging technique is used with 50 pairs of data points to extract the average drain current noise PSD, $\overline{S_{ID}(f;\sigma)}$, as a function of stress at specific frequencies. Figs. 5-12 and 5-13 plot the extracted average PSD values for n-channel MOSFETs as a function of applied tensile and compressive stress for specific frequencies and the normalized change in PSD, $\Delta S_{ID}(f;\sigma)/S_{ID}(f;0)$, as a function of frequency for a specific stress. Both the locally averaged PSD and the raw PSD are shown. The PSD values corrupted by external noise sources such as 60Hz and its harmonics were excluded in the average calculations.

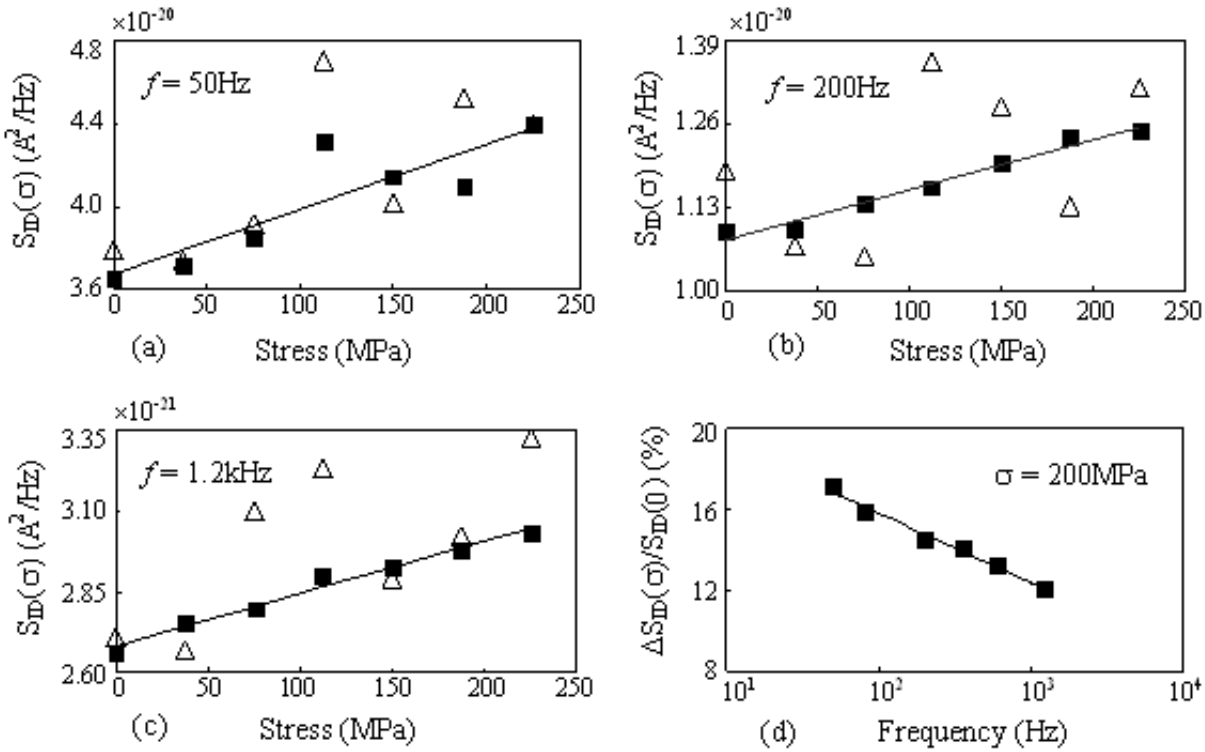

Figure 5-12. Analysis of n-channel MOSFET data under tensile stress(a)-(c) Changes in noise PSD vs. applied stress at different frequencies. The solid squares are extracted average values at each stress level using 50 pairs of neighboring PSD data, and the empty triangles are raw values directly read from the SR 785. The lines are fitted to the extracted average values. (d) Relative change in noise PSD vs. frequency at a stress of 200MPa.

To summarize our measurements, it is observed that: (1) *1/f* noise drain current PSD increases and decreases for n-channel MOSFETs with increasing tensile and compressive stress, respectively, while it increases for p-channel MOSFETs with increasing compressive stress. (2) The relative change in PSDs shows a frequency dependence (i.e., larger changes for lower frequencies) for both n- and p-MOSFETs. (3) With applied mechanical stress, the changes in drain current have a similar trend to the change in the drain current noise PSDs while the changes in gate currents have a trend opposite to that of the change in drain current noise PSDs.

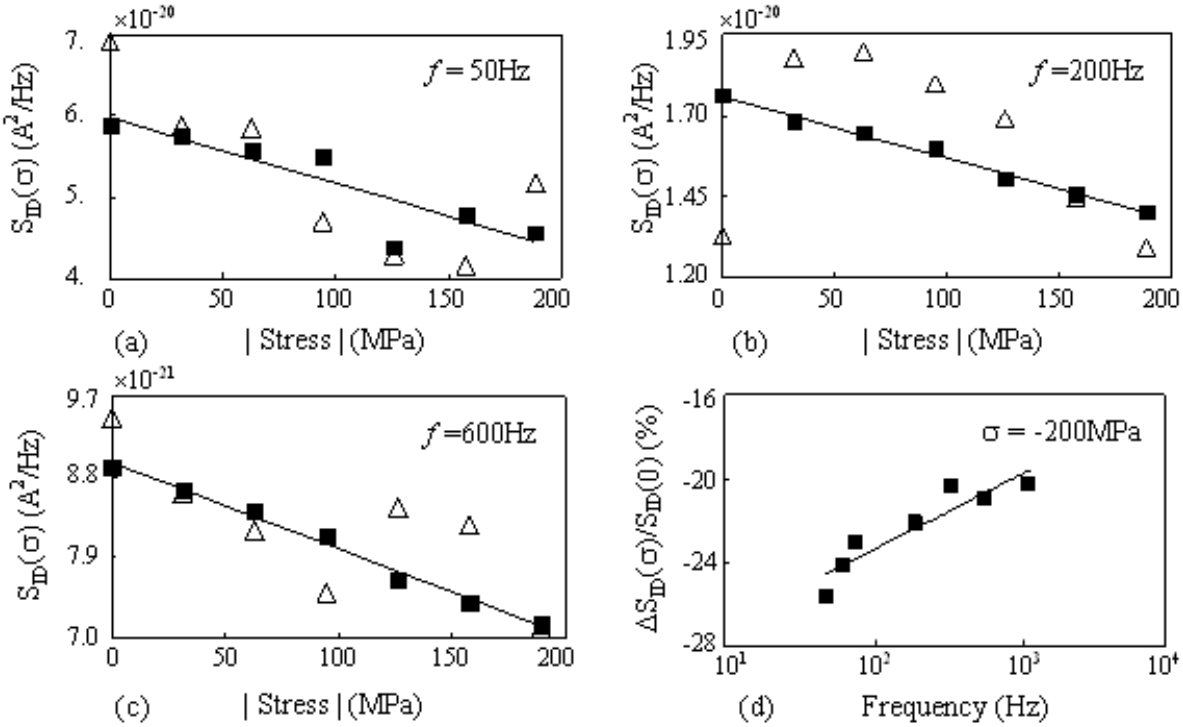

Figure 5-13. Analysis of n-channel MOSFET data under compressive stress. (a)-(c) Changes in noise PSD vs. applied stress at different frequencies. The solid squares are extracted average values at each stress level using 50 pairs of neighboring PSD data, and the empty triangles are raw values directly read from the SR 785. The lines are fitted to the extracted average values. (d) Relative change in noise PSD vs. frequency at a stress of -200MPa.

In the noise measurements, it has been observed that both *1/f* noise magnitude and exponent are functions of applied mechanical stress. Therefore, the strain-induced relative change in *1/f* noise PSD, referenced at zero stress, can also be expressed from Eq. (5-20) as

$$\ln\left(1+\frac{\Delta S_{ID}(f;\sigma)}{S_{ID}(f;0)}\right)=\ln\left(1+\frac{\Delta S_{ID}(1Hz;\sigma)}{S_{ID}(1Hz;0)}\right)-\Delta\alpha(\sigma)\cdot\ln f, \tag{5-23}$$

where $\Delta S_{ID}(f;\sigma)=S_{ID}(f;\sigma)-S_{ID}(f;0)$ and $\Delta\alpha(\sigma)=\alpha(\sigma)-\alpha(0)$. We assume that linear relationships for the parameters, $S_{ID}(f;\sigma)$ and $\alpha(\sigma)$, are valid since the applied stresses are small (< 250MPa). Table 5-1 lists the stress-dependent drain current PSD parameters obtained from our measurements. In this study of strain effects on noise PSD, $\Delta S_{ID}(1Hz;\sigma)$ and $\Delta\alpha(\sigma)$ are the

focus of the noise model since they vary independently with applied stress. The next section develops a theoretical model for the stress dependence of drain current noise PSDs.

Table 5-1. Relative change in noise PSD parameters for an applied stress of 100MPa.

Stress/Device		$\Delta I_D(\sigma)/I_D(0)$	$\Delta I_G(\sigma)/I_G(0)$	$\Delta\alpha(\sigma)$	$\Delta S_{ID}(1Hz;\sigma)/S_{ID}(1Hz;0)$
Tensile n-channel MOSFET		3.78 %	-1.20 %	0.66 %	11.9 %
Compressive n-channel MOSFET		-2.97 %	1.24 %	-0.75 %	-16.2 %
Compressive	-0.6V	5.07 %	-0.957 %	0.82 %	19.2 %
p-channel MOSFET	-0.8V	4.80 %	-0.769 %	1.03 %	22.9 %

*The relative changes in the noise magnitude and exponent are extracted using Eq. (5-23) for n-channel MOSFETs and are extracted using Eq. (5-21) on the log-log plot for p-channel MOSFETs.

Charge Trapping Model under Strain

Mechanism for Change in Noise PSD under Strain

A charge trapping model is considered to explain the strain dependence of *1/f* noise in MOSFETs. The charge trapping model ascribes the origin of *1/f* noise to charge trapping and detrapping of channel charge carriers by oxide traps [59, 65, 72, 75-78]. In ultrathin gate oxide MOSFETs, contrary to the conventional treatment of *1/f* noise, even a relatively low gate bias can cause significant band bending in the Si-channel, thus causing the Fermi level to lie above the conduction band edge or below the valence band edge [47-48]. Under this condition, the contribution to *1/f* noise PSD mostly results from trapping/detrapping of channel carriers at oxide traps existing above the Si conduction band edge or below the Si valence band edge. Thus, trapping at bandgap traps via two-step or multi-phonon processes can be neglected compared with trapping via elastic direct tunneling [65, 72, 75]. Fig. 5-14 (a) shows a schematic band diagram of n-channel MOSFETs under mechanical stress. Applying uniaxial tensile stress shifts the ground energy level (E_0) lower in the inversion layer [13, 46]. As a result, the tunneling probability of channel electrons at E_0 decreases because of the higher potential barrier while the

trapping probability of tunneling electrons by oxide traps increases since their energy level shifts closer to the quasi-Fermi level (E_{FN}) as shown in Fig. 5-14 (b). These two effects oppositely affect the change in noise PSD; the former decreases the noise PSD, but the latter increases it. However, as indicated in Table 5-1, the decreasing effect (the reduction in I_G) is not dominant in determining the overall change in noise PSD. In addition, the oxide trap distribution is another important factor in determining the noise PSD change. Tunneling electrons encounter less or more traps depending on the oxide trap distribution in energy space. Trap distribution is represented over space and energy as dots in Fig 5-14 (a). Strain also affects the correlated mobility fluctuations in the charge trapping model through both alteration of channel carrier mobility and repopulation among inversion subband carriers. In the following subsection, we discuss these strain effects on *1/f* noise PSD in more detail with some numerical examples.

Charge Trapping Model under Strain

In the conventional charge trapping model, the drain current noise PSD, $S_{ID}(f)$, is given by [59, 65, 72, 78]

$$S_{ID}(f) = A \cdot kT \cdot \frac{I_D^2 \cdot \kappa^2 \cdot n_t(E_{\mathrm{FN}})}{\gamma \cdot N^2 \cdot f^{\alpha}}, \tag{5-24}$$

where A is the gate area, kT is the thermal energy, N is the total number of channel carriers per unit area, γ is the attenuation coefficient in the WKB approximation, κ is the parameter combining carrier number and correlated mobility fluctuations (κ=1 for the number fluctuation model and κ>1 for the unified model), and $n_t(E_{\mathrm{FN}})$ is the trap density at the quasi-Fermi level with a unit of $cm^{-3}eV^{-1}$. Rewriting this equation for applied stress in terms of the measured quantities in Table 5-1, we obtain

$$\ln\left(1+\frac{\Delta S_{ID}(f;\sigma)}{S_{ID}(f;0)}\right)=\ln\left(1+\frac{2\Delta I_D(\sigma)}{I_D(0)}\right)+\ln\left(1+\frac{2\Delta\kappa(\sigma)}{\kappa(0)}\right)+\ln\left(1+\frac{\Delta n_t(E_{\mathrm{FN}};\sigma)}{n_t(E_{\mathrm{FN}};0)}\right)$$
$$-\ln\left(1+\frac{\Delta\gamma(\sigma)}{\gamma(0)}\right)-\ln\left(1+\frac{2\Delta N(\sigma)}{N(0)}\right)-\Delta\alpha(\sigma)\cdot\ln f. \tag{5-25}$$

The above expression is further simplified since the fourth and fifth terms can be neglected. The attenuation coefficient γ is defined by

$$\gamma=\frac{2}{\hbar}\cdot\sqrt{2m_{ox}^{*}\Phi_{\mathrm{B}}}, \tag{5-26}$$

where m_{ox}^{*} is the effective mass of channel carriers in the oxide, and Φ_{B} is the oxide barrier height seen by channel carriers at the interface.

Here Φ_{B} is a function of stress and the strain-induced change $\Delta\Phi_{\mathrm{B}}(\sigma)$ is only a few meV for our stress level of 200MPa compared with $\Phi_{\mathrm{B}}(0)$=3.15eV for conduction band electrons and 4.5eV for valence band holes [13, 47-48]. Thus, $\Delta\gamma(\sigma)/\gamma(0)<<1$. The total number change in channel carriers due to stress, $\Delta N(\sigma)/N(0)$, can be written in terms of the drain (I_D) and gate tunneling (I_G) currents in steady-state condition,

$$\frac{\Delta N(\sigma)}{N(0)}=\frac{I_G(0)}{I_D(0)+I_G(0)}\cdot\frac{\Delta I_G(\sigma)}{I_G(0)}. \tag{5-27}$$

This quantity is also very small. Then, from Eq. (5-23) and (5-25) through (5-27),

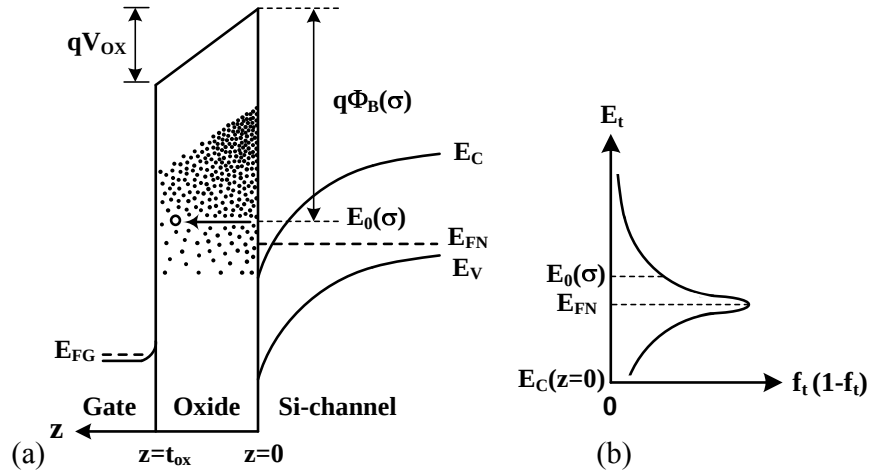

Figure 5-14. Schematic band diagram of an n-channel MOSFET under mechanical stress. Dots are symbolized as oxide traps. Traps are shifted by the amount of oxide band bending (qV_{ox}) when a gate bias is applied. Applying stress alters inversion subband energy levels at which tunneling electrons encounter less or more traps depending on the energy distribution of traps. (a) Trapping of channel charge carriers through an elastic direct tunneling mechanism. With increasing tensile stress, the ground energy level (E_0) of the inversion channel electrons continues to lower and get closer to the electron quasi-Fermi level (E_{FN}). The noise PSD increases under tensile stress since trapping probability increases as the energy level of tunneling electrons move closer to E_{FN}. (b) Trap occupation function product $f_t(1-f_t)$ versus trap energy E_t. Trapping probability is proportional to $f_t(1-f_t)$.

$$\ln\left(1+\frac{\Delta S_{ID}(f;\sigma)}{S_{ID}(f;0)}\right)=\ln\left(1+\frac{2\Delta I_D(\sigma)}{I_D(0)}\right)+\ln\left(1+\frac{2\Delta\kappa(\sigma)}{\kappa(0)}\right)+\ln\left(1+\frac{\Delta n_{t,\mathrm{eff}}(E_{\mathrm{FN}};\sigma)}{n_{t,\mathrm{eff}}(E_{\mathrm{FN}};0)}\right)-\Delta\alpha(\sigma)\cdot\ln f, \tag{5-28}$$

and

$$\ln\left(1+\frac{\Delta S_{ID}(1Hz;\sigma)}{S_{ID}(1Hz;0)}\right)=\ln\left(1+\frac{2\Delta I_D(\sigma)}{I_D(0)}\right)+\ln\left(1+\frac{2\Delta\kappa(\sigma)}{\kappa(0)}\right)+\ln\left(1+\frac{\Delta n_{t,\mathrm{eff}}(E_{\mathrm{FN}};\sigma)}{n_{t,\mathrm{eff}}(E_{\mathrm{FN}};0)}\right). \tag{5-29}$$

The magnitude change in noise PSD due to strain has been expressed with three terms in Eq. (5-29). Roughly estimated using our measured data in Table 5-1, half of the total magnitude change in PSDs comes from the last two terms in Eq. (5-29). It is mentioned by some literature that the oxide trap density $n_t(E_{FN})$ should change with strain, but in our experiments, the 3rd term is not necessarily a result of the trap density change. As mentioned earlier, it is due to strain-induced

trapping position change in energy space, and is also related to spatial trap distribution. In this sense, we use the effective change in trap density ($\Delta n_{t,\mathrm{eff}}/n_{t,\mathrm{eff}}$) instead of the direct change ($\Delta n_t/n_t$) as in Eqs. (5-28) and (5-29). Now, we examine the last two terms in Eq. (5-29) in more detail. In order to obtain a general form of the $1/f^{\alpha}$ spectrum since our measurements extract the stress dependence of the exponent α, we assume that the oxide traps are distributed exponentially over energy (E) and space (z) as assumed elsewhere [76]. It is also assumed that the traps are distributed continuously along the oxide depth direction for our ultrathin (1.3nm) gate oxide samples since the gate areas (50μm^2 and 100μm^2) are very large. Thus, the trap density is represented as

$$n_t(E,z) = n_{t0} \cdot \exp\left[\xi \cdot E + \eta \cdot z\right], \tag{5-30}$$

where n_{t0} is the trap density at the interface (z=0) with the Si band edge (E_C or E_V) at z=0, and ξ and η are the trap distribution coefficients over energy and space with units of meV^{-1} and nm^{-1}, respectively. Referring to Fig. 5-14 (a) for the coordinate system, under mechanical stress and gate bias, the trap distribution seen by tunneling channel carriers at the ground energy level (E_0) is given by

$$n_t(E_0,z;\sigma) = n_{t0}(\sigma) \cdot \exp\left[\xi(\sigma) \cdot q\left(|V_{ox}|\frac{z}{t_{ox}} - \Delta\Phi_{\mathrm{B}}(\sigma)\right) + \eta(\sigma) \cdot z\right], \tag{5-31}$$

where the terms in the exponential argument are due to oxide band bending, applied stress, and spatial trap distribution, respectively. In general, the parameters, n_{t0}, ξ and η, are functions of mechanical stress since applied stress can alter the trap distribution by affecting both trap energy and existing interface strain between the Si-channel and the oxide. The signs for ξ and η are positive (negative) for the exponential increase (decrease) for increasing distance from the

interface and increasing energy above the Si band edge. For clarification, we also state the signs of $\Delta\Phi_B(\sigma)$, that is

$$\Delta\Phi_B(\sigma) = \begin{cases} > 0 \text{ for n-channel MOSFET under tensile stress and} \\ \qquad \text{p-channel MOSFET under compressive stress} \\ < 0 \text{ for n-channel MOSFET under compressive stress and} \\ \qquad \text{p-channel MOSFET under tensile stress.} \end{cases} \tag{5-32}$$

These signs of $\Delta\Phi_B(\sigma)$ reflect the ground energy level shifts in the inversion layer for applied different types of stresses. Trapping by channel carriers in higher energy levels is neglected since the contribution to noise PSD is much smaller. The integral form of the drain current *1/f* noise PSD in the charge trapping model is written as [59, 75-78]

$$S_{ID}(f) = A \cdot \left(\frac{I_D}{N}\right)^2 \cdot \kappa^2 \cdot \int_{E_{Vox}}^{E_{Cox}} 4n_t(E,z) \cdot f_t(1-f_t) \cdot dE \int_0^{t_{ox}} \frac{\tau(E,z)}{1+\omega^2\tau^2(E,z)} \cdot dz, \tag{5-33}$$

where f_t is the trap occupation function, τ is the trap time constant, and E_{Cox} and E_{Vox} are the oxide conduction and valence band edges, respectively. The expression is valid for a low drain bias [59, 75-76]. Eq. (5-53) can be rewritten for applied mechanical stress, using Eq. (5-31), as

$$S_{ID}(f;\sigma) = A \cdot \left[\frac{I_D(\sigma)}{N}\right]^2 \cdot \kappa^2(\sigma) \cdot \exp\left[-\xi(\sigma) \cdot q\Delta\Phi_B(\sigma)\right] \cdot \int_{E_{Vox}}^{E_{Cox}} 4n_{t0}(\sigma) \cdot f_t(\sigma) \cdot \left[1-f_t(\sigma)\right] \cdot dE$$
$$\cdot \int_0^{t_{ox}} \frac{\tau(\sigma) \cdot \exp\left[\left(\xi(\sigma) \cdot q\left|V_{ox}\right| / t_{ox} + \eta(\sigma)\right) \cdot z\right]}{1+\omega^2\tau^2(\sigma)} \cdot dz, \tag{5-54}$$

where $f_t(\sigma) = \left[1 + \exp\left(\frac{E - E_{FN} - q \cdot \Delta\Phi_B(\sigma)}{kT}\right)\right]^{-1}$ and $\tau(\sigma) = \tau_0 \exp\left[\gamma(\sigma) \cdot z\right]$.

The stress-dependent trap occupation function, $f_t(\sigma)$, is introduced to describe the stress dependence of the trapping probability of tunneling channel carriers by oxide traps.

Strain effect on the exponent α in *1/f*$^{\alpha}$ noise power spectrum

From the second integral in Eq. (5-54), we obtain a general form of the $1/f^{\alpha(\sigma)}$ spectrum, where $\alpha(\sigma)$ is defined by

$$\alpha(\sigma) = 1 + \frac{\xi(\sigma)\cdot q\left|V_{ox}\right|/t_{ox} + \eta(\sigma)}{\gamma(\sigma)}. \tag{5-55}$$

The signs of ξ and η are ξ>0 and η<0 in the literature [65, 72, 76-77, 79]. We also confirmed that ξ>0 with our gate bias dependence measurements of the exponent α for both n- and p-channel samples. Typical values of ξ, η and γ are cited to be ~0.02/meV, ~ -3/nm and ~10/nm, respectively [72, 75-77, 79]. Referenced to the measured values of Δα(σ) in Table 5-1 and using Eq. (5-55), Δα(σ) is estimated approximately as

$$\begin{aligned}\left|\Delta\alpha(\sigma)\right| &\cong \frac{\left|\Delta\xi(\sigma)\cdot q\left|V_{ox}\right|/t_{ox} + \Delta\eta(\sigma)\right|}{\gamma(0)} \\ &= \sim 0.008 \text{ for } \sigma = 100\text{MPa at } V_G = 0.6\text{V},\end{aligned} \tag{5-56}$$

where $\Delta\xi(\sigma)$ and $\Delta\eta(\sigma)$ are changes due to trap redistribution over energy and space under stress. Physically, both changes are possible since stress alters both trap energy states by affecting the bonding energy of SiO_2 and the existing interface strain between the Si-channel and oxide. It is roughly estimated that $\left|\Delta\xi(\sigma)\right| = \sim 5\times10^{-4}$ /meV and $\left|\Delta\eta(\sigma)\right| = \sim 0.05/nm$ at a stress of 100MPa. The sign of $\Delta\alpha(\sigma)$ is positive (negative) for n-channel MOSFETs under tensile (compressive) stress. In order to account for our measured data of $\Delta\alpha(\sigma)$, traps must redistribute over energy and space for applied stress. Fig. 5-15 illustrates the stress dependence of the trap distributions in energy and space. As shown in the figure, applying tensile (compressive) stress to an n-channel MOSFET causes the oxide traps to move toward higher (lower) energy and spatially deeper (shallower) oxide regions. The exponent $\alpha(\sigma)$ then increases (decreases) for tensile (compressive) stress since trapping occurs more at spatially deeper (shallower) regions into the oxide. Note that trap redistribution to a higher (lower) energy region under oxide band bending yields the same effect on the exponent change $\Delta\alpha(\sigma)$ as trap redistribution to a spatially deeper

(shallower) oxide region as implied in Eq. (5-31). Under an assumption of sorely pure trap redistribution due to applied stress, there is no net increase or decrease in number of traps, that is

$$\iint_{E,z} n_t(E,z;0)dz \cdot dE = \iint_{E,z} n_t(E,z;\sigma)dz \cdot dE. \tag{5-57}$$

This assumption is likely to be valid for our maximum applied mechanical stress level of 200MPa since the strained energy is much less than the chemical bond energy of a Si-O bond in SiO_2.

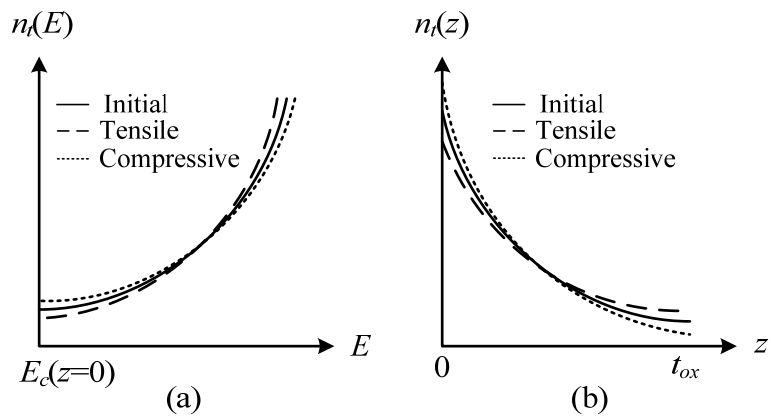

Figure 5-15. Trap redistribution for an n-channel MOSFET under mechanical stress. In our wafer bending experiments, the oxide layer is also stressed as well as the Si-channel. Applied mechanical stress may cause oxide traps to redistribute over energy and space. (a) Energy distribution of traps from the conduction band edge. (b) Spatial distribution of traps from the oxide-channel interface.

Strain effect on the noise PSD magnitude

Change in trapping probability of tunneling carriers by oxide traps

Assuming that the total number of oxide traps remains constant during redistribution as defined in Eq. (5-57), the trap redistribution effect can be neglected compared with the other strain effects although it can affect the magnitude change in noise PSD. In the first integral of Eq. (5-54), the maximum relative change in trapping probability under strain is given by

$$\frac{f_t(\sigma)\cdot[1-f_t(\sigma)]-f_t(0)\cdot[1-f_t(0)]}{f_t(0)\cdot[1-f_t(0)]} = [q\Delta\Phi_B(\sigma)/kT]. \tag{5-58}$$

This relation is obtained for trapping occurring far away from the Fermi level (E_0-E_F >3kT). At a stress of 100MPa, the maximum values of the relative change in trapping probability are calculated to be 0.066 for an n-channel MOSFET and 0.104 for a p-channel MOSFET. Fig. 5-16 shows the relative change in trapping probability as a function of energy of tunneling carriers at an applied stress of 100MPa.

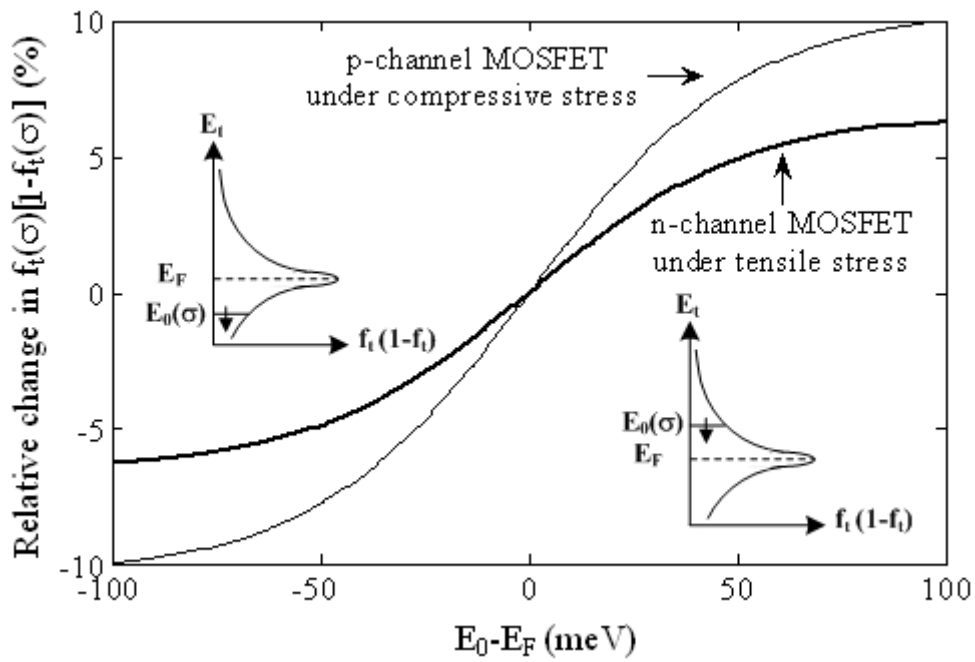

Figure 5-16. Relative change in trapping probability vs. tunneling channel carrier energy for an applied stress of 100MPa. The plots are made with an energy level shift $q\Delta\Phi_B(\sigma)$=1.7meV for an n-channel MOSFET and 2.7meV for a p-channel MOSFET at 100MPa. The energy level shift of 2.7meV for valence bands has been calculated based on the 4-band strain Hamiltonian [8].

At low gate biases the ground energy level E_0 of the inversion channel carriers are higher than the Fermi energy, E_F. The trapping probability for these tunneling carriers increases for n-channel (p-channel) MOSFETs with increasing tensile (compressive) stress, whereas its relative change decreases. At high gate biases where E_0 lies below E_F, the trapping probability decreases and the magnitude of its relative change increases. This behavior is desirable from the viewpoint

of device applications since both gate leakage and *1/f* noise can be reduced while drain current is enhanced.

Change in correlated mobility fluctuations of channel charge carriers

The factor κ in Eq. 5-54 is given by [59, 78]

$$\kappa = 1 + S \cdot \mu_{eff} \cdot N, \tag{5-59}$$

where S is the scattering parameter, μ_{eff} is the effective mobility limited by all the scattering mechanisms except for Coulombic scattering by oxide charges, and N is the total number of channel carriers per unit area. The strain induced change $\Delta\kappa(\sigma)/\kappa(0)$ is then

$$\frac{\Delta\kappa(\sigma)}{\kappa(0)} = \frac{\mu_{eff}(0) \cdot N \cdot \Delta S(\sigma) + S(0) \cdot N \cdot \Delta\mu_{eff}(\sigma)}{1 + S(0) \cdot \mu_{eff}(0) \cdot N}, \tag{5-60}$$

where the stress dependence of S is caused by the fact that stress alters the average distance of the channel carriers in the ground energy level from the oxide/channel interface through carrier repopulation among inversion subbands [78, 80]. The scattering parameter is approximately dependent upon an average distance (d_{ave}) between the scattering charge and channel carriers [65, 72, 78, 81], that is

$$S(d_{\text{ave}}) \approx 2S_0 \ln\left[1 + (r_{\max} / d_{\text{ave}})\right] \text{ with } r_{\max} \approx (\varepsilon_{ox} + \varepsilon_{Si})/(C_{ox} + C_{Si}). \tag{5-61}$$

For our ultrathin gate oxide samples, $r_{\max}$ is calculated to be ~5nm. The value of S is typically taken ~2×10^{-15}Vs [59, 65, 72]. With this value of S and a typical mobility value of S and a typical mobility value of 500 cm^2/Vs, we can rewrite Eq. (5-60) as

$$\frac{\Delta\kappa(\sigma)}{\kappa(0)} \cong \frac{4}{5}\left(\frac{\Delta S(\sigma)}{S(0)} + \frac{\Delta I_D(\sigma)}{I_D(0)}\right). \tag{5-62}$$

It should be noted that $\mu_{eff}(\sigma)/\mu_{eff}(0) \cong I_D(\sigma)/I_D(0)$ for long channel devices at low gate and drain biases [73], and that N is calculated to be ~$4\times10^{12}/cm^2$ for our MOSFET samples at the measurement bias condition using the relation $N = C_{ox}(V_G - V_t)/q$.

Estimation of total magnitude change in noise PSD

Returning to Eq. (5-29) compared with Eq. (5-54) and using Eqs (5-58) and (5-62), we finally obtain an expression for the magnitude change in noise PSD as follows,

$$\ln\left(1+\frac{\Delta S_{ID}(1Hz;\sigma)}{S_{ID}(1Hz;0)}\right)=\ln\left(1+\frac{2\Delta I_D(\sigma)}{I_D(0)}\right)+\ln\left[1+\frac{8}{5}\left(\frac{\Delta S(\sigma)}{S(0)}+\frac{\Delta I_D(\sigma)}{I_D(0)}\right)\right]+\ln\left(1+\frac{\Delta I_G(\sigma)}{I_G(0)}\right)$$
$$+\ln\left(1+\lambda\cdot\frac{q\Delta\Phi_{\mathrm{B}}(\sigma)}{kT}\right)-\xi(\sigma)\cdot q\Delta\Phi_{\mathrm{B}}(\sigma), \qquad (5\text{-}63)$$

where λ is a gate bias dependent parameter with its value ranging from -1 to 1. The third term in the equation is included to account for the strain-induced change in tunneling probability of channel carriers and the last term arises from the nonuniform energy distribution of traps which describes whether the tunneling channel carriers encounter less or more traps. In estimating the noise PSD magnitude for our measurements, we use the following values for n- and p-channel MOSFETs for an applied stress of 100MPa: $q\Delta\Phi_B(\sigma)$=1.7meV (n-channel) and 2.7meV (p-channel), $\xi(\sigma)$=0.02/meV (both n- and p-channel), λ=0.6 (n-channel) and 0.8 (p-channel), and $\Delta S(\sigma)/S(0)$ =±0.01 (both n- and p-channel). Here λ has been determined on the basis of the triangular well approximation of inversion layers. Note that the quantization effective mass of the carriers occupying the ground energy level is about three times larger for electrons than for holes ($0.92m_0$ vs. $0.29m_0$). Based on Eq. (5-61), $\Delta S(\sigma)/S(0)$ can be also estimated using the triangular well approximation and charge density expression for inversion subbands. The negative value of $\Delta S(\sigma)/S(0)$ is applied to an n-channel MOSFET under compressive stress. The calculated values for $\Delta S_{ID}(1Hz;\sigma)/S_{ID}(1Hz;0)$ are listed in comparison with the measured ones in Table 5-2, where the measured values of drain and gate currents [$I_D(\sigma)/I_D(0)$ and $I_G(\sigma)/I_G(0)$] are partly used for the calculations. In Eq. (5-63), the fourth and fifth terms have opposite signs for low gate and drain biases (*e.g.*, $|V_G - V_t|$=~ 0.3V, $|V_D|$=~ 0.1V). As a result, the actual sum of

the last three terms which is equivalent to the effective oxide trap change, $\ln\left[1+\Delta n_{t,\mathrm{eff}}(E_{\mathrm{F}};\sigma)/n_{t,\mathrm{eff}}(E_{\mathrm{F}};0)\right]$, in Eq. (5-29) is much smaller than the first two terms. In these bias ranges, the stress altered channel mobility $\mu_{\mathrm{eff}}(\sigma)$ is primarily responsible for the total change in drain current PSD under strain since both the change in drain current, $\Delta I_D(\sigma)/I_D(0)$, and correlated mobility fluctuations, $\Delta\kappa(\sigma)/\kappa(0)$, mainly results from the change in channel mobility, $\Delta\mu_{\mathrm{eff}}(\sigma)/\mu_{\mathrm{eff}}(0)$. Thus, Eq. (5-63) can be simply approximated as,

$$\begin{aligned}\ln\left(1+\frac{\Delta S_{ID}(1Hz;\sigma)}{S_{ID}(1Hz;0)}\right) &\cong \ln\left(1+\frac{2\Delta I_D(\sigma)}{I_D(0)}\right)+\ln\left[1+\frac{8}{5}\left(\frac{\Delta S(\sigma)}{S(0)}+\frac{\Delta I_D(\sigma)}{I_D(0)}\right)\right] \\ &\cong \ln\left(1+\frac{4\Delta I_D(\sigma)}{I_D(0)}\right).\end{aligned} \tag{5-64}$$

Eq (5-64) seems to be very useful from the practical point of view because we can easily estimate the noise magnitude change, $\Delta S_{ID}(1Hz;\sigma)/S_{ID}(1Hz;0)$, after simply measuring or calculating only the drain current change with strain, $\Delta I_D(\sigma)/I_D(0)$. As shown in Table 5-2, the calculated values of $\Delta S_{ID}(1Hz;\sigma)/S_{ID}(1Hz;0)$ are not so different for Eqs. (5-63) and (5-64). In this section, we have discussed four causes of the magnitude change in *1/f* noise PSD under strain; changes in (1) trapping probability of tunneling carriers by oxide traps (2) tunneling probability of channel carriers (3) correlated mobility fluctuations of channel charge carriers, and (4) available traps encountered by tunneling channel carriers due to nonuniform trap distribution in energy. These effects result directly from the modification of Si inversion subband energy levels by strain. In addition, strain effects on oxide traps were investigated. To explain our experimental observation that the exponent α in $1/f^{\alpha}$ noise spectrum is varied with applied stress, oxide traps must be redistributed over energy, or space, or both. The strain-induced change in the exponent, $\Delta\alpha(\sigma)$, is predicted to be a function of gate voltage as indicated in Eq. (5-56). A larger

value of $\Delta\alpha(\sigma)$ should be measured for a higher gate voltage, which is consistent with our measurements in Table 5-1.

Table 5-2. Comparison of the measured and calculated relative magnitude changes in drain current noise PSD, $\Delta S_{ID}(1Hz;\sigma)/S_{ID}(1Hz;0)$, at a stress of 100MPa.

Device/Stress		Measurement	Calculation
n-channel MOSFET under tension		11.9 %	14.9 (15.1) %
n-channel MOSFET under compression		-16.2 %	-11.4 (-11.9) %
p-channel MOSFET under compression	V_G= -0.6V	19.2 %	22.0 (20.28) %
	V_G= -0.8V	22.9 %	19.9 (19.2) %

*The relative magnitude changes in noise PSD, ΔSID(1Hz;σ)/SID(1Hz;0), were estimated with some measured values [ID(□)/ID(0) and IG(□)/IG(0)] and calculated values (λ, ΔΦB(□), S) using Eqs. (5-63) and (5-64). The values in the parenthesis were calculated using Eq. (5-64)

Summary

We examined detailed mechanisms of strain effects on noise PSD based on our measured data. It was shown that the applied mechanical stress altered both the magnitude and exponent in the $1/f^{\alpha}$ noise spectrum, resulting in larger changes in noise PSD at lower frequencies. The magnitude in *1/f* noise drain current PSD was measured to increase and decrease for n-channel MOSFETs with increasing tensile and compressive stress, respectively, while it increased for p-channel MOSFETs with increasing compressive stress. The dominant factors affecting *1/f* noise magnitude were identified and investigated. One of the main factors is a trapping position change in energy space. Since its contribution to noise PSD is solely determined by the relative distance from the quasi-Fermi level, there is some possibility we can suppress the noise arising from this factor through proper choice of gate bias or strain engineering. More specifically, the quantization effective mass which determines the lowest energy level in the inversion layer is approximately three times larger for electrons than for holes. At a relatively lower gate bias compared to p-channel MOSFETs, n-channel MOSFETs can be biased such that the ground energy levels are located below the Fermi level, and thus the *1/f* noise PSD can be reduced by

applied stress. The energy distribution of the oxide traps was shown to reduce the *1/f* noise PSD magnitude for both n-channel MOSFETs under tensile strain and p-channel MOSFETs under compressive strain. The stress altered channel mobility, $\mu_{\text{eff}}(\sigma)$, was also shown to be a key contributor to the noise PSD change especially at low gate and drain biases. In long channel devices, the noise PSD magnitude change is approximately related to the drain current change as,

$$\Delta S_{ID}(1Hz;\sigma)/S_{ID}(1Hz;0) \cong 4\Delta I_D(\sigma)/I_D(0).$$

CHAPTER 6
SUMMARY AND RECOMMENDATIONS FOR FUTURE WORK

Summary

In this dissertation, the effects of strain on the CMOS transistor operation such as threshold voltage, gate tunneling current, and *1/f* noise characteristics have been investigated. Strain effects on both conduction and valence energy bands are first presented in Chap 2. Using the elastic compliance constants (*S*-matrix elements), the deformation potentials of the conduction and valence bands are calculated, and the band edge shift and splitting are discussed as strain effects. Each component of the model is also analyzed thoroughly in conjunction with its underlying physical mechanism.

In Chap 3, stress-applying apparatuses of uniaxial and biaxial jigs are introduced. Based on the deformation potential calculation method in Chapter 2, key band parameters to affect the threshold voltage are obtained as a function of strain. Large differences in the strain-induced threshold voltage shifts for uniaxial and biaxial tensile strained Si n-channel MOSFETs are explained and quantified. The calculated threshold voltage shift is significantly larger for biaxial than uniaxial strained MOSFETs and is in agreement with uniaxial wafer bending and published biaxial strained Si on relaxed $Si_{1-x}Ge_x$ experimental data. The large threshold shift for biaxial strain results from the strain-induced change in the Si channel electron affinity (or conduction band offset) and bandgap. The small threshold voltage shift for uniaxial process tensile strain results since the n+ poly–Si gate in addition to the Si channel is strained and significantly less bandgap narrowing occurs for uniaxial than biaxial tensile strain.

In Chap. 4, strain effects on gate tunneling current are discussed. The detailed gate tunneling model for both n- and p-MOSFETs is then constructed. An experimental method to determine both the hydrostatic and shear deformation potential constants is introduced. The technique is based on the change in the gate tunneling currents of Si n-MOSFETs under

externally applied mechanical stress and has been applied to industrial long channel (2μm and 4μm) MOSFETs. The conduction band hydrostatic and shear deformation potential constants (Ξ_d and Ξ_u) are extracted to be 1.0±0.1 eV and 9.6±1.0 eV, respectively, which is consistent with recent theoretical works.

In Chap. 5, *1/f* noise PSD (Power Spectral Density) for both n- and p-MOSFETs has been measured and analyzed under externally applied mechanical stress in conjunction with applications of strained devices to high performance RF or high speed CMOS circuits. It is observed that (1) *1/f* noise PSD increases and decreases for n-channel MOSFETs with increasing tensile and compressive stress, respectively, while it increases for p-channel MOSFETs with increasing compressive stress. (2) The relative change in PSDs shows a frequency dependence (i.e., larger changes for lower frequencies) since strain alters both the noise magnitude and exponent. The observed trends have been explained by a strain-induced energy level shift mechanism in the inversion layer. More specifically, four causes of the magnitude change in *1/f* noise PSD were discussed: changes in (1) trapping probability of channel carriers by oxide traps (2) tunneling probability of channel carriers (3) correlated mobility fluctuations, and (4) available traps encountered by tunneling channel carriers due to nonuniform trap distribution in energy. These effects result directly from the modification of Si inversion subband energy levels by strain. Strain effects on oxide traps were also investigated. To explain our experimental observation that the exponent α in $1/f^{\alpha}$ noise spectrum is varied ith applied stress, oxide traps must be redistributed over energy or space or both.

Recommendations for Future Work

The demand for new material and technologies becomes increasing in the nanometer CMOS regime. The downscaling of device dimensions causes the gate leakage current to increase exponentially, thus increasing the *1/f* noise significantly. Especially in conjunction with

high-k gate dielectric MOSFETs, low-frequency *1/f* noise measurements can be used as a valuable tool for quality and reliability evaluations of these devices since the low-frequency noise in a device is sensitive to the device technology such as the presence of traps, defects and crystal damage [82].

In the noise measurements of our ultrathin (1.3nm) gate oxide MOSFET samples, *1/f* noise power spectrums have been observed in low frequency regions (< ~10Hz), contrary to the conventional charge trapping model. It is expected in the conventional model that the tunneling time is very fast for this thin gate oxide. As a result, no 1/*f* noise spectrums would be observed at such low frequencies as f < ~10Hz. A roll-off in the spectrum would be instead expected below a frequency corresponding to the tunneling time to the farthest situated traps at t_{ox}=1.3nm. This observation of 1/f noise spectrums in low frequency regions is important since it can be a new research topic for highly scaled CMOS devices.

APPENDIX A
CONDUCTION BAND DEFORMATION POTENTIALS FOR GE

In Chapter 2, we reviewed the conduction band deformation potentials for Si. It was shown that the behavior of Δ-valleys was critical to determine the physical properties of Si MOSFETs since the Δ-valleys form the lowest conduction energy bands. In Ge, however, the conduction band minima are Λ-valleys, which are located along the eight equivalent directions of [111]. In this case, Eq. (2-11) is no longer valid to use. A more general expression can be found in the original notation of Herring and Vogt [2, 8, 29, 30]:

$$\Delta E_C^i = \left[\Xi_d \overleftrightarrow{1} + \Xi_u \left\{ \hat{a}_i \hat{a}_i \right\} \right] : \overleftrightarrow{\varepsilon} \,, \tag{A-1}$$

where $\overleftrightarrow{\varepsilon}$ and $\overleftrightarrow{1}$ are the 2nd order strain and unit tensors, respectively, $\hat{a}_i$ is a unit vector parallel to the $\vec{K}$ vector of valley i, and $\left\{ \hat{a}_i \hat{a}_i \right\}$ denotes a dyadic product. In Eq. (A-1), the hydrostatic and shear strain components are written as

$$\Delta E_C^{Hydro} = \left[\Xi_d + \frac{\Xi_u}{3} \right] \overleftrightarrow{1} : \overleftrightarrow{\varepsilon},$$

and

$$\Delta E_C^{Shear} = \left[\Xi_u \left\{ \hat{a}_i \hat{a}_i \right\} - \frac{\Xi_u}{3} \overleftrightarrow{1} \right] : \overleftrightarrow{\varepsilon} \tag{A-2}$$

As mentioned in Section 2.1, a dyad notation is equivalent to a second order tensor representation, and the double dot product (**:**) is defined as [66]

$$\vec{A}\vec{B} : \vec{C}\vec{D} \equiv \left(\vec{A} \cdot \vec{C} \right) \left(\vec{B} \cdot \vec{D} \right) \; for \; any \; two \; dyads \; \vec{A}\vec{B} \; and \; \vec{C}\vec{D}. \tag{A-3}$$

The result of the double dot product produces a scalar quantity, and Eq. (A-3) can be written in a more convenient notation:

$$\vec{A}\vec{B} : \vec{C}\vec{D} = \vec{C} \cdot \vec{A}\vec{B} \cdot \vec{D} \;\; or \;\; \vec{A} \cdot \vec{C}\vec{D} \cdot \vec{B} \tag{A-4}$$

The strain and unit tensors can be also expressed in the dyad notations as follows:

$$\overleftrightarrow{\varepsilon} = \varepsilon_{xx}\hat{i}\hat{i} + \varepsilon_{xy}\hat{i}\hat{j} + ... + \varepsilon_{zz}\hat{k}\hat{k},$$

and $$\overleftrightarrow{1} = \hat{i}\hat{i} + \hat{j}\hat{j} + \hat{k}\hat{k}. \qquad \text{(A-5)}$$

Using Eq. (A-3) and (A-4), we can rewrite the energy shift expression of Eq. (A-1) in a simpler form:

$$\Delta E_C^i = \left[\Xi_d \overleftrightarrow{1} + \Xi_u \left\{\hat{a}_i \hat{a}_i\right\}\right] : \overleftrightarrow{\varepsilon} = \Xi_d \cdot Tr[\varepsilon_{ij}(\sigma)] + \Xi_u \cdot [\hat{K} \cdot \varepsilon \cdot \hat{K}^T], \qquad \text{(A-6)}$$

where $\hat{K}$ and $\hat{K}^T$ are row and column unit vectors, respectively, along the direction of the $\vec{K}$ vector of valley i. As an example, let us calculate the deformation potentials of the Ge conduction band for a uniaxial [110] stress. Fig. A-1 shows the location of eight ellipsoids of Λ-valleys. Four ellipsoids lie on a $(1\bar{1}0)$-plane and another four ellipsoids on a (110)-plane. When a uniaxial [110] stress is applied, these eight valleys can be divided into two groups according to their condition under stress. The four $(1\bar{1}0)$-plane valleys (blue) form one group which is under the same stress condition, and the other four (110)-plane valleys (grey) another group. Since these two groups each are on the same condition under [110] stress, we choose $[111]$- and $[1\bar{1}1]$ valleys, each one from each group for calculation. Using Table 2-1 and Eq. A-6, we can obtain the deformation potentials due to hydrostatic and shear strain components as follows:

$$\begin{aligned}\Delta E_{[111]}^{Hydro} = \Delta E_{[1\bar{1}1]}^{Hydro} &= \left[\Xi_d^{\Lambda(Ge)} + \frac{\Xi_u^{\Lambda(Ge)}}{3}\right] \cdot Tr[\varepsilon_{ij}(\sigma_{Ge})] \\ &= \left[\Xi_d^{\Lambda(Ge)} + \frac{\Xi_u^{\Lambda(Ge)}}{3}\right] \cdot \left(S_{11}^{Ge} + 2S_{12}^{Ge}\right) \cdot \sigma_{Ge}\end{aligned} \qquad \text{(A-7)}$$

$$\Delta E_C^{Shear} = \Xi_u^{\Lambda(Ge)} \cdot \left[\left(\hat{K} \cdot \varepsilon \cdot \hat{K}^T\right) - \frac{Tr[\varepsilon_{ij}(\sigma_{Ge})]}{3}\right] = \begin{cases} \Xi_u^{\Lambda(Ge)} \cdot (S_{44}^{Ge}/6) \cdot \sigma_{Ge} & for\ [111]\ valleys \\ -\Xi_u^{\Lambda(Ge)} \cdot (S_{44}^{Ge}/6) \cdot \sigma_{Ge} & for\ [1\bar{1}1]\ valleys \end{cases} \qquad \text{(A-8)}$$

$$with\ \hat{K}_{[111]} = \frac{1}{\sqrt{3}}(1,1,1),\ \hat{K}_{[1\bar{1}1]} = \frac{1}{\sqrt{3}}(1,-1,1),\ and\ \varepsilon_{[110]} = \begin{pmatrix} \varepsilon_{xx} & \varepsilon_{xy} & 0 \\ \varepsilon_{yx} & \varepsilon_{yy} & 0 \\ 0 & 0 & \varepsilon_{zz} \end{pmatrix}.$$

Note that off-diagonal strain components, ε_{xy} *and* ε_{yx}, are used in the calculation and the Herring and Vogts' formula is consistent with the conventional notation of stress-strain relation. The calculation result shows that the band splitting occurs in a way:

For a tensile [110] stress, the energy of each four valley on a $(1\bar{1}0)$- and a (110)-plane are up-shifted and down-shifted along each valley direction, respectively, by the same magnitude. Typically MOSFETs are fabricated on a (001)-wafer and the channel is located along the [110] direction. In this structure, the gate bias is applied along the [001] direction. Therefore, we need to obtain the effective band splitting in the field direction to correctly evaluate stress effects on the device properties. From Eq. (A-8), the effective band splitting along the [001] direction is obtained by projecting each valley direction onto the [001] direction.

$$\Delta E_C^{Shear} = \begin{cases} \dfrac{\Xi_u^{\Lambda(Ge)}}{\sqrt{3}} \cdot (S_{44}^{Ge}/6) \cdot \sigma_{Ge} & for\ \Lambda_4\ valleys \\ -\dfrac{\Xi_u^{\Lambda(Ge)}}{\sqrt{3}} \cdot (S_{44}^{Ge}/6) \cdot \sigma_{Ge} & for\ another\ \Lambda_4\ valleys \end{cases} \tag{A-9}$$

The band splitting in Ge for other directions is listed in [8].

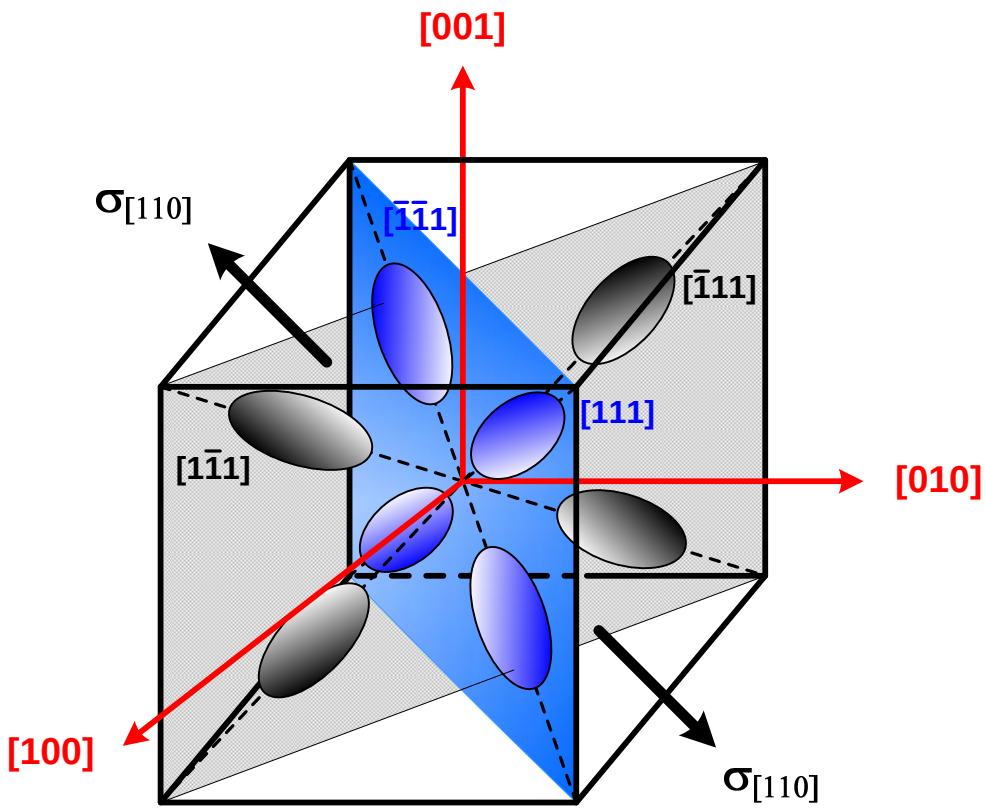

Figure A-1. Eight-fold degenerate Λ-valleys in the Ge conduction band. Under uniaxial [110] stress, the four valleys (blue) on a $(1\bar{1}0)$-plane are on the same stress condition and the other four valleys (grey) on a (110)-plane are on another same stress condition.

APPENDIX B
YOUNG'S MODULUS IN A (110)-SI WAFER

Young's modulus is plotted as a function of angle α in a Si (110)-wafer in Fig. B-1, and the analytical expression is given by [37]

$$Y^{(110)}(\alpha) = \left[S_{11} + (S_{11} - S_{12} - S_{44}/2)(\sin^4\alpha + \cos^4\alpha/2 - 1) \right]^{-1} \tag{B-1}$$

Similarly as in Section 3.1, we can calculate the conversion factor κ. For the purpose of comparison with an in-plane (x- and y-direction) biaxial stress, we take Young's modulus in the [001] direction to be a reference value.

$$\begin{aligned}
\langle Y(\phi) \rangle &= \kappa \cdot Y(\pi/2) \\
&= Y(\pi/2) \cdot \left\langle \left[1 + \left(1 - \frac{S_{12}}{S_{11}} - \frac{S_{44}}{2S_{11}} \right)(\sin^4\alpha + \cos^4\alpha/2 - 1) \right]^{-1} \right\rangle \\
&= Y(\pi/2) \cdot \frac{\int_0^{\pi} \left[1 + \left(1 - \frac{S_{12}}{S_{11}} - \frac{S_{44}}{2S_{11}} \right)(\sin^4\alpha + \cos^4\alpha/2 - 1) \right]^{-1} d\alpha}{\int_0^{\pi} d\alpha} \\
&\cong 1.256 \cdot Y(\pi/2) \cdot
\end{aligned} \tag{B-2}$$

The interval of the integral is chosen from 0 to 180 ° since Young's modulus has a two-fold rotation symmetry about the [001] axis. We can also calculate the conversion factor κ in Ge simply by replacing the elastic compliance constants in Eq. (131) with Ge elastic compliance values.

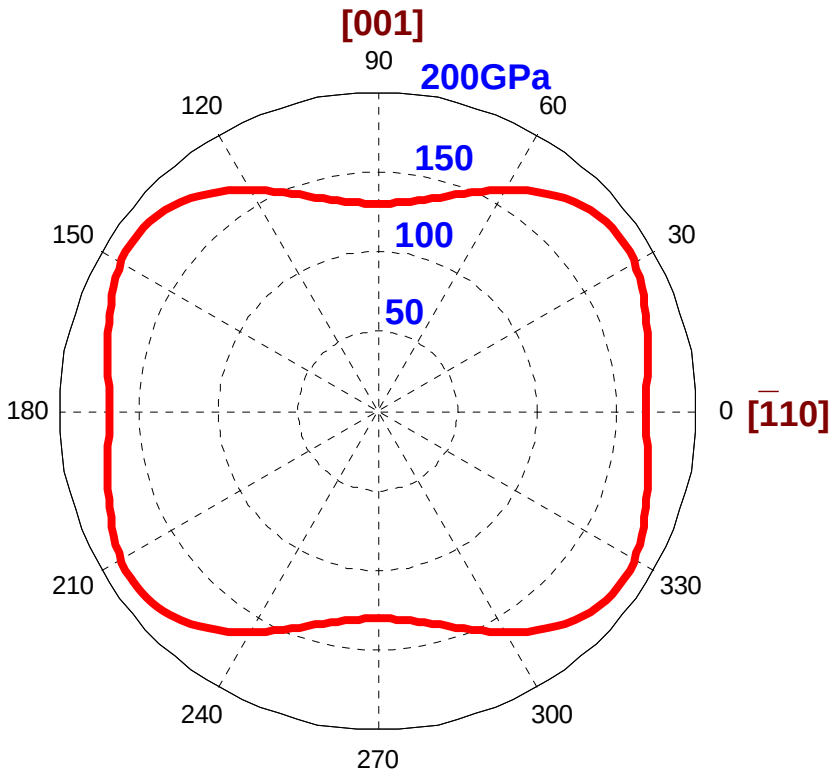

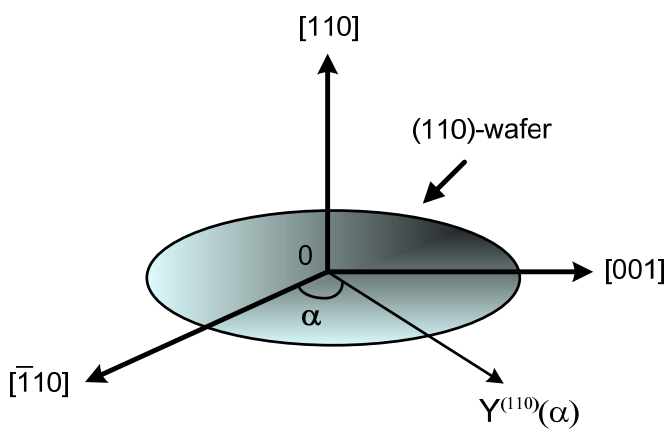

Figure B-1. Young's modulus of Si as a function of direction α in the (110) plane.

APPENDIX C
STRAINED-SI MOFETS ON A (110) WAFER

It is contended in [67, 68] that biaxially-strained Si MOSFETs on a (110)-wafer are advantageous over the conventional counterparts on a (001)-wafer in respect of mobility enhancement. However, in order to accurately compare these two types of (001)- and (110)-wafer MOSFETs in terms of the stress effects on mobility enhancement, we need to first quantify an equivalent stress to the field direction for (110) MOSFETs. In the appendix, we investigate which direction of the strain and channel is desirable for uniaxially-strained (110) MOSFETs to obtain the highest mobility on the bases of deformation potentials and carrier effective masses. Let us first obtain the stress tensor components for an arbitrary stress direction as shown in Fig. C-1. A simple calculation using Eq. (2-7) leads to

$$\left(\sigma_{ij}(\theta,\phi)\right)=\sigma(\theta,\phi)\cdot\begin{pmatrix}\sin^2\theta\cos^2\phi & \sin^2\theta\sin\phi\cos\phi & \sin\theta\cos\theta\cos\phi\\ \sin^2\theta\sin\phi\cos\phi & \sin^2\theta\sin^2\phi & \sin\theta\cos\theta\sin\phi\\ \sin\theta\cos\theta\cos\phi & \sin\theta\cos\theta\sin\phi & \cos^2\theta\end{pmatrix}. \tag{C-1}$$

If we set $\phi=\frac{3\pi}{4}$ and $\theta=\frac{\pi}{2}-\alpha,$ we obtain a stress tensor expression for an arbitrary stress direction in a (110)-plane, and then using Eq. (2-3) through (2-5) we can calculate the strain components as follows:

$$\varepsilon_{xx}^{(110)}(\alpha)=\sigma^{(110)}(\alpha)\cdot\left[\frac{S_{11}+S_{12}}{2}\cdot\cos^2\alpha+S_{12}\sin^2\alpha\right],$$
$$\varepsilon_{yy}^{(110)}(\alpha)=\sigma^{(110)}(\alpha)\cdot\left[\frac{S_{11}+S_{12}}{2}\cdot\cos^2\alpha+S_{12}\sin^2\alpha\right],$$
$$\varepsilon_{zz}^{(110)}(\alpha)=\sigma^{(110)}(\alpha)\cdot\left[S_{11}\sin^2\alpha+S_{12}\cos^2\alpha\right],\qquad \varepsilon_{yz}^{(110)}(\alpha)=\frac{\sigma^{(110)}(\alpha)}{2\sqrt{2}}\cdot S_{44}\sin\alpha\cos\alpha,$$
$$\varepsilon_{xz}^{(110)}(\alpha)=-\frac{\sigma^{(110)}(\alpha)}{2\sqrt{2}}\cdot S_{44}\sin\alpha\cos\alpha,\qquad \varepsilon_{xy}^{(110)}(\alpha)=-\frac{\sigma^{(110)}(\alpha)}{4}\cdot S_{44}\cos^2\alpha, \tag{C-2}$$

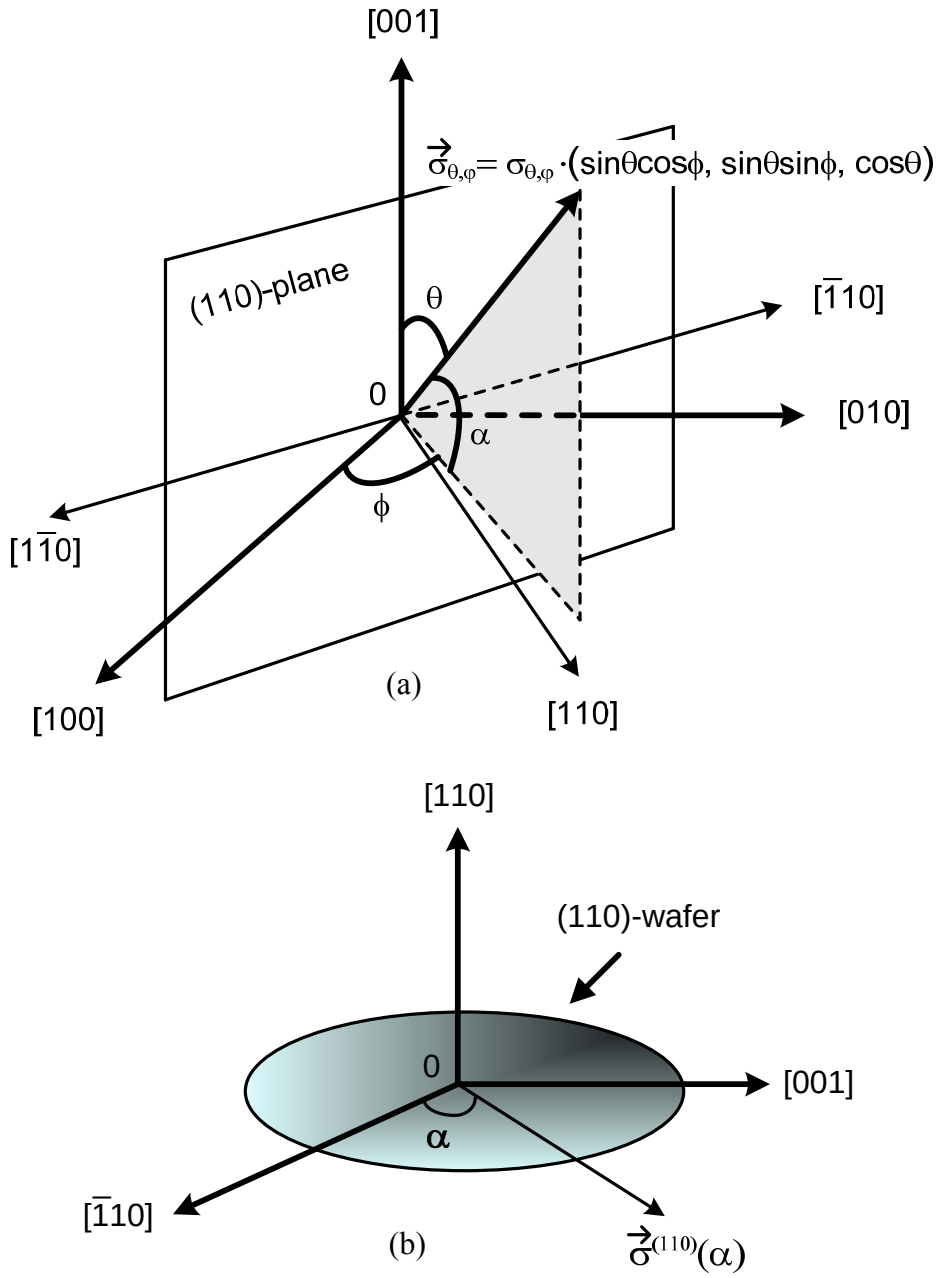

Figure C-1. (a) Representation of an arbitrary stress in a spherical coordinate. (b) New direction α specified in a (110)-wafer.

where the superscript (110) denotes a (110)-wafer and α is a newly specified direction in a (110)-wafer. In order to obtain the effective band splitting along the [110] (or a gate field) direction, we need to first calculate each band splitting for the [100]- and [010]-valleys. From Eq. (2-12), the average energy shift and band splitting for the [100]-valleys are expressed as

$$\begin{aligned}
\Delta E_C^{Hydro}\left(\sigma^{(110)}(\alpha)\right) &= \left(\Xi_d + \frac{\Xi_u}{3}\right)\cdot Tr[\varepsilon_{ij}(\alpha)] = \left(\Xi_d + \frac{\Xi_u}{3}\right)\cdot\left(S_{11}+2S_{12}\right)\cdot\sigma^{(110)}(\alpha), \\
\Delta E_{\Delta_2}^{[100]}\left(\sigma^{(110)}(\alpha)\right) &= \Xi_u \cdot \left(\varepsilon_{xx}(\alpha) - \frac{Tr[\varepsilon_{ij}(\alpha)]}{3}\right) \\
&= \Xi_u \cdot \left(S_{11}-S_{12}\right)\cdot\left(\frac{\cos^2\alpha}{2} - \frac{1}{3}\right)\cdot\sigma^{(110)}(\alpha).
\end{aligned} \tag{C-3}$$

Note that the magnitude of this Δ_2 band splitting is two thirds of the total splitting, as shown in Eq. (2-15). For [010]-valleys as well, we have the same magnitude of the band splitting since in-plane uniaxial stresses in a (110)-wafer are applied symmetrically to the [100]- and [010]-valleys. Fig. C-2 (a) shows the location of six valleys in a (110)-wafer and a band splitting diagram. It is illustrated in the diagram how to calculate the effective band splitting along the [110]-direction. Along both [100]- and [010]-directions, each Δ_2 valley is shifted by two thirds of the splitting as denoted by symbols ① and ② in the figure. More specifically, we first consider the band splitting between the [100] Δ_2-valleys and [010]-[001] Δ_4-valleys along the [100] direction. The two groups split oppositely (① and ①′); the [100] Δ_2-valleys are up-shifted by two thirds of the splitting and the rest Δ_4-valleys are down-shifted by one third. Again, along the [010] direction the [010] Δ_2-valleys are up-shifted by two thirds of the splitting (②) and the [100] Δ_2-valleys and [001] Δ_2-valleys are down-shifted by one third (②′ and ②″). As a result, each pair of valleys of the three directions reaches its final position which is a successive vector sum, that is, ①+②″ for [100] Δ_2-valleys, ①′+② for [010] Δ_2-valleys, and ①′+②′ for

[001] Δ_2-valleys. Therefore, the effective band splitting along the [110] direction is expressed, using Eq. (A-6), as

$$\Delta E_{C\_Spl}^{[110]}(\sigma) = \begin{cases} \frac{\Xi_u}{2} \cdot (S_{11} - S_{12}) \cdot \left(\frac{\cos^2 \alpha}{2} - \frac{1}{3} \right) \cdot \sigma^{(110)}(\alpha) \cdot \cos 45^\circ \ \ for\ \Delta_4\ valleys \\ -\Xi_u \cdot (S_{11} - S_{12}) \cdot \left(\frac{\cos^2 \alpha}{2} - \frac{1}{3} \right) \cdot \sigma^{(110)}(\alpha) \cdot \cos 45^\circ \ \ for\ \Delta_2\ valleys. \end{cases} \tag{C-4}$$

Note that the average band energy level is not changed with shear strain in all directions. Fig. C-2 shows the effective band splitting vs. stress direction, and the conductivity effective mass of Δ_4 valley electrons vs. channel direction. Under a gate bias, the ground energy state becomes a Δ_4 subband since the out-of-effective mass of the electrons in Δ_4 valleys is larger, namely, $m_{\Delta_4}^{*[110]} = \frac{2m_t^* m_l^*}{m_t^* + m_l^*} \cong 0.315 m_0$ *vs.* $m_{\Delta_2}^{*[110]} = m_t^* \cong 0.19 m_0$. Consistent with these quantized energy levels, the strain-induced splitting direction and magnitude must be determined for the carrier mobility to be maximized. In the figure, the splitting direction is changed at $\alpha = \sin^{-1}\left(\frac{1}{\sqrt{3}}\right) \cong 35.3^\circ$, which corresponds to the [111] stress as listed in Table 2-2. At $\alpha = 90°$ ([001] direction) for a tensile stress, the splitting magnitude is maximum, and the direction is consistent with the quantized energy levels; the ground (Δ_2 subband) and 2nd lowest (Δ_4 subband) energy levels are lowered and raised, respectively. It is also shown that the selection of the channel direction for a (110)-wafer MOSFET has a strong influence on carrier mobility because of the anisotropic conductivity effective mass of Δ_4 valleys [67, 68]. An actual calculation yields the following dependence of the effective mass on the channel direction α:

$$m_{(110)}^*(\alpha) = \frac{2m_t^* m_l^*}{m_t^* \cos^2 \alpha + m_l^* (1 + \sin^2 \alpha)}. \tag{C-5}$$

Therefore, both the best stress and channel directions are the [001] direction for a (110)-wafer n-MOSFET as indicated in the plots.

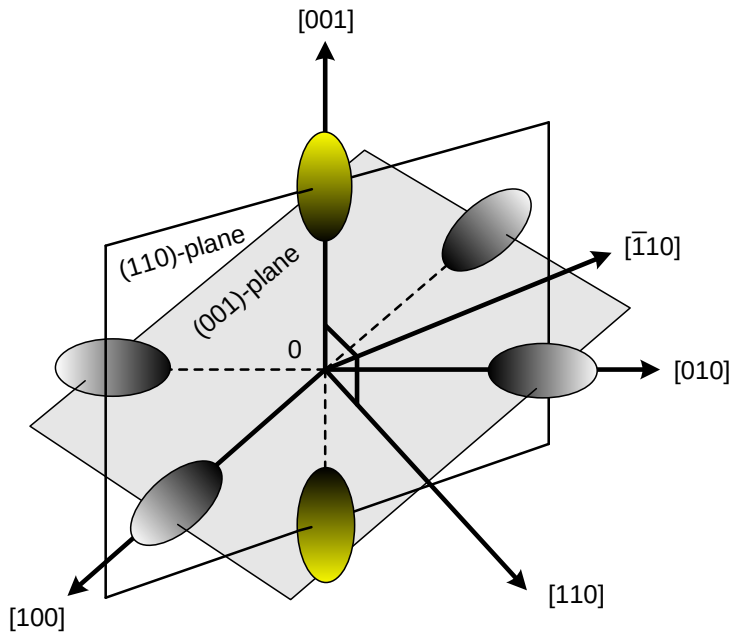

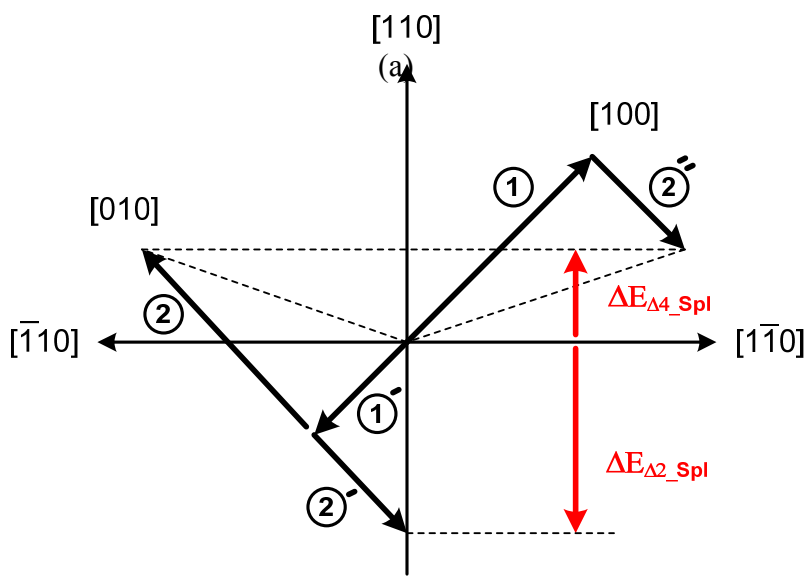

(b)

Figure C-2. (a) Six ellipsoids of Δ-valleys, each lying along the six equivalent axes of [100]. For a (110)-wafer MOSFET, there are two Δ-valleys on the in-plane and four Δ-valleys on the out-of-plane. (b) Diagram for calculating the effective band splitting along the [110]-direction. The red arrows represent the resultant magnitudes and directions of the band splitting along the [110] direction.

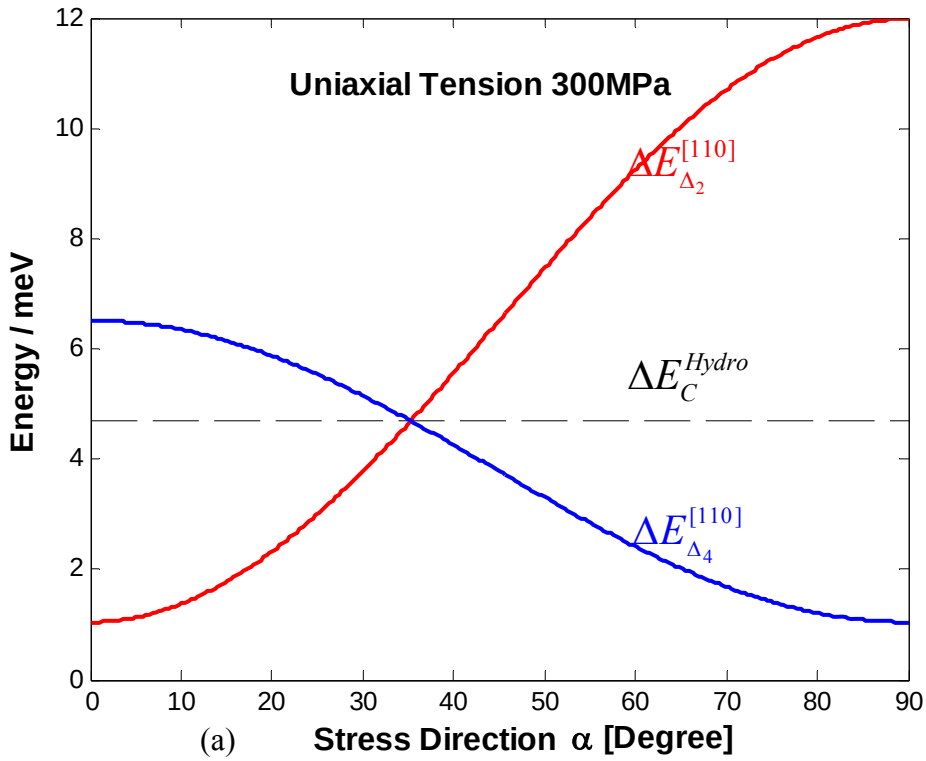

(a)

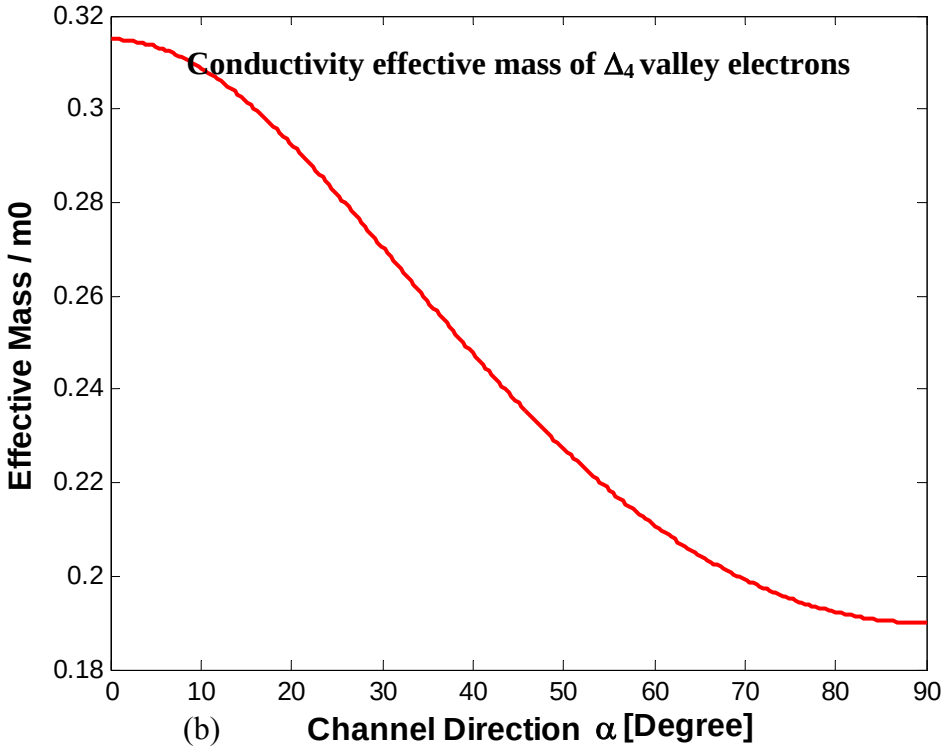

(b)

Figure C-3. (a) Effective band splitting vs. stress direction. (b) Conductivity effective mass of Δ_4 valley electrons vs. channel direction.

LIST OF REFERENCES

[1] J. Bardeen and W. Shockley "Deformation Potentials and Mobilities in Non-Polar Crystals," *Phys. Rev.*, vol. 80, pp. 72-80, 1950.

[2] C. Herring and E. Vogt, "Transport and Deformation-Potential Theory for Many-Valley Semiconductors with Anisotropic Scattering," *Phys. Rev.*, vol. 101, pp. 944-961, 1956.

[3] G. L. Bir and G. E. Pikus, *Symmetry and Strain-Induced Effects in Semiconductors*. New York: John Wiley & Sons, Inc., 1974.

[4] H. Hasegawa, "Theory of Cyclotron Resonance in Strained Silicon Crystals," *Phys. Rev.*, vol. 129, pp. 1029-1040, 1963.

[5] C. S. Smith, "Piezoresistance Effect in Germanium and Silicon," *Phys. Rev.*, vol. 94, pp. 42-49, 1954.

[6] J. E. Aubrey and et al., "Piezoresistance and Piezo-Hall-Effect in n-Type Silicon," *Phys. Rev.*, vol. 130, pp. 1667-1670, 1963.

[7] J. C. Hensel and G. Feher, "Cyclotron Resonance Experiments in Uniaxially Stressed Silicon: Valence Band Inverse Mass Parameters and Deformation Potentials," *Phys. Rev.*, vol. 129, pp. 1041-1062, 1963.

[8] I. Balslev, "Influence of Uniaxial Stress on the Indirect Absorption Edge in Silicon and Germanium," *Phys. Rev.*, vol. 143, pp. 636-647, 1966.

[9] R. N. Bharagava and M. I. Nathan, "Stress Dependence of Photoluminescence in GaAs," *Phys. Rev.*, vol. 161, pp. 695-698, 1967.

[10] F. H. Pollak and M. Cardona, "Piezo-Electroreflectance in Ge, GaAs, and Si," *Phys. Rev.*, vol. 172, pp. 816-837, 1968.

[11] C. Tahan, M. Friesen, and R. Joynt, "Decoherence of electron spin qubits in Si-based quantum computers," *Phys. Rev. B*, vol. 66, pp. 035314, 2002.

[12] M. V. Fischetti and S. E. Laux, "Band Structure, deformation Potentials, and Carrier Mobility in Strained Si, Ge, and SiGe alloys," *J. Appl. Phys.*, vol. 80, pp. 2234-2252, 1996.

[13] J. Lim, X. Yang, T. Nishida, and S. E. Thompson, "Measurement of conduction band deformation constants using gate direct tunneling current in n-type metal oxide semiconductor field effect transistors under mechanical stress," *Appl. Phys. Lett.*, vol. 89, pp. 073509, 2006.

[14] H. M. Manasevit, I. S. Gergis, and A. B. Jones, "Electron mobility enhancement in epitaxial multilayer $Si/Si_{1-x}Ge_x$ alloy films on (100) Si," *Appl. Phys. Lett.*, vol. 41, pp. 464-466, 1982.

[15] R. People and et al., "Modulation doping in Ge_xSi_{1-x}/Si strained layer heterostructures," *Appl. Phys. Lett.*, vol. 45, pp. 1231-1233, 1984.

[16] K. K. Rim, L. H. Judy, and J. F. Gibbons, "Fabrication and Analysis of Deep Submicron Strained-Si N-MOSFETs," *IEEE Trans. Electron Devices*, vol. 47, pp. 1406-1415, 2000.

[17] K. Rim and et al., "Characteristics and device design of sub-100 nm strained Si N- and PMOSFETs," *Symp. VLSI Tech. Dig.*, pp. 98-99, 2002.

[18] S. E. Thompson and et al., "A Logic Nanotechnology Featuring Strained-Silicon," *IEEE Electron Device Lett.*, vol. 25, pp. 191-193, 2004.

[19] N. Mohta and S. E. Thompson, "Mobility Enhancement: The Next Vector to Extend Moore's Law," *IEEE Circuits & Magazine*, Sep./Oct., pp. 18-23, 2005.

[20] S. E. Thompson, G. Sun, Y. Choi, and T. Nishida, "Uniaxial-Process-Induced Strained-Si: Extending the CMOS Roadmap," *IEEE Trans. Electron Devices*, vol. 53, pp. 1010-1020, 2006.

[21] S. E. Thompson, "Strained Silicon MOSFETs: The Next Material Change to Extend Moore's Law," *Proc. MRS*, 2004.

[22] C. Kittle, *Introduction to Solid State Physics*, 6th ed. New York: John Wiley & Sons, Inc., pp. 80-87, 1996.

[23] K. Matsuda, "Stress-Induced Effects on Depletion-Layer Capacitance of Metal-Oxide-Semiconductor Capacitors," *Appl. Phys. Lett.*, vol. 83, pp. 4351-4353, 2003.

[24] S. L. Chuang, "Efficient Band-Structure Calculations of Strained Quantum Wells," *Phys. Rev. B*, vol. 43, pp. 9649-9661, 1991.

[25] G. Dresselhaus, A. F. Kip, and C. Kittel, "Cyclotron Resonance of Electrons and Holes in Silicon and Germanium Crystals," *Phys. Rev.*, vol. 98, pp. 368-384, 1955.

[26] I. Balslev and P. Lawaetz, "On the Interpretation of the Observed Hole Mass Shift with Uniaxial Stress in Silicon," *Phys. Lett.*, vol. 19, pp. 6-7, 1965.

[27] Kehuey Wu, *Ph. D. Thesis of Univ. of Florida*. 2006.

[28] J. Lim, S. E. Thompson, and J. G. Fossum, "Comparison of Threshold-Voltage Shifts for Uniaxial and Biaxial Tensile-Stressed n-MOSFETs," *IEEE. Electron Device Lett.*, vol. 25, pp. 731-733, 2004.

[29] C. G, Van de Walle and R. M. Martin, "Theoretical calculations of heterojunction discontinuities in the Si/Ge system," *Phys. Rev. B*, vol. 34, pp. 5621-5634, 1986.

[30] C. G, Van de Walle, "Band lineups and deformation potentials in the model-solid theory," *Phys. Rev. B*, vol. 39, pp. 1871-1883, 1989.

[31] A. Hamada and et al., "A new aspect of Mechanical Stress Effects in Scaled MOS Devices," *IEEE Trans. Electron Devices*, 1991.

[32] R. E. Beaty and et al., "Evaluation of Piezoresistive Coefficient Variation in Silicon Stress Sensors Using a Four-Point Bending Test Fixtures", " *IEEE Trans. Components, Hybrids and Manufacturing Technology*," 1992.

[33] S. A. Gee and et al., "The design and Calibration of a Semiconductor Strain Gauge Array," *Proc. on Microelctronic Test Structures*, vol. 1, pp. 185-191, 1988.

[34] Tung-Sheng Chen and Yu-Ren Huang, "Evaluation of MOS Devices as Mechanical Stress Sensors" *IEEE Trans. Components and Packaging Technologies* ," 2002.

[35] S. Timoshenko, *Strength of Materials*, 3rd ed. Huntington: Robert E. Krieger Publishing Co., Inc., 1976, c1958.

[36] J. J. Wortman and R. A. Evans, "Young's Modulus, Shear Modulus, and Poisson's Ratio in Silicon and Germanium," *J. Appl. Phys.*, vol. 36, pp. 153-156, 1965.

[37] T. Toriyama and S. Sugiyama, "Analysis of Piezoresistance in p-Type Silicon for Mechanical Sensors," *IEEE. J. Microelectromechanical Systems*, vol. 11, pp.598-604, 2002.

[38] G. Dorda, "Piezoresistance in Quantized Conduction Bands in Silicon Inversion Layers," *J. Appl. Phys.*, vol. 42, pp. 2053-2060, 1971.

[39] P. Kleimann, B. Semmache, M. L. Berre, and D. Barbier, "Stress-dependent Hole Effective Masses and Piezoresistive Properties of P-type Monocrystalline and polycrystalline Silicon," *Phys. Rev. B*, vol. 57, pp. 8966-8971, 1998.

[40] Y. Taur and T. H. Ning, *Fundamentals of Modern VLSI Devices*. Cambridge New York: Cambridge University Press, 1998.

[41] W. Zhang and J. G. Fossum, "On the Threshold Voltage of Strained-Si-$Si_{1-x}Ge_x$ MOSFETs," *IEEE Trans. Electron Devices*, vol. 52, pp. 263-268, 2005.

[42] J. Welser, J. L. Hoyt, S. Takagi, and J. F Gibbons, "Strain Dependence of the Performance Enhancement in Strained-Si n-MOSFETs," *Technical Digest of the IEEE International Electron Devices Meeting*, pp. 373-376, 1994.

[43] Q. Xiang and et al., "Strained silicon nMOS with nickel-silicide metal gate," *Symp. VLSI Tech. Dig.*, pp. 101-102, 2003.

[44] N. Sugii and et al., "Performance enhancement of strained-Si MOSFETs fabricated on a chemical-mechanical-polished SiGe substrate," *IEEE Trans. Electron Devices*, vol. 49, pp. 2237-2243, 2002.

[45] X. Yang, J. Lim, G. Sun, K. Wu, T. Nishida, and S. E. Thompson, "Strain-induced changes in the gate tunneling currents in p-channel metal-oxide-semiconductor field-effect transistors," *Appl. Phys. Lett.*, vol. 88, pp. 052108, 2006.

[46] W. Zhao, A. Seabaugh, V. Adams, D. Jovanovic, and B. Winstead, "Opposing Dependence of the Electron and Hole Gate Currents in SOI MOSFETs under uniaxial strain," *IEEE Electron Device Letters*, vol. 26, pp. 410-412, 2005.

[47] N. Yang, W. K. Henson, J. R. Hauser, J. J. Wortman, "Modeling Study of Ultrathin Gate Oxides Using Direct Tunneling Current and Capacitance-Voltage Measurements in MOS Devices," *IEEE Trans. Electron Devices*, vol. 46, pp. 1464-1470, 1999.

[48] Y. T. Hou, M. F. Li, Y. Jin, and W. H. Lai, "Direct tunneling hole currents through ultrathin gate oxides in metal–oxide–semiconductor devices," *J. Appl. Phys.*, vol. 91, pp. 258-264, 2002.

[49] T. Numata, T. Mizuno, T. Tezuka, J. Koga, and S. Takagi, "Control of Threshold-Voltage and Short-Channel Effects in Ultrathin Strained-SOI CMOS Devices," *IEEE Trans. Electron Devices*, vol. 52, pp. 1780-1786, 2005.

[50] H. S. Fu and C. T. Sah, "Theory and experiment on surface *1/f* noise in MOS transistors," *IEEE Trans. Electron Devices*, vol. ED-19, pp. 273, 1972.

[51] A, Van Der Ziel, "On the noise spectra of semiconductor noise and of flicker effect," *Physics*, vol. 16, pp. 359-372, 1950.

[52] F. K, Du Pre, "A suggestion regarding the spectral density of flicker noise," *Phys. Rev.*, vol. 78, pp. 615, 1950.

[53] B. Neri, P. Olivo, B. Ricco, "Low-frequency noise in silicon-gate metal-oxide-silicon capacitors before oxide breakdown," *Appl. Phys. Lett.*, vol. 51, pp. 2167-2169, 1987.

[54] K. S. Ralls, W. J. Skocpol, L. D. Jackel, R. E. Howard, L. A. Fetter, R. W. Epworth, and D. M. Tennant, "Discrete resistance switching in submicrometer silicon inversion layers: Individual interface traps and low-frequency (*1/f*) noise," *Phys. Rev. Lett.*, vol. 52, pp. 228-231, 1984.

[55] M. E. Welland and R. H. Koch, "Spatial location of electron trapping defects on silicon by scanning tunneling microscopy," *Appl. Phys. Lett.*, vol. 48, pp. 724-726, 1986.

[56] F. N. Hooge, "*1/f* noise is no surface effect," *Phys. Lett.*, vol. 29A, pp. 139-140, 1969.

[57] F. N. Hooge, "*1/f* noise sources," *IEEE Trans. Electron Devices*, vol. 41, pp. 1426-1935, 1994.

[58] R. P. Jindal, "Compact Noise Models for MOSFETs," *IEEE Trans. Electron Devices*, vol. 53, pp. 2051-2061, 2006.

[59] K. K. Hung, P. K. Ko, and Y. C. Cheng, "A unified model for the flicker noise in metal-oxide-semiconductor field-effect-transistors," *IEEE Trans. Electron Devices*, vol. 37, pp. 654-665, 1990.

[60] J. Chang, A. A. Abidi, and C. R. Viswanathan, "Flicker noise in CMOS transistors from subthreshold to strong inversion at various temperature," *IEEE Trans. Electron Devices*, vol. 41, pp. 1965-1971, 1994.

[61] L. K. J. Vandamme, X. Li, and D. Riguad, "*1/f* noise in MOS devices, mobility or number fluctuations," *IEEE Trans. Electron Devices*, vol. 41, pp. 1936-1945, 1994.

[62] M. J. Deen and O. Marinov, "Effect of forward and reverse substrate biasing on low-frequency noise in pMOSFETs," *IEEE Trans. Electron Devices*, vol. 49, pp. 409-413, 2002.

[63] A. Blaum, O. Pilloud, G. Scalea, and J. Victory, "A New Robust On-Wafer *1/f* Noise Measurement and Characterization System," Proc. *IEEE 2001 Int. Conference on Microelectronic Test Structures*, vol.14, pp. 125-130, 2001.

[64] T. A. Kramer and R. F. W. Pease, "Noise in Sub 100nm Transistors and Nanostructure," *DURINT MEETING*, 2001.

[65] R. Jayaraman and C. G. Sodni, "A *1/f* Noise Technique to Extract the Oxide Trap Density Near the Conduction Band Edge of Silicon," *IEEE Trans. Electron Devices*, vol. 36, pp. 1773-1782, 1989.

[66] H. Goldstein, *Classical Mechanics, 2nd ed*. Massachusetts: Addison-Wesley Publishing Company, Inc., 1980.

[67] T. Mizuno and et al., "(110)-Strained-SOI n-MOSFETs with Higher Electron Mobility," *IEEE. Electron Device Lett.*, vol. 24, pp. 266-268, 2003.

[68] T. Mizuno and et al., "(110)-Surface Strained-SOI CMOS Devices," *IEEE Trans. Electron Devices*, vol. 52, pp. 367-374, 2005.

[69] L. D. Laude, M. Carnoda, and F. H. Pollak, "Deformation Potentials of the Indirect and Direct Absorption Edges of AlSb," *Phys. Rev. B*, vol. 1, pp. 1436-1442, 1970.

[70] L. D. Laude, F. H. Pollak, and M. Carnoda, "Effects of Uniaxial Stress on the Indirect Exciton Spectrum Silicon," *Phys. Rev. B*, vol. 3, pp. 2623-2636, 1971.

[71] A, Rahman, M. S. Lundstrom, and A. W. Ghosh, "Generalized effective-mass approach for n-type metal-oxide-semiconductor field-effect transistors on arbitrarily oriented wafers," *J. Appl. Phys.*, vol. 97, pp. 053702, 2005.

[72] T. L. Tewksbury, H. Lee, "Characterization, Modeling, and Minimization of Transient Threshold Voltage Shifts in MOSFET's," *IEEE J. Solid-State Circuits,* vol. 29, pp. 239-252, 1994.

[73] S. Suthram, J. C. Ziegert, T. Nishida, and S. E. Thompson, "Piezoresistance Coefficients of (100) Silicon nMOSFETs Measured at Low and High (□1.5 GPa) Channel Stress, "*IEEE. Electron Device Lett.*, vol. 25, pp. 731-733, 2004.

[74] Y. G. Wang, D. B. Scott, Y. Wu, J. L. Waller, J. Hu, K. Liu, and V. Ukraintsev, "Effects of uniaxial mechanical stress on drive current of 0.13 μm MOSFETs," *IEEE Trans. Electron Devices*, vol. 50, pp. 529–531, 2003.

[75] Z. Celik and T. Y. Hsiang, "Study of *1/f* Noise in N-MOSFET's: Linear Region," *IEEE Trans. Electron Devices*, vol. ED-32, pp. 2797–2802, 1985.

[76] C. Surya and T. Y. Hsiang, "Theory and Experiment on the $1/f^{\gamma}$ noise in p-channel metal-oxide-semiconductor field-effect transistors at low bias," *Phys. Rev. B*, vol. 33, pp. 4898-4905, 1986.

[77] C. Surya and T. Y. Hsiang, "Surface mobility fluctuations in metal-oxide-semiconductor field-effect transistors," *Phys. Rev. B*, vol. 35, pp. 6343-6347, 1987.

[78] A. K. M. Ahsan and D. K. Schroder, "Impact of channel carrier displacement and barrier height lowering on the low-frequency noise characteristics of surface-channel n-MOSFETs," Solid-State Electron. vol. 49, pp. 654-662, 2005.

[79] D. Bauza, "Near interface oxide traps capture kinetics in metal-oxide-semiconductor transistors: Modeling and measurement," *J. Appl. Phys.*, vol. 84, pp. 6178-6186, 1998.

[80] O. Weber and S. Takagi, "New Findings on Coulomb Scattering Mobility in Strained-Si nFETs and its Physical Understanding," Symposium on VLSI Technology of Technical Papers. pp. 130-131, 2007.

[81] J. R. Brews, "Theory of the carrier-density fluctuation in an IGFET near threshold," *J. Appl. Phys.*, vol. 46, pp. 2181, 1975.

[82] M. V. Haartman, "Low-frequency noise characterization, evaluation and modeling of advanced Si- and SiGe-based CMOS transistors," *Ph. D. Thesis of School of KTH Information and Communication Technology*, *Stockholm*, *Sweden*. 2006.

BIOGRAPHICAL SKETCH

Ji-Song Lim was born in Korea. He received his Master of Science degree in electrical and computer engineering from the University of Florida in 2002, where he is currently pursuing a Ph.D. degree focusing his research on strain effects on silicon CMOS transistors such as threshold voltage, gate tunneling current, and *1/f* noise characteristics.